The copyright of this thesis vests in the author. No quotation from it or information derived from it is to be published without full acknowledgement of the source. The thesis is to be used for private study or non-commercial research purposes only.

Published by the University of Cape Town (UCT) in terms of the non-exclusive license granted to UCT by the author.

University of Cape Town

Changes in the Near-Surface Stress in Titanium Caused by Krypton Ion-Implantation

By

Raji Abdulrafiu Tunde

Thesis submitted to the Department of Physics,
University of Cape Town, South Africa.

In partial fulfilment of the award of

Master of Science (M.Sc) Degree in

Physics

December, 2006

CONTENT

ABSTRACT

Ion implantation has been performed on polycrystalline titanium samples with 170 keV Kr^+ ions at two different doses of 1 x $10^{16}/cm^2$ and 5 x $10^{16}/cm^2$ at room temperature. The major techniques used in characterising the samples were Rutherford backscattering spectroscopy and X-ray diffraction. By means of the $\sin^2\Psi$ technique, the near surface stress has been determined for both unimplanted and implanted samples. The initial stress state has been shown to be strongly tensile in the first 55 nm below the surface, and weakly compressive deeper into the material. Near the surface, the main effect of the low dose implantation process was to relax the high tensile stress state. This could be attributed to stress relaxation effect of vacancies that are produced. However, higher dose implantation introduces additional sources of tensile stress. Deeper into the material, higher dose implantation introduces also, additional sources of compressive stress and these are thought to be larger defect clusters due to vacancy agglomeration.

CHAPTER 1

INTRODUCTION

The study of noble gases in materials dates as far back as 1897 when a study was reported on the permeation of helium through metals [1]. However, the motivation for the study of noble gases in materials has shifted over the years. For example in nuclear industry, interest was in the behaviour of fission and fusion products such as the swelling caused by the formation of noble gases, krypton and xenon, in nuclear reactor fuels [2]. More recently, the use of noble gas ions to modify the refractive index of optical materials through the introduction of radiation damage has been used in the fabrication of optical waveguides, such as helium-ion implanted waveguides in Zircon [3] and crystals of yttrium aluminium garnet (Nd: YAG)[4].

Noble gases are chemically uncreactive with most host matrices, but their incorporation produces physical changes in host materials. For example, individual atoms can collect into clusters and these can cause swelling of the matrix [5, 6]. Other possible effects may include changes in mechanical properties such as hardness [7] and wear resistance [8] as well as electrical properties [9]. This should be expected since the implanted ions reside in the host structure [10, 11].

Since the equilibrium solubility of noble gases in most materials is low [12, 13], the ions must be forced into the material using non-equilibrium methods. The most common method for introducing noble gases into materials is through the use of ion implantation techniques. Ion implantation is a low temperature, non-equilibrium processes by which almost any element can be introduced into the near surface region of a material. As stated earlier, the process may cause both structural and compositional changes in the host lattice and may be used to tailor materials to have particular mechanical, electrical and optical properties [14]. Ions are typically accelerated to energies of the order of 100 keV and are directed toward a sample, causing the ions to penetrate fractions of a micron into the specimen [15]. Two processes can be identified: firstly, the incoming ions collide with the substrate resulting in multiple displacements of the lattice atoms; and secondly

the penetration of implanted ions deeper into the near-surface region of the material. During an ion implantation treatment of metals, the injected ions only penetrate down to a depth of some 100 nm, termed the implanted zone (IZ). It is commonly thought that this process can cause a compressive stress near the surface [16]. This is desirable since it improves the fatigue properties by closing microcracks. However, experimental evidence on the change of stress is conflicting, even with the same materials [17]. Sharkeev et al [18] indicate that a tensile stress can be developed near the surface through ion implantation.

The nature of noble gas inclusions and their effect on the host material are often determined through the use of transmission electron microscopy (TEM) [19], X-ray diffraction (XRD) [20], positron annihilation [21], Rutherford backscattering spectrometry (RBS) [22] and ion-channelling measurements [23]. In this study however, we are mainly concerned with the effect of krypton ion implantation on the residual stress state of polycrystalline titanium. This will be studied by X-ray diffraction. Residual stress is present and plays an important role in all technological materials; metals, polymers or ceramics. The X-ray diffraction technique has been extensively used in determining the residual stress of polycrystalline samples with high precision and accuracy [24, 25]. In this work, the effect of krypton implantation on the morphology of titanium samples is investigated through scanning electron microscopy (SEM). Rutherford backscattering spectrometry (RBS) was also used to determine the dose and depth of implanted krypton. The krypton profile in titanium, and the associated damage profile, was modelled with TRIM [26] calculations. In addition, metallurgical techniques were also used to examine the microstructure details of the as-received, unimplanted titanium sample.

CHAPTER 2

DEFECTS AND STRESS IN SOLIDS

2.1 DEFECTS IN CRYSTALS

Defects are anything that break periodicity of the crystal. They can be classified according to their dimensionality as point defects, line defects, planar defects and volume defects. Point defects include vacancies and interstitial atoms. Volume defects include precipitates, voids and bubbles. Line defects are dislocations. These types of defects can be found in single crystals. However, single crystals are rarely found in real materials unless the growth condition is specially designed and controlled. Instead, most solids contain a small number of crystallites or grains, whose sizes range from nanometres to millimetres, and are thus called polycrystals. Defects in such materials include the above mentioned defects together with grain boundaries and even twin boundaries, if twinning is present.

2.1.1 POINT DEFECTS

Point defects can be categorised into four principal types: vacant lattice sites, which are vacancies; interstitial atoms; and foreign atoms which may occupy interstitial or substitutional sites. Vacancies are simply unoccupied lattice sites. The atoms around the vacant sites may relax their configuration and in most cases the point symmetry of the lattice is retained [27]. This is shown as defect 1 in figure 2.1. Defects 2 and 3 in the figure show interstitial atoms which are extra atoms that have being forced into the interstices of the crystal structure. In contrast to vacancies, a great variety of structures may occur and the point symmetry of the interstitial site is often not retained [27], although the relaxation of the site is generally outwards as shown in the figure. If the atoms in question are of the same chemical species as those of the host lattice, they are termed self-interstitials. Foreign atoms are atoms of a different chemical species from the host crystal lattice. They may be substitutional (defect 5 in figure 2.1) when they replace a host atom or interstitial (defect 3 in figure 2.1) when they occupy the otherwise empty interstices of the host lattice.

All point defects introduce local distortions to the structure (see figure 2.1) and due to these distortions, they can interact with each other and with external stresses. Defects in the form of vacancies and foreign interstitial atoms are also created in ion implanted material and are thought to cause a volume increase and contribute to generation of compressive residual stress [22].

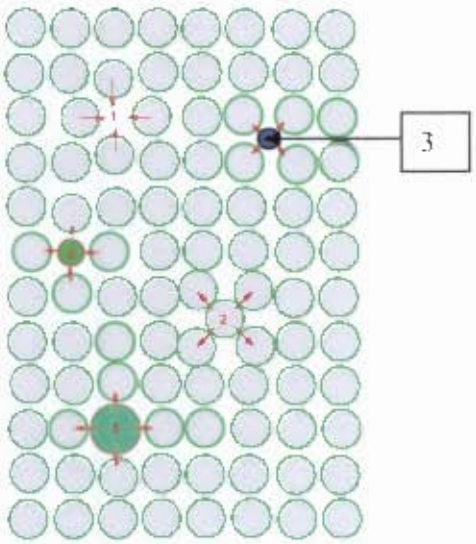

Fig 2.1 Schematic of different point defects in metals: (1) vacancy; (2) self-interstitial; (3) Interstitial impurity; (4) and (5) are substitutional impurities. The arrows represent the direction of the force exerted on the crystal structure (modified after [28]).

2.2 LINE DEFECTS: DISLOCATIONS

Dislocations are line imperfections, and like point defects they cause distortion of the crystal structure. In a simple cubic crystal for example, this distortion may be caused by a slip of one atomic distance over the left half of the slip plane, but not over the right half as shown in figure 2.2. The boundary between the slipped and unslipped region is called the dislocation. Its position is marked by the termination of an extra vertical half-plane of atoms crowded into the upper half of the crystal as shown in figure 2.3. This arrangement of atoms characterised an edge dislocation and is also shown in figure 2.2 as *EF*. The dislocation line runs along the edge of the half plane of atoms [29] and is perpendicular to the slip direction [30]. The distortion at the end of the extra half plane is caused by the

attempt of the atoms to accommodate themselves to the end of the plane. Atomic spacings in the upper half-crystal are thus compressed by the insertion; those in the lower half are extended (figure 2.3).

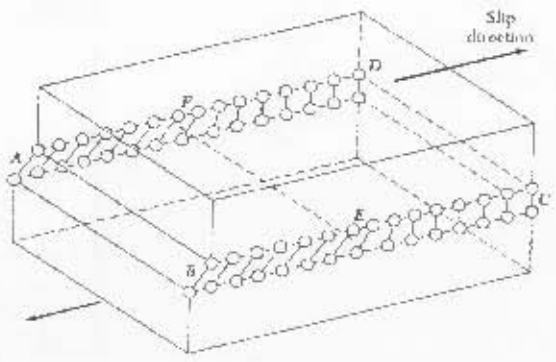

Fig. 2.2 A schematic of edge dislocation EF in the glide plane ABCD. The figure shows the slipped region ABEF in which the atoms have being displaced relative to the unslipped region FECD [29].

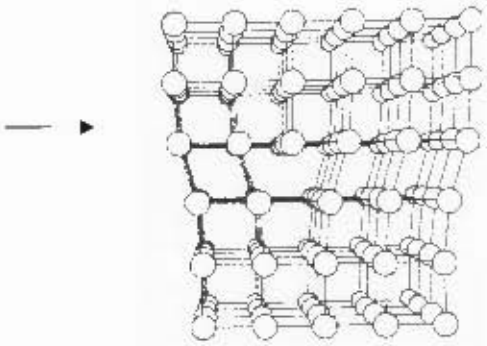

Fig. 2.3 *The structure of an edge dislocation. The deformation may be thought of as caused by inserting an extra plane of atoms in the upper half of the figure. Atomic spacings in the upper half crystal are compressed by the insertion while those in the lower half are extended. The arrow indicates the slip direction. (modified after [30])*

Another type of dislocation is the screw dislocation. A screw dislocation marks the boundary between slipped and unslipped parts of the crystal. Figure 2.4 is an example of

screw dislocation. Here, part *ABEF* of the slipped plane has slipped in the direction parallel to the dislocation line, denoted as *EF*. Unlike the edge dislocation, complete slipped planes of atoms normal to the dislocation line no longer exist, rather, all atoms lie on a single surface which spirals from one end of the crystal to the other, hence the word screw [22]. "The screw dislocation may be thought of as produced by cutting the crystal partway through with a knife and shearing it parallel to the edge of the cut by one atom spacing" [29].

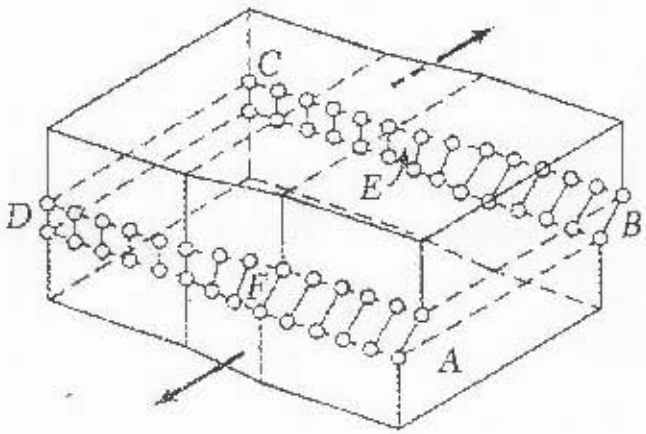

Fig. 2.4 A screw dislocation. A part ABEF of the slipped plane has slipped in the Direction parallel to the dislocation line EF [29].

An important feature of all dislocations is that the distortion is severe in the immediate vicinity of the dislocation line. Along this line, the atoms may not even possess the correct number of neighbours while not more than a few atom distances away from the centre, the distortion may be so negligible that the crystal is locally nearly perfect. The region near the dislocation line, where the distortion is extremely large, is called the core of the dislocation. Here, the local strain is very high. Far away from the core, the strain is small enough to be described by elastic theory, and is therefore called the elastic region.

2.3 DISLOCATIONS: GENERAL DESCRIPTION

Burgers has shown that the geometry of dislocations can be described in a more general manner which shows how the edge and screw dislocations are related to one another. By

constructing a closed curve within a crystal or an open curve terminating at both ends (see figure 2.5), a cut is made along any sample surface bounded by the line; the material on one side of the surface is displaced from the other rigidly by the distance $\boldsymbol{b}$, where $\boldsymbol{b}$ is the Burgers vector i.e. the vector giving the magnitude and direction of the displacement.

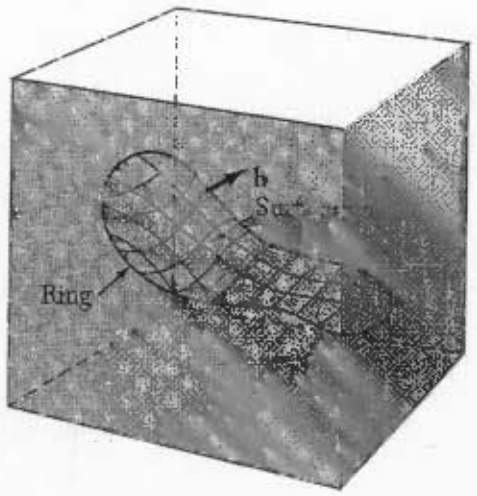

Fig. 2.5 General construction of a dislocation line. The rectangular block represents the medium. The closed curve in the interior of the block represents the ring. The contoured area provides the surface on which a dislocation can be created through cutting, displacement, filling or cutting and welding operations. $\boldsymbol{b}$ is the Burgers vector [29].

The displacement may leave a cavity in the crystal or the material may overlap, depending upon the direction of displacement. In these cases, we imagine that we either add a material to fill the gap, or subtract material to prevent overlap. The atoms are then reconnected together with their new neighbours across the surface and the crystal is then allowed to relax into that configuration which minimizes its total energy. The resulting strain pattern is that of the dislocation characterised by the boundary curve and the Burgers vector. For the screw dislocation, the shear displacement and hence the Burgers vector, lies along the dislocation line. For the edge dislocation, the Burgers vector is perpendicular to the line. Generally, the Burgers vector may have other directions with respect to the dislocation, and for these cases the dislocation is a mixture of edge and screw types. The mixed dislocation is defined in terms of the direction of the Burgers

vector. The geometry of these types can be somewhat complicated, however, it suffices to say that they are simply the geometrical composite of both types [31].

2.4 RESIDUAL STRESS

Residual stress is in general present in all technological materials with or without the presence of external applied forces; whether they are metals, polymers or ceramics [32]. They are those stresses which remain in a component following manufacture, processing, fabrication or assembly and are not necessary to maintain equilibrium between the body and its environment. In natural or artificial multiphase materials, residual stress can arise from differences in thermal expansivity, yield stress or stiffness. They can be beneficial or detrimental to performance; they may be critical or insignificant. For example, unexpected failure of components has been attributed to combined effects of service stresses and residual stress. On the other hand, residual stress are sometimes introduced deliberately [32] in a material, for example, in shot peening where compressive stresses are introduced on the surface. This compressive stress closes microcracks thereby improving the fatigue resistance of the material. Within a proper framework therefore, residual stress can be incorporated into design in material based industry, such as aerospace, nuclear and other critical engineering industries.

2.4.1 CLASSIFICATION OF RESIDUAL STRESS

Residual stress in a body may be categorised by cause; such as thermal or elastic mismatch; by the scale over which they self-equilibrate; or according to the method by which they are measured [32]. Residual stress by thermal mismatch occurs, for example, during the process of improving the failure strength of glass by rapid cooling of the surface to create a compressive stress in the exterior and thermal stress in the interior [33]. Residual stress can also be introduced during welding. In this case, large thermal stress gradients are created in the vicinity of the welded joint by the localised heating and subsequent cooling of the weld zone.

Residual stress by elastic mismatch occurs in shot peening, for example. Shot peening involves bombarding a material with a small spherical media called shot (see figure 2.6a).

As the shot peening is being performed, the atoms of the surface of the metal become crowded and try to restore the metal's original shape by pushing outward. This pulls atoms in the deeper layers towards the surface, which resist the outward pull, thereby creating an internal tensile stress that keeps the part in equilibrium with the compressive stress on the surface. The plastic bending of a bar is also a way of introducing residual stress, which varies over a whole thickness of the bar (figure 2.6b).

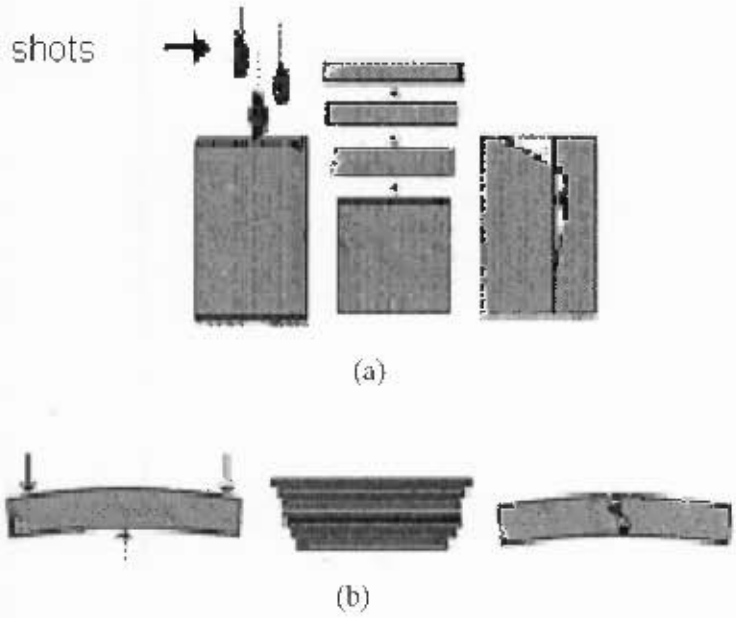

Fig 2.6 (a) schematic showing residual stress by shot peening; (b) is the residual stress by plastic deformation. The arrows in (b) shows the direction of applied force needed to bend the bar (modified after [31]).

As mentioned earlier, residual stresses may also be categorized according to their characteristic length, which is a length scale over which the stresses equilibrate. They can be classified as macroresidual, intergranular and atomic scale stresses. Figure 2.7 is a schematic of this classification, using a two phase material consisting of matrix (M) and reinforcement (R).

Macroresidual stresses are long range stresses as they equilibrate over the length scale of the structure. This length scale is represented by a continuous curve, σ_{macro} in figure 2.7. Such stresses are usually estimated, using a continuum model which ignores the

polycrystalline or multiphase nature of the material. Intergranular stresses equilibrate over a number of grain dimensions, approximately, three to ten times the grain size. As shown in figure 2.7, these are denoted by σ_{IIM} and σ_{IIR}, the intergranular stress across the matrix and the reinforcement respectively. Intergranular stresses occur, for example, as the interphase thermal stresses in a metal matrix composite. Atomic scale stresses (σ_{IIIM}) on the other hand, exist over atomic dimensions and balance within the grain size, such as, those caused by point defects and dislocations.

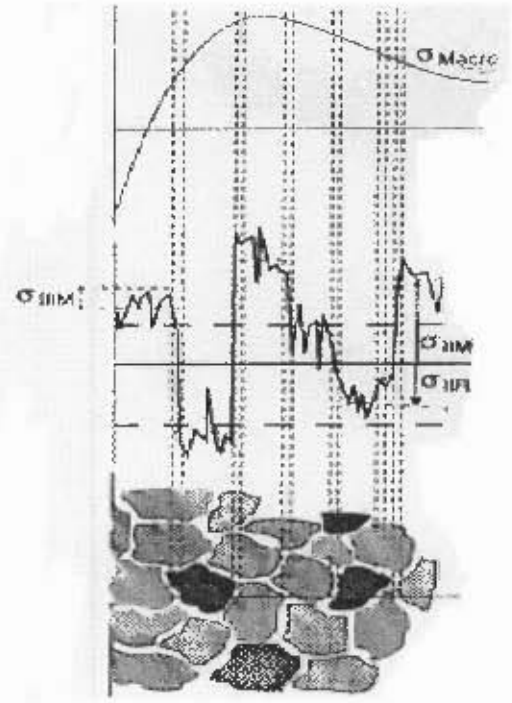

Fig 2.7 Schematic of stress classification according to length scales in a two phase material consisting of matrix (M) and reinforcement(R). σ_{macro} is the macroresidual stress; σ_{IIM} and σ_{IIR} are the intergranular stress across the matrix and the reinforcement respectively; σ_{IIIM} is the atomic scale stress (modified after [32]).

CHAPTER 3

ION INTERACTIONS IN SOLIDS

Ion implantation is a process in which energetic ions are introduced into the sub-surface of a solid substrate via bombardment [34]. The implantation energies generally range from 20-200 keV, thereby making the ions penetrate the surface of the material and come to rest below the surface. The implanted ion concentration distribution in depth is usually almost Gaussian, with the peak of the distribution at a depth of a few hundred to a few thousand angstroms, depending on the ion-target combination and the incident energy.

Ion implantation is basically a non equilibrium process. Ions can be injected into a solid without regard for normal thermodynamic constraints such as solubility limits. Thus, a saturated solid solution can be further doped with the saturated impurity to produce a supersaturated solution [35]. Another example would be implanting a species with another species when the two species are immiscible in the melt. Thus it may be possible to create metastable alloys with new and unusual properties.
Ion implantation has been applied to the creation of thin doped layers in semiconductors [36-41], and has been used to improve the material property such as wear resistance of hard coatings, and to increase the lifetime of cutting tools [42].

3.1 RANGE OF IMPURITY IONS

When a beam of energetic ions impinges on a surface of a solid, the fast ions interact with the stationary near-surface atoms leading to three possible effects. These include ion penetration into the subsurface region, re-arrangement of near-surface atoms and the emission of particles or other forms of radiation from the surface [43] (Figure 3.1).

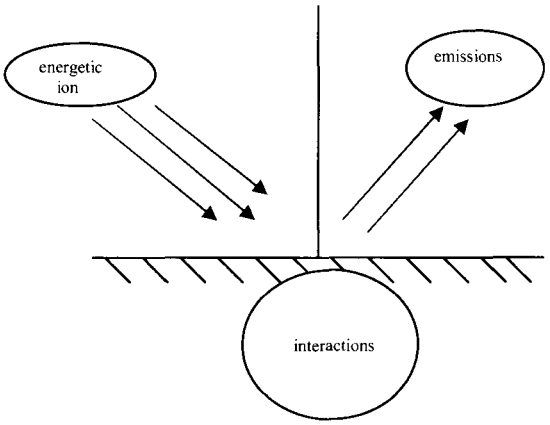

Fig 3.1 Schematic showing various form of ion interaction with a solid.

Ions penetrating a solid undergo two types of collision with the host atoms: with the nucleus and with electrons of the target atoms. These are often referred to as nuclear and electronic collisions respectively. Each of these collision processes leads to loss of energy, leading to the stopping of the ions at a certain distance from the surface. This distance is the penetration depth of the ions in the solid, and is usually called the range, R. The range is thus dependent on the rate of energy loss as the ions transverse the solid. This is mathematically expressed as [43]

$$R = \int_{E_0}^{0} \frac{1}{(dE\ dx)} dE \quad , \tag{3.1}$$

where the stopping power dE/dx represents the energy loss per increment of path. If the orientation of the crystal lattice is neglected, the main parameters governing the range or energy loss rate are the incident energy E_0, the atomic number, and mass of the ion and the target. The heavy ions penetrate much shallower than light ions. The energy loss rate, dE/dx, can thus be expressed as a sum of energy loss rates due to nuclear and electronic collisions. Hence

$$\frac{dE}{dx} = \left(\frac{dE}{dx}\right)_n + \left(\frac{dE}{dx}\right)_e \quad . \tag{3.2}$$

Substituting equation 3.2 into 3.1, the range R can thus be expressed as:

$$R = \int_{E_0}^{0} \frac{dE}{(dE\ dx)_n + (dE\ dx)_e} \quad . \tag{3.3}$$

Due to the statistical nature of the energy loss processes, the range of penetration of incident ions in the solid differs. This is often referred to as the range distribution. Figure 3.2 is a schematic describing the ion range parameters. Usually, the projection of R normal to the surface (penetration depth) is of interest rather than the total distance. This is known as the projected range R_P.

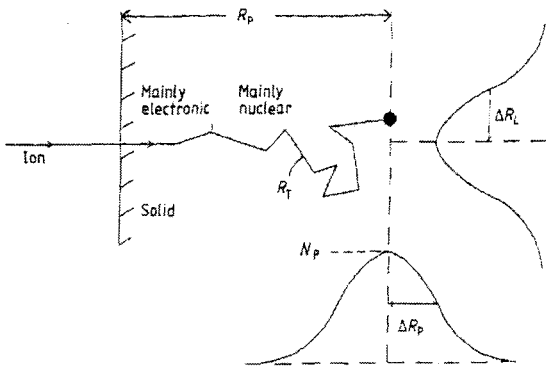

Fig 3.2: Schematic of ion range parameters. R_P is the projected range [43]

From the knowledge of the range distributions, it is possible to estimate the peak concentration, N_p, for a given implanted dose N_s using the expression [35]

$$N_p \approx \frac{N_s}{2.4\Delta R_p} \quad . \tag{3.4}$$

The number of ions per centimetre square (ions/cm^2) implanted into the solid is called the ion dose or the fluence. The dose rate is the number of implanted ions per second. The concentration C at depth x is [14]

$$C(x) = \frac{\phi}{n\Delta R_p \sqrt{2\pi}} \exp[-(x - R_p)^2 / 2\pi(\Delta R_p)^2] \quad , \qquad (3.5)$$

where ϕ and n represent the ion fluence and the atomic density respectively. ΔR_p is the projected range straggling. The projected range of ions in the substrate is related to the range straggling as [14]

$$R_P \cong 2.5\Delta R_P \quad . \qquad (3.6)$$

3.2 SCATTERING PROCESSES

During ion implantation, bombarding energetic particles interact with many target nuclei resulting in a large number of interactions. The amount of energy transferred to the target nuclei, or the scattering angle is usually addressed using the concept of differential cross-section. This gives a measure of "either the probability of transferring energy T in the range between T *and* dT to a target atom or the probability of scattering a projectile into some angle θ_c *and* $\theta_c + d\theta_c$" [44]. The term cross-section refers to the differential cross-section integrated over all angles and is simply the effective target area presented by each scattering centre (target nucleus) to the incident ions.

Figure 3.3 is a schematic of the collision process in which the incident particle is scattered by the target nucleus through an angle, θ_c. The projectile motion was a straight line until it is fairly close to the target nucleus, at which point it is deflected through an angle θ_c. The scattering cross-section is thus dependent on the impact parameter b.

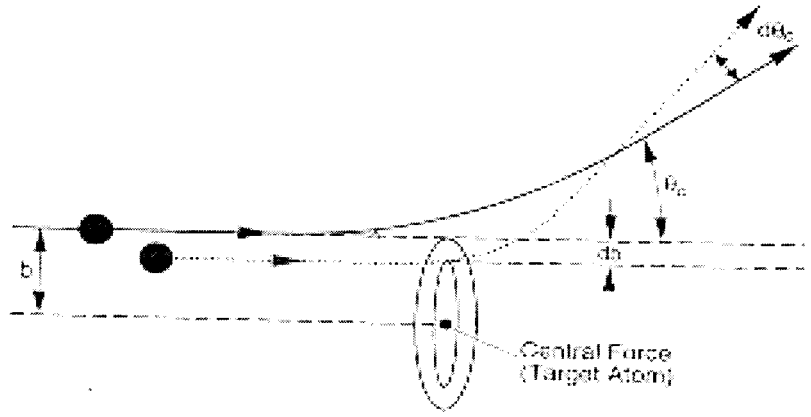

Fig 3.3 Target area for the differential cross-section $d\sigma$ *and impact parameter b [44].*

In a simple model, all incident particles with impact parameter b are headed in a direction to strike the rim of the circle drawn around the target nucleus, and will be deflected by angle θ_c. The area of this circle is πb^2 and any particle with a trajectory that strikes anywhere within this area will be deflected by an angle greater than θ_c. The target area defined by the impact parameter is called the total cross-section,

$$\sigma = \pi b^2 \quad . \tag{3.7}$$

In addition to the total cross-section, there is a differential cross-section and it has relationship to b. This is found by taking the differential of Eqn. (3.7) with respect to the impact parameter:

$$d\sigma = 2\pi b db \quad . \tag{3.8}$$

Figure 3.4 shows a thin plate with each target presenting an effective scattering area σ. A flux of energetic incident particles traverses a thin target of thickness dx and unit area, containing a total of N target atoms per unit volume.

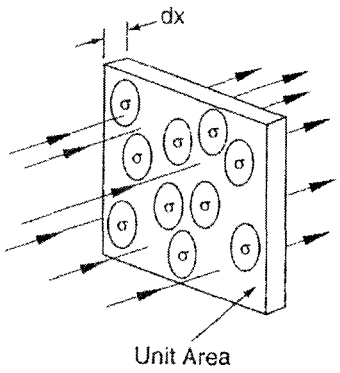

Fig 3.4 Schematic view showing a thin plate with each target atom presenting an effective scattering area σ. dx is the elemental width of the foil [44].

Each target atoms present an effective scattering area σ to the incoming projectile. The probability of a projectile with energy E undergoing scattering event or a collision with a target nucleus while traversing a thickness dx is

$$P(E) = N\sigma(E)dx \quad , \tag{3.9}$$

where $\sigma(E)$ is the total collision cross section between an energetic particle of energy E and target atoms. The total cross section gives a measure of the probability for any type of collision to occur where energy transfers are possible for energy up to and including the maximum value. The differential energy transfer cross-section $d\sigma(E)/dT$ is the probability that a projectile with energy E will transfer an amount of energy between T *and* $T + dT$ to a target atom and is obtained by differentiating equation 3.9,

$$P(E,T)dT = \frac{1}{\sigma(E)}\frac{d\sigma(E)}{dT}dT \quad . \tag{3.10}$$

P(E, T) is the probability that an ion with energy E will undergo a collision producing an energy transfer in the range T *to* $T+dT$ while transversing the distance dx .

The differential cross-section is an important parameter in describing ion ranges in solids and radiation damage. For example, the nuclear stopping power in Eqn.3.2 can be expressed as

$$\left(\frac{dE}{dx}\right)_n = N\varepsilon(E) = N\int_{T_{min}}^{T_m} T\,\frac{d\sigma(E)}{dT}dT \quad . \tag{3.11}$$

where N is the number of target atoms per unit volume, and ε is the stopping cross section. T_{min} is the minimum energy transferred, and is usually the energy required to displace an atom from its site. The upper limit is the maximum energy transferred and is given by

$$T_m = \frac{4M_1M_2E}{(M_1+M_2)^2} \quad , \tag{3.12}$$

where M_1 and M_2 and E are the atomic masses of the projectile and target atom and incident energy respectively. With regard to radiation damage, the total number of

displacement damage or Frenkel pairs (vacancy-interstitial defect) resulting from an ion of initial energy E_0 is given as

$$N_p(E_0) = \int_0^{E_0} \sigma_d(E') \frac{dE}{\varepsilon(E')} \quad , \tag{3.13}$$

where $\sigma_d(E')$ is the displacement cross-section at energy $E' = E'(x)$, defined as the ion energy as a function of the travelled path length x towards the end of the range, down to zero energy. $\varepsilon(E')$ is the stopping cross section.

3.3 CHANNELING EFFECT

The structure of the target crystal has a large effect on the stopping and therefore on the range profiles of implanted ions [45]. In single crystalline structures, atoms occupy a periodic lattice, forming rows of atoms and empty spaces. Depending on the viewing direction, the same structure can appear to be closed or open. Incident energetic ions can move longer distances, without collisions, between the channel formed by rows of atoms since they do not make close-impact collisions with the lattice atoms, and thus have a much lower rate of energy loss, $\frac{dE}{dx}$, than non-channeled ions. Less energy loss means greater range in solids compare to non-channeled ions (Fig. 3.5). This crystal orientation effect on implanted ion range distribution is called channeling or the channeling effect.

A theoretical explanation for this phenomenon is that the ions are channeled if they are incident within some critical angle to the channel direction [14]. This critical angle is a function of the incident ion energy, ion species, and the target material. The channeling distribution also depends on surface preparation, temperature, beam alignment and disorder introduced during the implantation process itself.

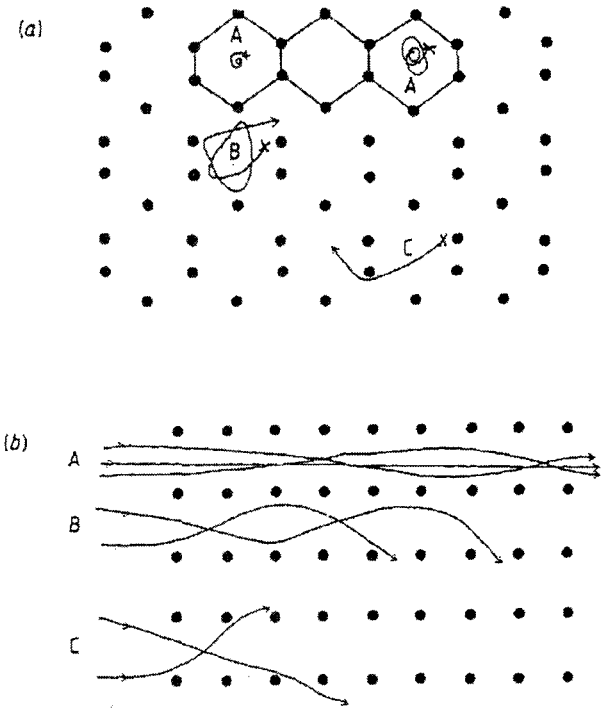

Fig 3.5: Schematic illustrating channeling effect (a) end view, and (b) side view for well channelled (A), dechanneled (B), and random (C) trajectories [43].

In Figure 3.5, ions following the trajectory labelled *A* are well channeled and thus penetrate deeper into the crystal. Energy loss is predominantly electronic. The ions in trajectory B are dechanneled "since they are incident too close to the atomic rows, or with an angle which is not particularly well aligned with the axis. The ions thus oscillate, resulting in unstable trajectories in the channel and so do not penetrate as deeply as well-channeled ions. Ions following trajectory *C* are not steered by the lattice rows. Their motion is random and they penetrate the solid the least.

3.4 DAMAGE PRODUCTION

The collision between the implanted ions and the host lattice atoms may result in the displacement of host atoms from their lattice positions. Lattice atoms which are displaced by incident ions are called primary knock-on atoms or PKAs. The PKAs, if having sufficient energy, can in turn displace other atoms thus creating a cascade of atomic collisions. This atomic process leads to the creation of lattice damage such as vacancies,

interstitial atoms and their clusters. If the atomic displacements are large, a dense defect microstructure can result [14].

The primary damage state in irradiated materials depends on the bombarding particle and its energy, ranging from isolated Frenkel pairs under electron irradiation, through cascades with average energies of a few keV with heavy ion bombardment, up to cascades with energies well in excess of 100 keV for high energy neutron bombardment [47]. Furthermore, the distribution of damage in a material also depends on the type and energy of the bombarding particle. Heavy ions with energies of a few MeV have ranges of few micrometers. Defect production is thus confined to thin surface layers and is non-uniform within these layers, peaking near the end of the range of the bombarding particle. In contrast, light ions and electrons have ranges of a millimetre or more and are thus capable of introducing defects which are deeper in the bulk of a material.

3.5 DEFECT MIGRATION

The initial damage event results in vacancies and interstitials isolated from each other or in small clusters. These defects cannot mutually annihilate without subsequent diffusion. The possible fates of the defects during these diffusion processes lead to macroscopic changes in the physical and mechanical properties of the material such as stress state, swelling, hardening and creep [47].

The movements of defects in solids are temperature dependent. For example, both vacancies and interstitials are immobile at low temperature, thus leading to the formation of dense clusters of defects as a result of the nuclear displacements within each ion cascade. The interstitials become mobile at higher temperatures and will migrate to be annihilated at vacancies and other sinks, or to cluster, thus leaving a distribution of vacancies and defect clusters. The vacancies also become mobile at still higher temperature. The vacancies can then agglomerate, forming defect clusters and dislocation loops [14].

Complex defects, voids and extended defects such as dislocations are also formed at high temperature and at high implantation fluence. Void formation is enhanced by the

presence of insoluble gases such as helium in the matrix. Point defects can also migrate under the influence of applied stress fields which provide the driving force. By treating the defect as a Somigliana dislocation, the force on a general inhomogeneity in an elastic medium is [48]

$$F = \oiint_{\xi} (u \cdot \nabla \sigma - \sigma \cdot \nabla u) \cdot ds \quad , \tag{3.14}$$

where σ is the applied stress and the displacement field of the defect in the surrounding medium is u. ξ is the surface of integration and it encloses the surface singularity corresponding to the defect, in this case a sphere.

In addition, both point and extended volume defects can be regarded as elastic inclusions with a volume V different from the volume of the surrounding medium, V_0 which they replace [49, 50]. There is thus a volume mismatch, often expressed as:

$$V = V_0(1 + \alpha) \quad , \tag{3.15}$$

where α denotes the mismatch parameter. A positive α represents a centre of dilatation in the case of interstitial atom. In the case of a vacancy however, α is negative and it represents the centre of contraction. The force on such an inclusion according to Eshelby [49] is

$$F = \alpha \frac{4}{3} \pi r_0^3 \nabla Tr(\sigma) \quad , \tag{3.16}$$

where r_0 is the radius of the defect core and $Tr(\sigma)$ is the normal stress which can be written as

$$Tr(\sigma) = \sigma_{11} + \sigma_{22} + \sigma_{33} \quad . \tag{3.17}$$

It is thus evident from equation 3.16 that force on a spherical defect is due to the presence of a stress gradient. Thus, the force acting on a centre of dilatation such as foreign interstitial atom is opposite to that acting on a centre of contraction (i.e. vacancy) [48]. It

can further be said that that the force on an interstitial is 'uphill' *i.e.* in the direction of increasing tensile stress and that on a vacancy is 'downhill', in the direction of compressive stress.

The rate of change of concentration of particles (vacancies and interstitials) at any position r in the distribution can be derived from the total flux using Fick's law:

$$\frac{\partial c}{\partial t} = -\nabla J + S(r,t) \quad . \tag{3.18}$$

The second term S*(r, t)* represents the rate at which particles are created at any point. ∇J is the gradient of the particle flux and it results from two contributions: diffusive J_D ,and forced J_F . It can thus be expressed as [48]

$$J = -D\nabla c + \eta cF \quad , \tag{3.19}$$

where the two terms represent J_D and J_F respectively. c is the particle concentration, D is the diffusivity and η is the mobility. For a random diffusion process such as gas diffusion, the diffusivity can be interpreted as the product of the mean free path and the molecular velocity. With respect to thermally activated processes such as vacancy diffusion, it can be interpreted as the product of mean squared displacement and the jump rate. The mobility η is a measure of how fast a particle can be moved under the influence of an applied force. Its product with the force gives the drift velocity as can be found in hydrodynamics and current electricity.

The mobility is related to diffusivity through the Nernst-Einstein relationship

$$\eta = \frac{D}{kT} \quad , \tag{3.20}$$

where k is Boltzmann's constant and T the absolute temperature. Equations 3.18 and 3.19 can be combined to give the general form of the drift diffusion equation

$$\frac{\partial c}{\partial t} = D[\nabla^2 c - \frac{1}{kT}(F \cdot \nabla c + c\nabla \cdot F] + S(r,t) \ , \qquad (3.21)$$

which has found useful application in studying ion implantation damage [48].

Also, by considering the strain fields which are intrinsic to the individual defects, the influence of point defects on each other can be investigated. However, the strain fields due to spherically symmetric defects in an infinite isotropic medium are a pure shear which causes no dilation of the surrounding medium. It can thus be concluded that spherically, point-like defects cannot influence the dynamic of other point defects [48]. For stress induced diffusion to occur, another source of stress must be present besides the point defects. Consequently, the clustering of point defects is thermodynamically driven. Non-spherically symmetric displacement fields of the large defects may however lead to accelerated or retarded clustering, as can an existing residual stress field.

CHAPTER 4

EXPERIMENTAL TECHNIQUES

4.1 ION BEAM ANALYSIS (IBA)

The acronym IBA is mostly used for a variety of techniques based on the detection of ions scattered by target nuclei. The energy of the scattered projectile is measured and related to the mass of the scattering nucleus and its position in the matrix. Rutherford backscattering Spectrometry (RBS) is an important IBA technique in which the collision energy must be below the Coulomb barrier, and the projectile must be lighter than the target. This makes RBS particularly useful for determination of the depth distribution of heavier elements in light element matrices [51].

In Rutherford backscattering spectrometry, a beam of collimated and monoenergetic particles of energy E_0 is generated from the source (see figure 4.1). These particles impinge on the sample (or target) which is the object to be analyzed. Most of the incident particles come to rest within the sample, while a few (of order 10^{-4}) are scattered back out of the sample. Of these, a small portion is incident on the area defined by the aperture of the analyzing system. The output of the system is a signal which is processed by the multichannel analyzer which subdivides its magnitude into series of equal increments. Each increment is numbered and is referred to as a channel. An event whose magnitude falls within a particular channel is registered there as a count.

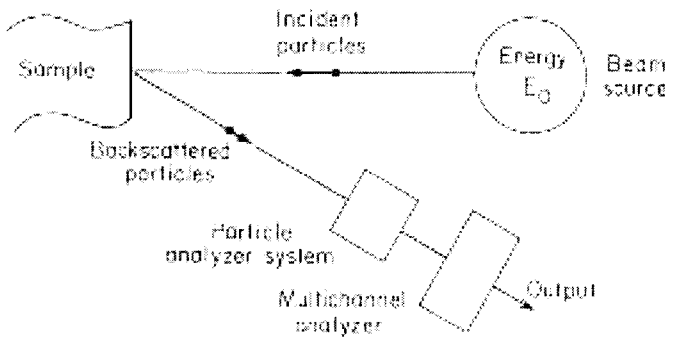

Fig 4.1 Schematics of beam path in a Rutherford backscattering system [52].

At the termination of the experiment, each channel has registered a certain number of counts. The output of the multichannel analyzer is thus a series of counts contained in the various channels. A series of counts versus channel number constitutes a back-scattering spectrum. The ordinate is frequently labelled as the yield, or the backscattering yield. The relation between the energy of the backscattered and detected particle and the channel number in which the particle is counted is a characteristic of the system and must be determined experimentally. This is often referred to as the system calibration. An example is shown in figure 4.2.

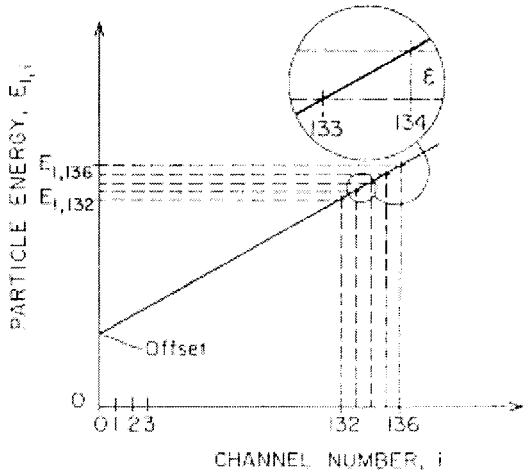

Fig 4.2 Relationship between detected particle energy and channel number [52].

The abscissa is the channel number *i*. The ordinate gives the energy $E_{1,i}$ of a detected particle where $E_{1,i}$ are the energies of particles that produce counts in channel *i*. The slope of the line corresponds to the energy interval corresponding to one channel. It is thus possible to convert the abscissa of a backscattering spectrum from channel numbers to particle energy.

4.1.1 ENERGY LOSS INFORMATION

Back-scattering provides a mass-sensitive depth spectroscopy [53]. This means that, it provides the ability to distinguish the atomic mass of elements and their distribution in depth as a function of detected energy.

Figure 4.3 illustrates the kinematics of the elastic collision process in Rutherford backscattering. For a helium ion of incident energy E_0 and of mass M_1, colliding with the target atom of mass M_2, the scattered energy E_1 is given by [52]

$$E_1 = K_M E_0 \quad , \tag{4.1}$$

where K_M is the kinematic factor, given as [52]

$$K_M = \frac{E_1}{E_0} = \frac{\left(M_2^2 - M_1^2 \sin^2\theta\right)^{\frac{1}{2}} + M_1 \cos\theta}{M_1 + M_2} \tag{4.2}$$

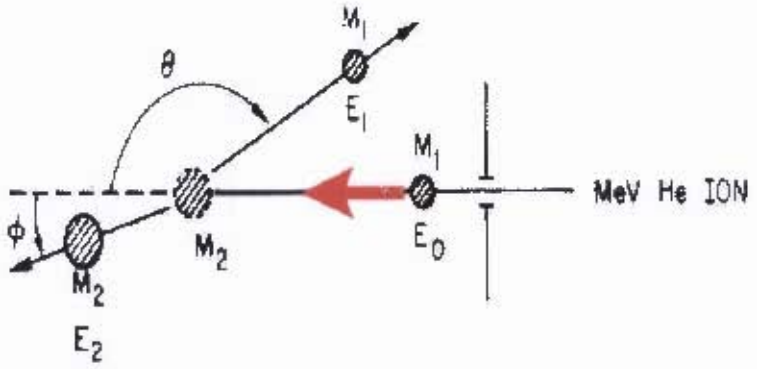

Figure 4.3 Schematic of kinetics of elastic collision [52].

With increasing atomic mass of the target atoms, K_M increases (approaching unity) and hence the energy of the elastically scattered particle increases approaching E_0. This allows one to distinguish elements. Because of the energy loss of the He ions in the target material, the signals from larger depths will have lower energy. The left edge of a typical RBS spectrum thus represents scattering from deepest part of the material. If the energy difference ΔE represents the energy loss by the beam particles on inward and outward passage through a surface, the relationship [53]

$$\Delta E = [S]\, t \tag{4.3}$$

gives the direct relation between the total thickness of the layer and the total width ΔE of the signal. *[S]* is the energy loss parameter which depends on K_M and the energy loss per unit length dE/dx in the material and t is the film thickness. Equation 4.3 holds for thicknesses less than 500 nm [53]. Information on energy loss dE/dx is generally presented in the form $dE/\rho dx$ or stopping cross section ε, where

$$\varepsilon = \frac{1}{N}\frac{dE}{dx} = \frac{M}{N_0}\frac{dE}{\rho dx} \quad , \tag{4.4}$$

where M is the atomic mass of the target, ρ is the density (mass per unit volume) and N_0 is Avogadro's number.

4.1.2 IMPURITY ION DOSE

The energy axis of a backscattering spectrum and the depth below the surface of a sample are uniquely related to each other by a functional dependence such as that shown in figure 4.4.

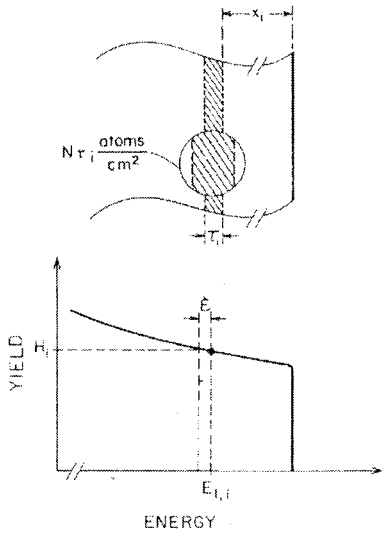

Fig 4.4 Schematic showing the correspondence between a slab at a depth and equivalent energy [52].

Each energy width ξ of a channel i in the multichannel analyzer is thus imaged within the sample by a slab i of thickness τ_i from which all the backscattering events recorded in channel i emanate. The number of counts H_i in the channel i is thus determined by two factors; the thickness τ_i of the slab and the number of scattering centers (atoms) in the slab. Thus we are able to relate the number of counts H_i to the number of scattering centers per unit area $N\tau_i$ in the slab of thickness τ_i at depth x_i, which corresponds to the energy width ξ and the depth E_i of channel i in the energy spectrum.

For a beam of normal incidence, the total number of particles detected in channel i is H_i

$$H_i = \sigma(E_i)\Omega QN\tau_i \quad , \tag{4.5}$$

where $\sigma(E_i)$ is the differential cross section evaluated at energy E_i and averaged over the finite solid angle Ω spanned by the detector, Q is the total number of incident particles on the sample and N is the atomic density of the sample element. Equation 4.5 is appropriate for normal incidence of the beam. For other angles of incidence $\theta > 0$, the number of atoms per unit area as seen by the beam is therefore increased by $\frac{1}{\cos\theta_i}$, so that for this general case:

$$H_i = \frac{\sigma(E_i)\Omega QN\tau_i}{\cos\theta_i} \quad . \tag{4.6}$$

However the total number of counts A is also given as

$$A \equiv \sum_i H_i \quad .$$

Thus

$$A = \sum_i \frac{\sigma(E_i)\Omega QN\tau_i}{\cos\theta_i} \quad . \tag{4.7}$$

For a material of thickness d,

$$A = \frac{\Omega Q N}{\cos \theta_1} \int_0^d \sigma(E)\, dx \quad . \tag{4.8}$$

In the surface energy approximation, the total number of counts is thus:

$$A_0 = \frac{\sigma(E_0)\Omega Q N t}{\cos \theta_1}$$

or

$$Nt = \frac{A_0}{\sigma(E_0)\Omega Q} \cos \theta_1 \quad . \tag{4.9}$$

This provides the number of atoms per unit area Nt without knowledge of the cross-section in the material of interest. The number of impurities per square centimetre can be directly calculated from the area of the signal A given by the total number of counts integrated over the region of interest. For a given impurity denoted by the subscript i, the area A_i can further be expressed for normal incidence

$$A_i = \sigma_i \Omega Q (N t_i) \quad , \tag{4.10}$$

For the surface region:

$$H = \frac{\sigma(E_0)\Omega Q N \tau_0}{\cos \theta_1} \equiv H_0 \quad . \tag{4.11}$$

The thickness τ_0 is defined by the energy width ξ of a channel. The depth scale at the surface is given by:

$$\xi = [\varepsilon_0] N \tau_0 \tag{4.12}$$

where $[\varepsilon_0]$ is the stopping cross-section. Hence

$$H_i = \frac{\sigma(E_0)\Omega Q \varepsilon}{[\varepsilon_0] \cos \theta_1} \quad , \tag{4.13}$$

meaning that the height of the energy spectrum at the surface is a function of the total number of incident projectiles bombarding the sample Q, the average differential cross section σ, between the projectile and the sample evaluated at the incident energy E_0, the solid angle spanned by the detector aperture Ω, the energy width of a channel ξ, and the inverse of the stopping cross-section factor $([\xi_0]\cos\theta_1)^{-1}$, evaluated at the surface for a given scattering geometry multiplied by the *cosine* of the angle of incidence of the beam against the sample normal. Combining equations 4.9 and 4.10, then [49]

$$(Nt_i) = \left(\frac{A_i}{H_{S,0}}\right)\left(\frac{\sigma_S(E_0)}{\sigma_i(E_0)}\right)\left(\frac{\xi}{\varepsilon_0}\right)_s^s \quad . \qquad (4.14)$$

The subscripts s and o refers to substrate and surface energy approximation. Thus for example, the dose of krypton implanted in titanium can be calculated as

$$(Nt)_{kr} = \left(\frac{A_{kr}}{H_{Ti}}\right)\left(\frac{\sigma_{Ti}(E_0)}{\sigma_{kr}(E_0)}\right)\frac{\xi}{[\varepsilon_0]_{Ti}} \quad , \qquad (4.15)$$

where ε_0 is the stopping cross-section factor.

4.1.3 IMPURITY ION CONCENTRATION

The maximum concentration of impurity ions in the sample can be derived from the expression [52]

$$\frac{N_I}{N_S} = \left(\frac{H_I}{H_S}\right)\left(\frac{\sigma_S(E_0)}{\sigma_I(E_0)}\right)\left(\frac{[\varepsilon_0]_I}{[\varepsilon_0]_S}\right) \quad , \qquad (4.16)$$

where N_I and N_s are the atomic densities of the impurity and host ions. H_I and H_s are the peak counts for implanted ions and substrate respectively, $\sigma_s(E_0)$ and $\sigma_I(E_0)$ are the scattering cross-sections at energy E_0. $[\varepsilon_0]_I$ and $[\varepsilon_0]_s$ are the respective stopping cross-section factors.

4.1.4 IMPURITY DEPTH DISTRIBUTION

The depth of impurity ions I in the sample material s is given as [52]

$$N^{s}t = \frac{\Delta E_{I}}{[\varepsilon]_{I}^{S}} \quad . \tag{4.17}$$

where ΔE_I represents the energy width derivable from the backscattering spectrum while $[\varepsilon]_I^S$ is the beam parameter. N is the atomic density of the substrate and t is often represented by R_p, the projected range of the ions in the substrate. A data manipulation package, RUMP [54, 55] is often used for the analysis and simulation of Rutherford Backscattering Spectroscopy data. It consists of series of FORTRAN subroutines.

4.1.5 RBS INSTRUMENTATION

RBS instrumentation essentially consists of an ion source, the accelerator, focusing system, beam line, a voltage source, electron charge stripper, the vacuum system (for the charge stripper and the beam line) and the sample chamber (figure 4.5). The He^{+} ions required for a single ended accelerator come from plasma ion sources. The duoplasmatron starts with a low voltage arc burning between cathode and anode. The helium plasma is geometrically and magnetically confined, and ions are extracted by a strong electric field. The sample chamber components are a stage, one or more detectors, a beam entrance, and the vacuum system.

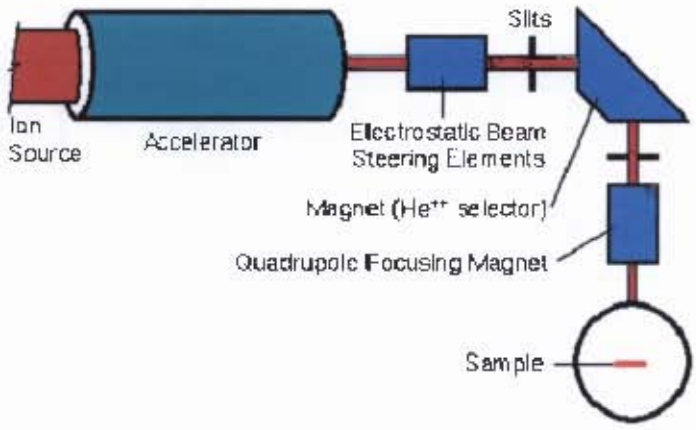

Fig 4.5 Schematic of a Rutherford Backscattering system [56].

The beam line carries the charged particles and it is enclosed in a tank containing high voltage components and an insulating gas. In order to linearize the electronic potentials and to reduce the electric fields between charge components, alternating insulator and conductor sections are connected to the terminal voltage along a resistor chain (see figure 4.6). An additional measure designed to reduce voltage gradients between accelerator components and thereby minimize electric fields, consists of series of smooth conducting rings which are also connected along a resistor chain to the terminal voltage.

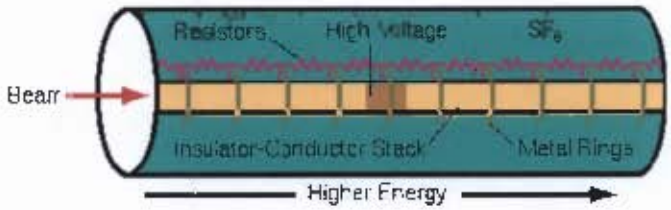

Fig 4.6 Schematic diagram of a beam line [56].

The source of high voltage is the Van der Graaff generator. Its distinguishing feature is charge transfer on a moving belt with one pulley at the terminal and the other at ground. Charge is placed on the belt by a comb of corona points. A second set of points removes the charge at the terminal (Figure 4.7). The traditional Van der Graaf generator is single ended but can be used in a tandem machine.

A well known variation of the Van der Graaff is the Pelletron. It uses a chain with alternative links (pellets) of metal and insulator rather than a belt. The chain provides more uniform charges than the belt, resulting in more stable voltage.

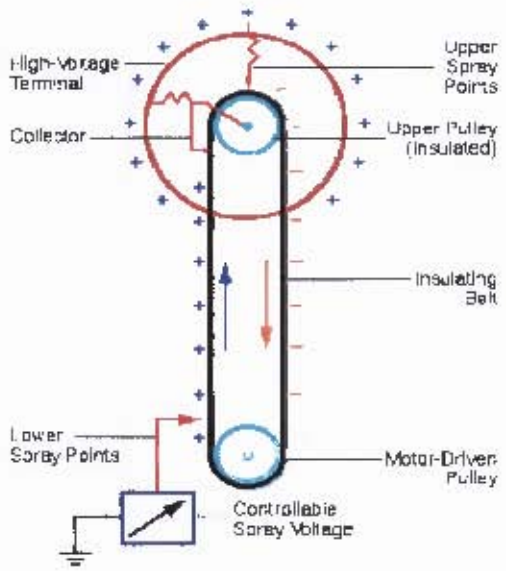

Fig 4.7 Schematic of a Van der Graaff generator [56].

4.2 X-RAY DIFFRACTION STRESS DETERMINATION

X-ray diffraction is a standard method of measuring residual stress [57, 58, 59] in a material. In X-ray diffraction stress measurement, the specimen is bombarded with high energy X-rays which penetrate the sample and diffract according to Bragg's law

$$n\lambda = 2D\sin\theta \tag{4.18}$$

n is an integer, λ is the wavelength of the X-rays, D is the interplanar spacing and θ is the diffraction angle of the X-ray beam. The X-ray detector records the angular positions where X-rays have satisfied Bragg's law and are diffracted. These peaks form the characteristic pattern of the material. Internal stress in the crystal structure of the material can be characterized in terms of its effect on the diffraction pattern. As seen in figure 4.8, if the net strain is non-zero over the illuminated volume which incorporates different grains, there will be a shift in the measured peak position corresponding to the change in average lattice spacing in the direction measured. Such stresses are referred to as macroresidual stresses. It is also possible to have a variation of strain over shorter distances with no net effect in the illuminated volume. This is usually referred to as microresidual stress, and its effect is to cause an angular broadening of the diffraction peak with no change in its position.

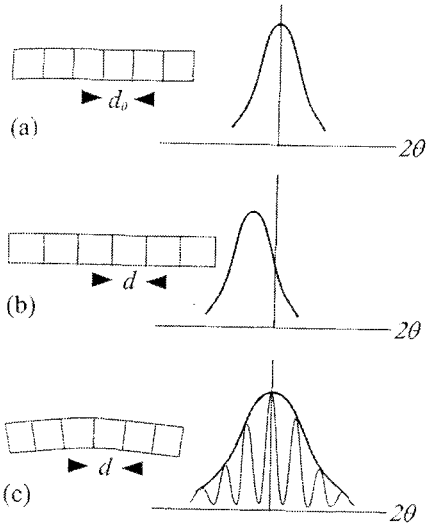

Fig 4.8 Influence of lattice strain on the X-ray diffraction pattern (a) Without strain (b) macroresidual stress (c) microresidual stress. D_0 is the interplanar spacing in equation 4.18 and D represents the straining of D_0 [60].

By utilizing one of these characteristic peaks, usually at as high an angle of 2θ as possible, the strain within the material can be measured by comparing the unstrained inter-planar spacing, D_0 with the strained inter-planar spacing. The shift, $d(2\theta)$ of the peak is proportional to the lattice strain, $\frac{dD}{D_0}$ as [60]

$$d(2\theta) = -2\left(\frac{dD}{D_0}\right)\tan\ \theta_0 \quad . \qquad (4.19)$$

It is easily seen from equation 4.19 that from the measured peak positions $2\theta_{\varphi,\Psi}$ of the diffraction peaks, the lattice strain in the direction φ,Ψ is [60]

$$\varepsilon_{\varphi,\Psi} = -\frac{\cot\theta_0}{2}\left(2\theta_{\varphi,\Psi} - 2\theta_0\right) = \left(\frac{D_{\varphi,\Psi} - D_0}{D_0}\right) \quad , \qquad (4.20)$$

where the angles Ψ and φ are the inclination to the sample normal and the azimuthal rotation around the sample normal respectively (see fig. 4.9)

An X-ray difrractometer for stress analysis is classified as Ψ-diffractometer (figure 4.9) when the specimen axis for the Ψ -tilt is vertical to the diffraction plane during the measurement. The geometrical arrangement for the Ψ-diffractometer is often referred to as side inclination.

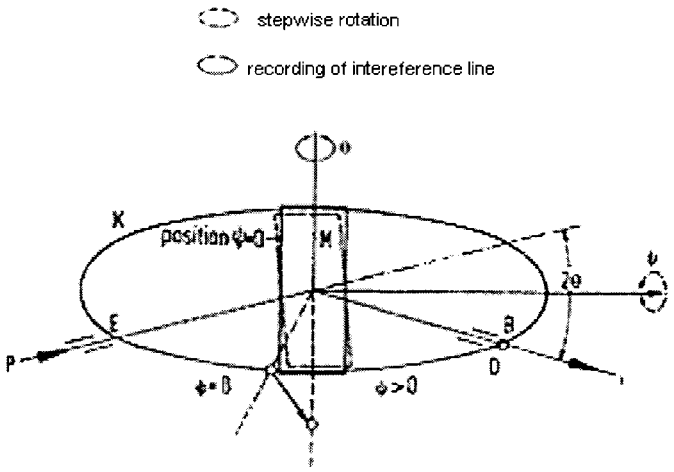

Fig 4.9 Principle of Ψ-difrractometer arrangement [60].

An important procedure usually undertaken in order to achieve accurate result in X-ray measurements is the alignment, usually by mechanical means, and calibration of the diffractometer using stress-free powders of suitable materials. The diffractometer is aligned such that the peak positions or the (hkl) lines of the calibration powder do not differ by more than 0.01^0 in 2θ. Apart from the need for precise peak determination, accuracy in lattice strain determination can be achieved if in the specimen area irradiated by the incident X-ray beam, a sufficient number of grains of the material phase of interest are randomly oriented. This condition is not fulfilled in coarse-grained materials or in materials with preferred orientation of grains.

4.2.1 SIN^{2}Ψ METHOD OF STRESS DETERMINATION

For a specimen in a rotationally symmetric plane state of stress, the so-called $sin^2\Psi$ method is often used for the determination of stress by diffraction measurements [61]. In this method, the peak position of a certain (hkl) reflection is measured at different

specimen tilt angles Ψ. The measured peak positions are used to determine the lattice strain perpendicular to the (hkl) planes at the different tilt angles Ψ.

By a coordinate transformation, the strain $\varepsilon_{\varphi,\Psi}$ in component form ($\varepsilon_{i,j}$; $i = j = 1,2,3$) is defined as

$$\varepsilon_{\varphi,\Psi} = \frac{D_{\varphi,\Psi} - D_0}{D_0} = \varepsilon_{11}\cos^2\varphi\sin^2\Psi + \varepsilon_{12}\sin 2\varphi\sin^2\Psi + \varepsilon_{13}\cos\varphi\sin 2\Psi$$

$$+\varepsilon_{22}\sin^2\varphi\sin^2\Psi + \varepsilon_{23}\sin\varphi\sin 2\Psi + \varepsilon_{33}\cos^2\Psi \quad . \quad (4.21)$$

The indices 1 and 2 refer to directions in the plane of the sample, and index 3 normal to the sample. If the shear components $\varepsilon_{ij}(i \neq j)$ are zero, this equation reduces to:

$$\varepsilon_{\varphi,\Psi} = \frac{D_{\varphi,\Psi} - D_0}{D_0} = \left(\varepsilon_1\cos^2\varphi + \varepsilon_2\sin^2\varphi - \varepsilon_3\right)\sin^2\Psi + \varepsilon_3 \ , \quad (4.22)$$

where $\varepsilon_1, \varepsilon_2, \varepsilon_3$ are the principal strains. Applying Hooke's law to equation 4.22,

$$\varepsilon_{\varphi,\Psi} = \frac{1}{2}S^{hkl}{}_2[(\sigma_\varphi - \sigma_3)\sin^2\Psi + \sigma_3] + S_1{}^{hkl}(\sigma_1 + \sigma_2 + \sigma_3) \ . \quad (4.23)$$

The constants $S_1{}^{hkl}$ and $\frac{1}{2}S_2{}^{hkl}$ are the X-ray elastic constants [62] which are independent of Ψ and can be calculated for each reflection (hkl) using a grain interaction model. Grain interaction models are used to describe the distribution of stresses and strains over the crystallographically oriented crystallites in a specimen. Examples of such models include Voigt [63], Reuss [64], Nerrfeld-Hill [65] and Eshelby-Kroner [66]. In an isotropic medium, the constants can be written in terms of Young's Modulus E and Poisson's ratio υ:

$$S_1{}^{hkl} = -\frac{\nu}{E} \ ,$$

and

$$\frac{1}{2}S_2{}^{hkl} = \frac{1+\nu}{E} \ .$$

The assumption of a biaxial stress state, which is essentially a surface stress state, is crucial to the application of the $sin^2\Psi$ method. Under this assumption $\sigma_3 = 0$ and equation 4.20 can therefore be expressed as

$$\varepsilon_{\varphi,\Psi} = \frac{1+\nu}{E}(\sigma_\varphi \sin^2 \Psi) - \frac{\nu}{E}(\sigma_1 + \sigma_2) \quad . \tag{4.24}$$

The stress components σ_φ in the direction φ is given by

$$\sigma_\varphi = \sigma_{11} \cos^2 \varphi + \sigma_{22} \sin^2 \varphi \quad . \tag{4.25}$$

Equation 4.21 represents a linear function of $\sin^2 \Psi$ and hence by plotting the lattice strain $\varepsilon_{\varphi,\Psi}$ against $\sin^2 \Psi$, the stress σ_φ can be derived from the slope of the line. Thus the bi-axial stress is estimated with appropriate values of ν and E. This is the basis of the so-called "$\sin^2 \Psi$ method".

CHAPTER 5

EXPERIMENTAL METHODS

5.1 SAMPLE DESCRIPTION

Thin, disk shaped polycrystalline titanium samples of 99.6% purity, supplied by GoodFellow Ltd. were used in this study. Each is of diameter 25 mm and thickness 0.3 mm. The samples have been previously rolled and annealed by the supplier, and each weighs 0.691 gramms.

Krypton implantation was performed, using an ion implanter at the University of Witwatersrand, Johannesburg, Republic of South Africa. Two titanium samples were each implanted at energy of 170 KeV: one with a krypton dose of $1x10^{16}/cm^2$ and the other with $5x10^{16}/cm^2$. During the implantation, the temperature of the target was maintained at the ambient level using a water circulation system for the target holder. The implantation current density was *2.7* $mAcm^{-2}$. The implanted samples were not subjected to any form of treatment after the implantation.

The main techniques used to characterize the samples and to investigate the effects of implantation are Rutherford Backscattering Spectrometry diffraction stress determination respectively. The morphology of the samples was investigated with the aid of optical and scanning electron microscopy.

5.2 RUTHERFORD BACKSCATTERING SPECTROMETRY

The purpose of RBS was to determine whether the implanted samples actually contain the expected doses of implanted krypton, and to determine the depth of krypton penetration in these samples. The analysis was performed with a single ended Van der Graaf generator at iThemba LABS, Faure, South Africa, which uses a 2 MeV He^+ beam. The general protocol for RBS experiments can be described in three steps: (1) to produce a clean sample that is contaminant free; (2) to perform the actual RBS coverage measurements, including calibration; (3) to analyze the RBS data using ion scattering spectrometry software.

Calibration is usually carried out, using standard samples such as SiO_2/Si, Ir/Si or Ti/Si and these three were used in this work. The objective of the calibration procedure is to determine the channel-energy conversion factor, which is an important input parameter for RUMP [67] computer package. RUMP is a commercial software package used to simulate the spectral data and to determine the absolute elemental density as a function of depth.

Both the calibration and titanium samples can be loaded on the sample holder, usually called the ladder. The ladder used is able to accommodate seven experimental samples at the same time during measurements. In our case, the calibration samples, and the two krypton implanted titanium samples were loaded on the ladder, and thereafter transferred to the sample chamber. A typical set up of the sample chamber is shown figure 5.1.

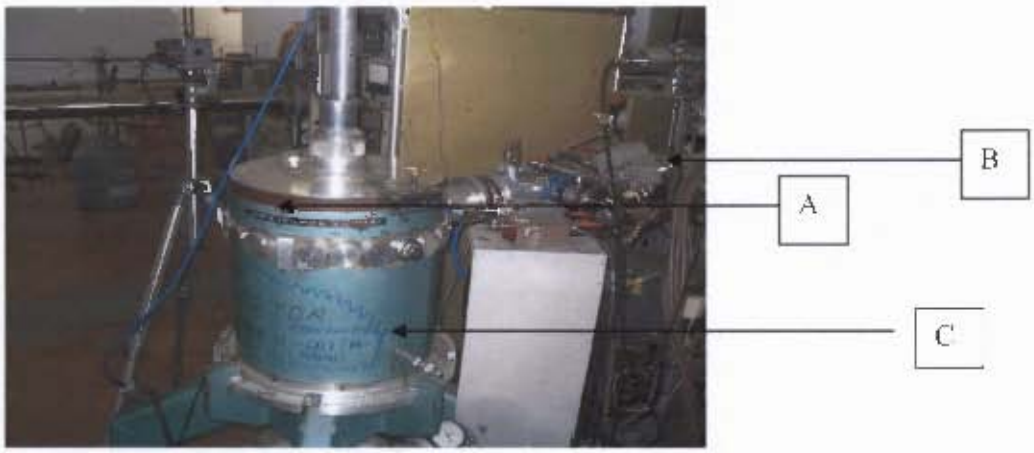

Fig 5.1 A typical set-up of the RBS sample chamber. A is the goniometer; C is the sample chamber enclosing the detector; B is the beam line [68].

The sample chamber is an enclosure which contains a stage for holding the ladder, the beam entrance, a detector and the vacuum system. The vacuum system ensures that the chamber is free of any contaminants, which might affect through collision, the incoming He^+ beam, thereby reducing its energy. After the chamber is closed, A 2 MeV helium beam, at a current of 35nA and a total charge 10μC, was incident on the sample at an angle of 10^0. The energy spectra of the scattered radiation were recorded using a surface barrier detector at a constant scattering angle of 165^0. Under these conditions, the typical

measurement time for each sample is about 19 minutes and the maximum depth probed in titanium is approximately 100 nm.

The raw data acquired are saved in ASCII format and are then imported into RUMP for analysis. Inputs to the RUMP program include the model layers, beam energy, the ion species, ion concentration and its thickness in a layer, integrated incident charge, detector solid angle, energy-channel conversion factor, and energy resolution. Our model is a three layer system consisting of titanium/titanium-krypton/titanium layers. At this point, RUMP can produce a simulation of the expected spectrum. The krypton, being heavier and concentrated in the near surface region, should therefore appear as a peak to the right of the main, continuous, titanium spectrum.

5.3 XRD PHASE ANALYSIS

Before the stress state of titanium samples could be investigated, it was necessary to examine their phase composition. This was carried out using a BRUKER AXS D8 ADVANCED diffractometer [68] (shown in Fig 5.2).

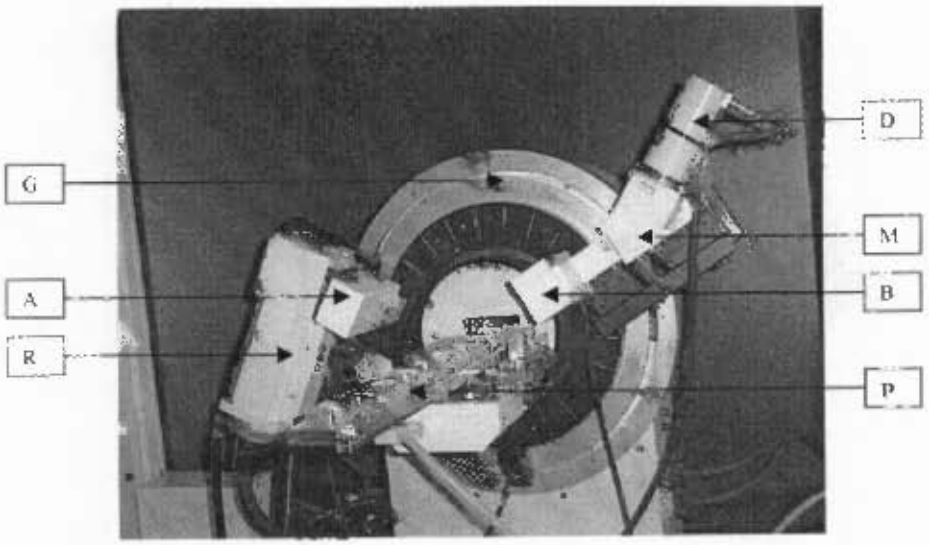

Fig 5.2 BRUKER AXS D8 ADVANCED diffractometer used for phase analysis: R-X- ray tube housing with the tube, A-divergence slit, G-vertically-oriented goniometer, D-Detector, M-monochromator, B-antiscatter slit, P-automatic sample magazine [68].

The set-up of the system can be divided into three sections: the primary side, the secondary side and the sample stage. The primary side consists of a fixed anode copper tube which acts as radiation source housed inside the tube *R*. It was possible to operate the tube either in point or line focus mode. For the present purpose, it was operated in line focus mode. Attached to the tube is a divergence slit system *A* which can be adjusted to modify the incident beam.

The secondary side consists of the antiscattering slit system *B*, the monochromator *M*, and the scintillation detector *D*. The scintillation detector detects the scattered radiation; the graphite monochromator mounted in front of the detector selects a CuK_{α} wavelength beam and the antiscattering slit system B defines the diffracted beam.

The sample stage is an automatic platform with nine sample slots, which may be fully occupied during measurements. The loaded samples continuously rotate horizontally under X-ray illumination. The X-ray is focused in Bragg-Brentano geometry (see figure 5.3). Hence, the diffraction vector is fixed perpendicular to the sample surface. Consequently, all orders of diffraction for a given (hkl) plane will come from the same crystallites since they will have the right orientation to diffract. In figure 5.2, radiation emerging from the X-ray tube *R* impinges on the sample *P* and is scattered into the detector D. Both the source and the detector are fixed in position throughout the duration of measurement and this position is defined by the imaginary focusing circle, which equally touches the sample surface. The sample is mounted at the centre of the difrractometer.

For the unimplanted sample, the diffraction pattern was recorded over a 2θ range from 20^0 to 145^0, with a step size of 0.009^0 and a measuring time of 8s per step. The total measurement time was about 31 hours. For the implanted samples however, the 2θ range varied from 20^0 to 129^0, with a step size of 0.02^0 and a measuring time of 8.5s per step. The measurement time was about thirteen hours. It should be mentioned that we do not expect additional crystallographic reflections resulting from krypton implantation. The reflection peaks are expected to be the same for both implanted and unimplanted samples. All the raw data obtained were corrected for $K\alpha_2$ and background contributions. This was done with the aid of a routine in the DIFFRAC^{plus} EVA program.

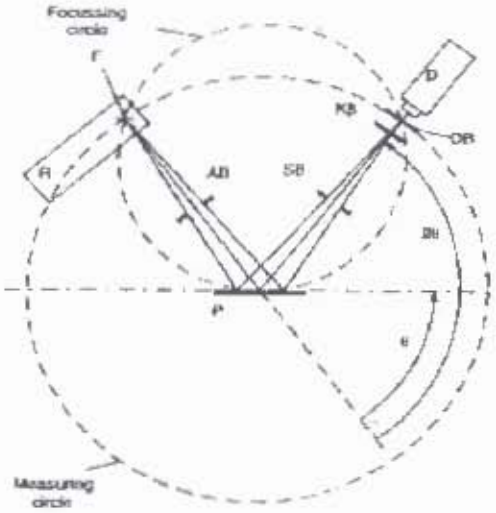

Fig 5.3: Schematic illustrating beam path for X-ray phase analysis diffractometer: AB- Divergence slit, D-detector, DB-detector slit, F-focus, P-sample, R-X-ray tube. SB-anti-scatter slit, $\theta - 2\theta$ -incidence angle-diffraction angle and Kβ - filter [69].

5.4 XRD STRESS DETERMINATION

X-ray stress measurements were performed using a BRUKER–AXS D8 DISCOVERY diffractometer [68] (shown in figure 5.4).

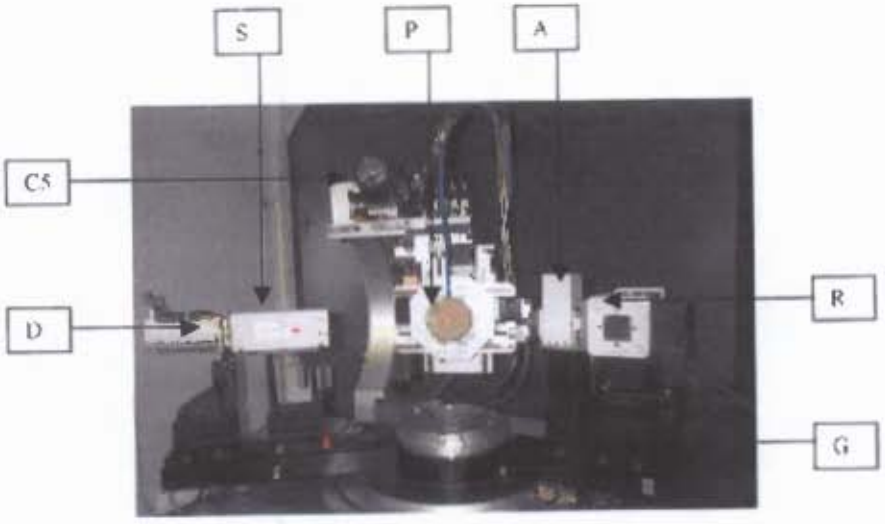

Fig 5.4 BRUKER D8 Discovery X-ray Diffractometer: R- X-ray tube, A-divergence slit, P-sample stage, S-long soller slit, D-Detector, G-horizontally-oriented goniometer [62].

The configuration of this equipment can also be divided into three parts: the primary side, the secondary side and the sample stage. The primary side consists of a copper X-ray tube which serves as the source of radiation. A 1mm diameter short collimator is mounted on the divergence slit system *A* which is in turn mounted in the front of the tube housing *R*. Both the collimator and the divergence slit *A* define the incident beam. The secondary side includes a long Soller slit *S* with divergence of 0.4^0 which ensures that a near parallel-diffracted beam reaches the detector. Behind the Soller slits is a 15μm Nickel filter for suppressing unwanted K_β radiation. The measurement sample is positioned in the sample holder which is then mounted on the sample stage *P*, prior to the commencement of the measurement.

Strain measurements were carried out with the equipment shown in figure 5.4, using filtered CuK_α radiation at 40 KeV and 40 mA. Four different reflection peaks were used: (101), (102), (103) and (213). These correspond to Bragg angles of 20.1^0, 26.5^0, 35.4^0 and 69.7^0 respectively. The sample was tilted in side inclination mode, at 10^0 intervals, up to 70^0 ($\sin^2\Psi = 0.883$), and 75^0, 80^0, 82^0, 84^0, 86^0, 88^0, 89^0 ($\sin^2\Psi = 0.999$). At high values of Ψ, the beam is nearly parallel to the surface and so does not penetrate deeply, allowing very near surface stresses to be probed. In contrast, at low Ψ, the whole region up to the maximum X-ray penetration depth is probed. It is assumed the sample is isotropic in the plane of the surface, and this was not expected to change as a result of implantation. Consequently, only one φ orientation was measured. Moreover, the measurement time for one reflection at the precision required was typically three weeks. The side-inclination mode ensures that unwanted effects, such as defocusing are avoided during tilting. Throughout the measurement, the tube was near the sample to ensure maximum intensity and improve convergence of the beams.

5.5 DATA PROCESSING

Measured peaks from X-ray strain measurements are superpositions of contributions from $K_{\alpha 1}$, $K_{\alpha 2}$ radiations and background radiation. However only contributions from $K_{\alpha 1}$ are useful in peak determination, hence the need for corrections to reduce, or totally eliminate the contribution from such unwanted radiation sources. This was done with the

aid of a routine within the DiffracPlus software. The corrections are categorized as follows:

- Background correction which eliminates scattered intensity not contributing to the diffraction line
- Smoothing which reduces the effect of counting statistics and finally:
- Alpha2 correction which eliminates scattered intensity due to $K_{\alpha 2}$ radiation.

All the raw data had the same systematic corrections applied. Figure 5.6 is a typical diffraction peak at tilt angle $\Psi = 88^0$ with raw, smoothed and $K_{\alpha 1}$ curves.

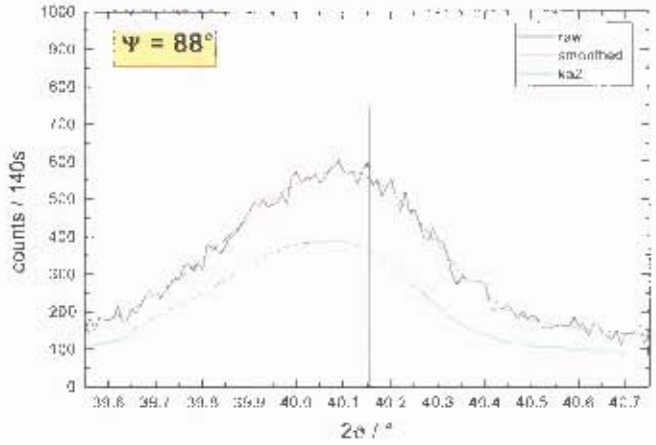

Fig 5.6 A typical diffraction peak showing the effect of corrections. The 'raw' curve was 'smoothed' and 'alpha2' correction made to obtain the smooth $K_{\alpha 1}$ curve.

The resultant peaks, after processing, were analyzed using the instrument software package (DIFFRAC^{plus}STRESS). This package supports several methods of locating the position of the diffracted peaks. These are: sliding gravity, centre of gravity, parabolic fit and Pseudo-Voigt fit methods. The sliding gravity has thresholds of 10, 20, 30, 40, 50, 60, 70, 80 %; centre of gravity has 30% and parabolic fit has 80%. A threshold is a peak intensity cut off point, data below which is not used in the fitting procedure. For example, in the centre of gravity method, a threshold of 30% means that the top 70% of the data was used in the peak fitting routine. This method is accurate and is used in locating the peaks. The final stress values were calculated by fitting straight lines through the data points.

5.6 METALLOGRAPHIC TECHNIQUE

The objective of the metallographic technique was to gain insight into the microstructure of the as received titanium sample. Information about grain sizes and other microstructural features can be accessed through this technique.

The sequences of operations undertaken consisted of sample cutting, mounting, grinding and polishing, etching and finally observation under light microscope.

5.6.1 Sample Cutting and Cold Mounting

A previously cut sample was cold mounted. Since our sample is small and will be subsequently subjected to grinding and polishing operations, there was a need to hold it safely during these operations, hence the need for cold mounting. Cold mounting requires very simple equipment which consists of a cylindrical ring as the mould and a flat piece of glass which serves as the base of the mould. The sample was placed on the glass within the cylinder and a mixture of powder filler and liquid resin poured in and allowed to set, a process which took about 40 minutes.

5.6.2 Grinding and Polishing

The purpose of grinding was to remove all the blemishes on the sample and to achieve a flat sample surface. Grinding was done with the aid of rotating discs, covered with silicon carbide, and water. There are number of grades of paper. These are usually quoted as 220, 600, 800, 1000, and 1200, corresponding to the number of mesh lines per linear inch used to grid the grit. The 220 grade therefore represents the coarsest particles and the grinding operations started with this grade and subsequently higher grades. The final grinding operation was with 1200 paper and the sample was then washed in water followed by alcohol and later dried before moving to the polisher.

The polisher consists of rotating discs covered with soft cloth impregnated with diamond particles (3 and 0.25 microsize) and an oily lubricant. Polishing started with the 3 micron grade and continued until all the grinding scratches were removed. The sample was then

thoroughly cleaned with soapy water, followed by alcohol before commencing with the 0.25 micron size.

5.6.3 Etching

Grinding and polishing operations usually produce a highly deformed layer in the surface, which can be removed chemically during etching. The etchant is able to attack the surface with preference for those sites with the highest energy, leading to surface relief, thus allowing different crystal orientations, precipitates, grain boundaries phases and defects to be distinguished in reflected light microscopy. Sodium hydroxide was used as the etchant. The sample was later observed under light microscope interfaced with a computer. Data processing was done with the aid of LEICA DC100 processing software

CHAPTER 6

RESULTS

6.1 SCANNING ELECTRON MICROSCOPY (SEM)

Scanning Electron Microscopy was used to investigate the surface morphology of the titanium samples. Three titanium samples were investigated: one as-received, pure and unimplanted and two krypton implanted samples at doses $1x10^{16}$ Kr^{+}/cm^{2} and $5x10^{16}$ Kr^{+}/cm^{2}.

Figure 6.1 is an image, taken in secondary electron mode, of as-received pure unimplanted titanium. Evident in this image are several regions of discontinuities typified by darker cavities and lighter flaking regions. These constitute surface roughness and are presumably a result of machining and shaping operations, such as, pressing, rolling or drawing. Also visible are a series of parallel ridges with a spacing of about 0.5μm, resulting from the rolling of the material.

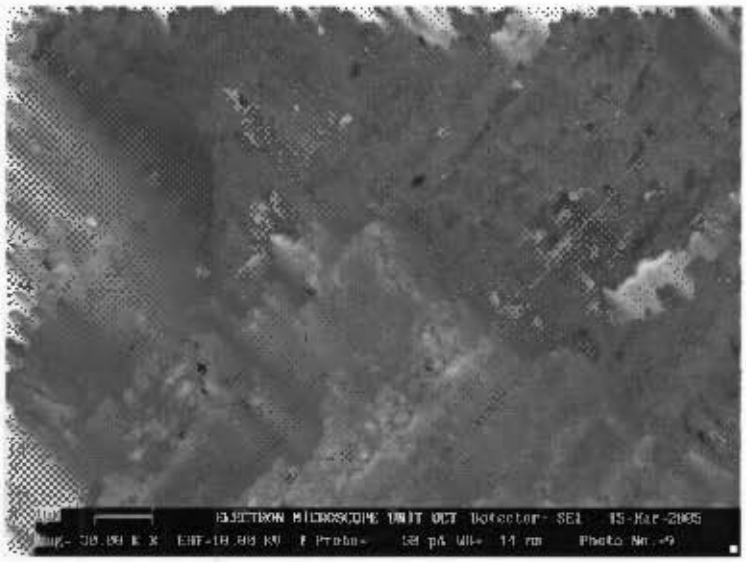

Fig 6.1 SEM micrograph of the surface of unimplanted titanium sample.

Figure 6.2 is a similar image of a surface of titanium after implantation with $1x10^{16}/cm^2$ krypton ions. Figure 6.3 is the corresponding image of the titanium sample implanted at $5x10^{16}$ $/cm^2$. In both figures, the surface structure is more pronounced when compared with figure 6.1. However, there is no qualitative difference between the three images, except for a different contrast which is probably due to instrumental factors. It can be concluded that at these doses, there is no significant blistering resulting from krypton or vacancy agglomeration.

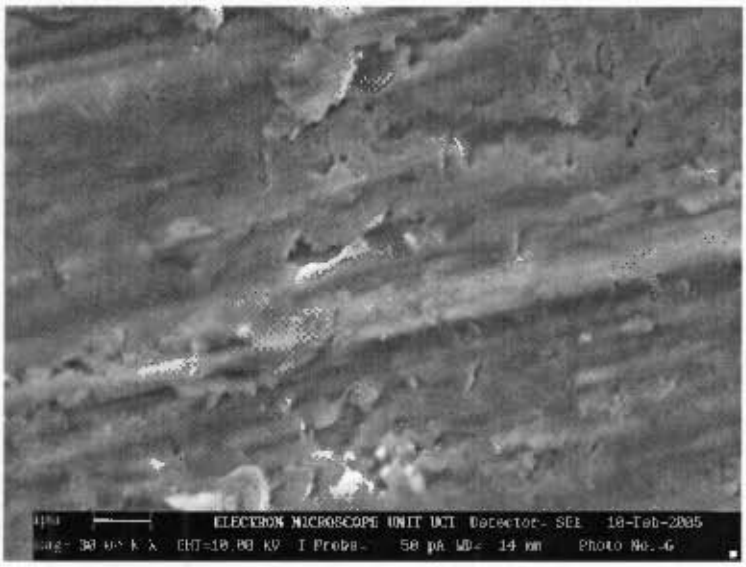

Fig.6.2 SEM micrograph of the surface of krypton implanted titanium at a dose of 1 x10^{16} Kr^+/cm^2.

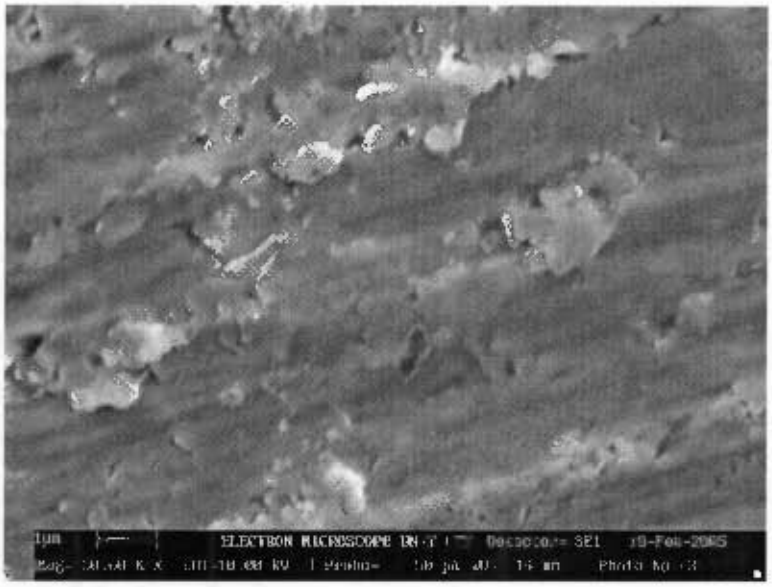

Fig.6.3: SEM micrograph of the surface of krypton implanted titanium at a dose of $5x10^{16}$ Kr^{+}/cm^{2}.

6.2 METALLOGRAPHIC TECHNIQUE

Figure 6.4 is the micrograph of the unimplanted titanium sample as observed under an optical microscope after preparation as described in chapter 5.6. The grain size is non-uniform, varying from between 5 μm to 15 μm. An additional feature, as revealed in the image, is the occurrence of series of closely spaced, almost parallel bands of broad lines that cut across the grains. These are thought to be twin bands and are an evidence of plastic deformation [29]. Possible origins of twinning are shaping and machining operations such as pressing, cutting, or rolling.

Fig 6.4 Optical micrograph of unimplanted titanium after polishing and etching of the surface.

6.3 RUTHERFORD BACKSCATTERING SPECTROMETRY

Figure 6.5 is the spectrum of the unimplanted sample, while figures 6.6 and 6.7 are the RBS spectra of the two titanium samples implanted with krypton at doses of $1x10^{16}$ Kr^{+}/cm^{2} and $5x10^{16}$ Kr^{+}/cm^{2} respectively. Using the RUMP computer package [67] and with a two layer model structure consisting of titanium oxide/titanium, the solid curve in figure 6.5 was modelled to match the experimental curve as closely as possible. The oxide layer thickness was assumed to be 30 nm thick with oxygen concentration of 2 at. %. The oxygen is seen as a small kink on the broad modelled titanium spectrum, at energy of approximately 0.7 MeV.

Figures 6.6 and 6.7 were modelled with a three layer structure consisting of titanium/titanium-krypton/titanium layers. The broad part of the spectrum identifies the titanium substrate as an effectively infinite continuum with cut-off energy of about 1.4 MeV corresponding to the minimum energy loss given by the kinematic factor as discussed in chapter 4.1.1. The wavy, solid curve is the raw RBS spectrum while the smooth curve is the model spectra. In both RBS spectra, the presence of krypton is seen as a smaller peak to the right of the titanium edge at 1.7 MeV. This peak is more visible in the sample implanted at a krypton dose of $5x10^{16}/cm^{2}$. Figure 6.6 was modelled, by

assuming titanium of thickness 35 nm for the first layer, 50 nm thickness of titanium for the second layer with krypton concentration of 3 at.%, and an infinite thickness of titanium for the third layer. The depth of krypton penetration was then estimated to be 99 nm. Figure 6.7 was modelled with titanium of thickness 10 nm for the first layer, the second layer with titanium thickness of 85 nm and 8 at.% krypton, and the third layer is of titanium of infinite thickness. The depth of krypton penetration is estimated to be approximately 90 nm.

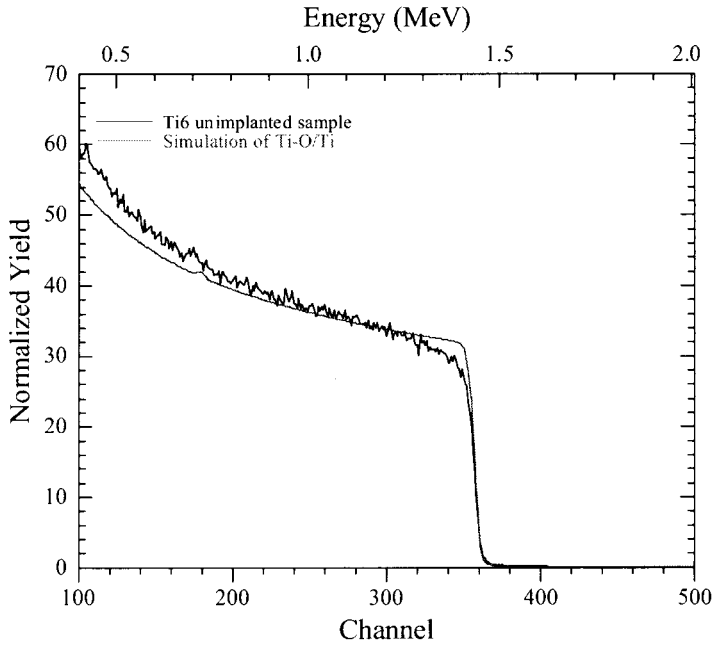

Fig 6.5 RBS spectrum and modelled curve for the unimplanted sample

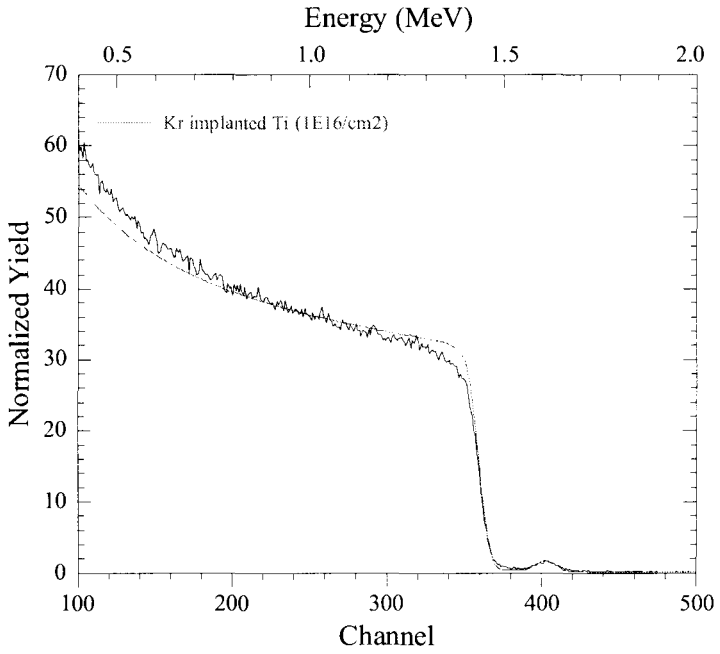

Fig 6.6 RBS spectrum and modelled curve of the titanium sample implanted with krypton at a dose of $1x10^{16}/cm^2$.

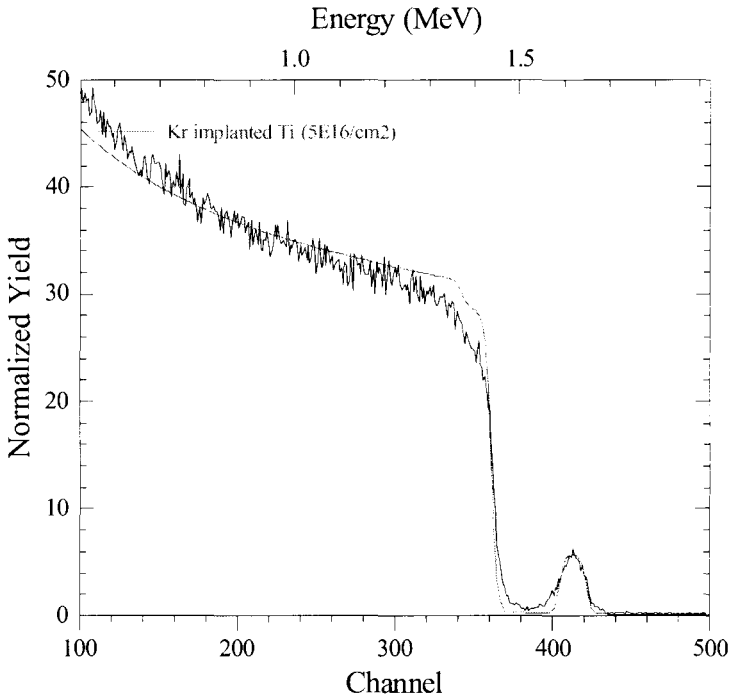

Fig 6.7 RBS spectrum and solid curve of the titanium sample implanted with krypton at a dose of $5\ x10^{16}/cm^2$

6.4 TRIM SIMULATION

TRIM-2003 [26] calculations were carried out for krypton implantation into titanium target using 20000 ions. Figure 6.8 shows the calculated titanium vacancy profiles and the distribution of implanted krypton ions in the titanium target. The total damage was 1648 vacancies per projectile ion. An estimate of the projected range of krypton penetration reveals the depth to be about 64 nm. Also evident in the figure is that, the projected range of implanted krypton extends beyond the peak concentration of titanium vacancies which is approximately 50 nm.

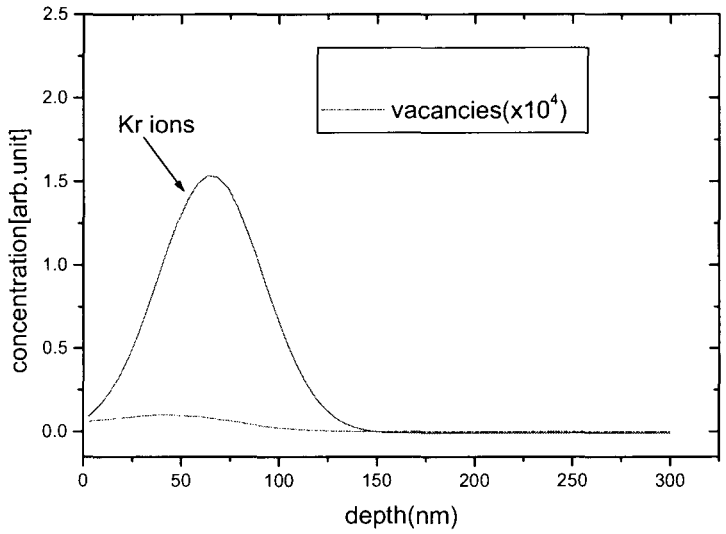

Fig 6.8 TRIM-2003 simulation of implanted krypton (170keV) and titanium damage profiles.

6.5 XRD PHASE ANALYSIS

To obtain structural information on all samples, implanted and unimplanted, a θ - 2θ scan over a wide 2θ angle (20^0-149^0) was carried out using the difrractometer and measurements conditions described in chapter 5.3. Figure 6.9a shows the diffraction pattern of the unimplanted titanium sample. The reflection peaks are consistent with those for single phase, pure titanium as contained in the powder diffraction file (PDF) [70]. It should be noted that the (302) diffraction peak, which corresponds to $2\theta = 148^0$ is

missing from this figure. This is due to instrumental factors, as the maximum scan angle allowed by the machine and its software is 145^0.

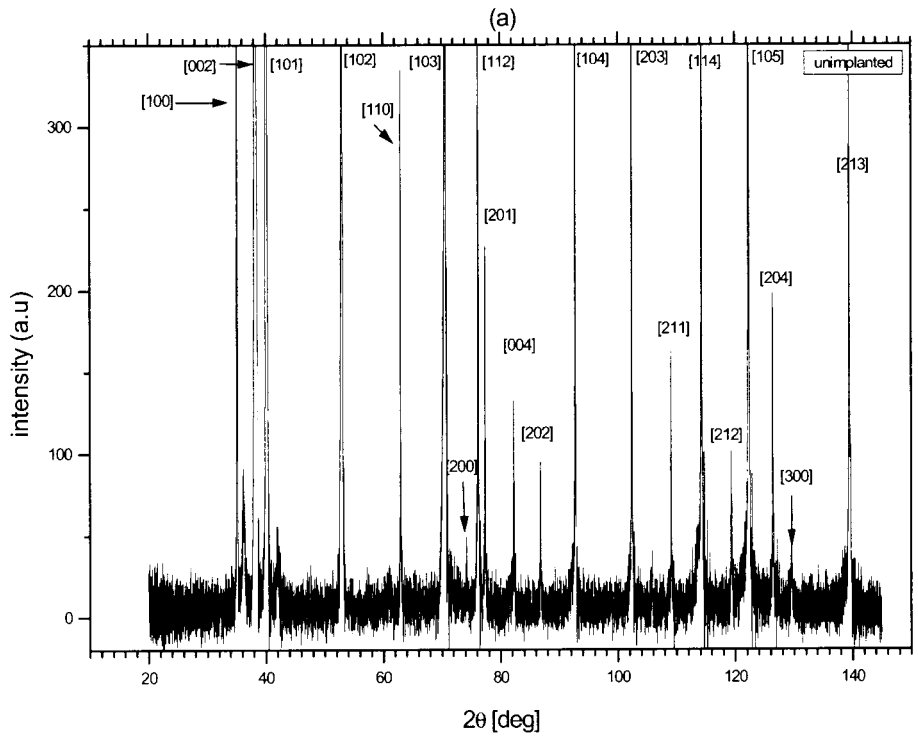

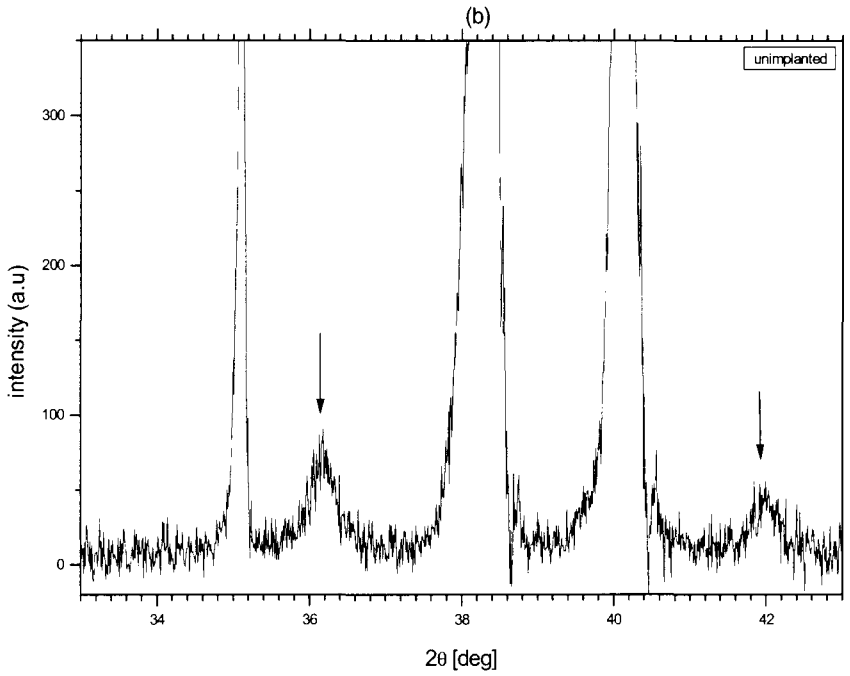

Fig 6.9 XRD-Phase analysis for the (a) unimplanted titanium sample (b) same unimplanted sample, but with an expanded scale to show the peak positions at $2\theta = 36.3^0$ and 42^0, as indicated by arrows.

Apart from the very high intensity reflection peaks shown in the figure, there are additional peaks of relatively low intensities present in the background. Among these, the peaks at $2\theta = 36.3^0$ and $2\theta = 42^0$ are more pronounced, and are shown on an expanded scale in figure 6.9b. These are thought to be contributions from the near surface, chemically stable oxides and contaminants.

Figures 6.10a and 6.11a are phase analysis scan results obtained for the titanium samples implanted with $1x10^{16}\,Kr^+/cm^2$ and $5x10^{16}Kr^+/cm^2$ respectively. In both figures, there are no obvious differences in the diffraction patterns and certainly no additional crystallographic phases resulting from the implantation. This is to be expected, since the concentration of the implanted krypton in the depth probed by the X-rays is extremely low (in the ppm-range). Secondly at these low implantation doses, high density clustering

which can form solid precipitates is not expected [71]. Comparing these two figures with the phase analysis scan for the unimplanted sample (figure 6.9a), there is a visible difference in the absolute count intensity between the three measurements. This is simply as a result of the different measuring time as described in chapter 5.3, and has no physical significance.

Also, a visible reduction in the intensity of some reflection peaks, resulting from the implantation is observed. This is best illustrated with the reflection peaks at $2\theta = 36.3^0$ and $2\theta = 42^0$. Compared with the unimplanted sample, the intensity of these two reflection peaks have been reduced by more than 50 %, due to implantation with $1x10^{16}$ Kr^+/cm^2 (figure 6.10b). The reflection peak at $2\theta = 36.3^0$ almost disappeared to the background in the sample implanted with $5x10^{16}Kr^+/cm^2$ (figure 6.11b). The reduction in the intensity of these peaks is a suggestive of a possible decrease in the concentration of their source through the sputtering process during krypton implantation. We may thus conclude that the near surface contaminants as represented by these two peaks are reduced, or removed by the implantation at these doses.

It is also observed that the relative intensity of the [101] and [103] reflections are nearly the same for the unimplanted and the sample implanted with a dose of $5x10^{16}Kr^+/cm^2$. However for the titanium sample implanted with a dose of $1x10^{16}Kr^+/cm^2$, for the same reflection peaks, the relative intensity is much higher. This suggests a preferred orientation or texturing of the lattice grains in the sample.

Finally, it should be noted that the peak positions of titanium reflections show some variations between the three samples. This is the basis of X-ray stress determination as discussed in the next chapter.

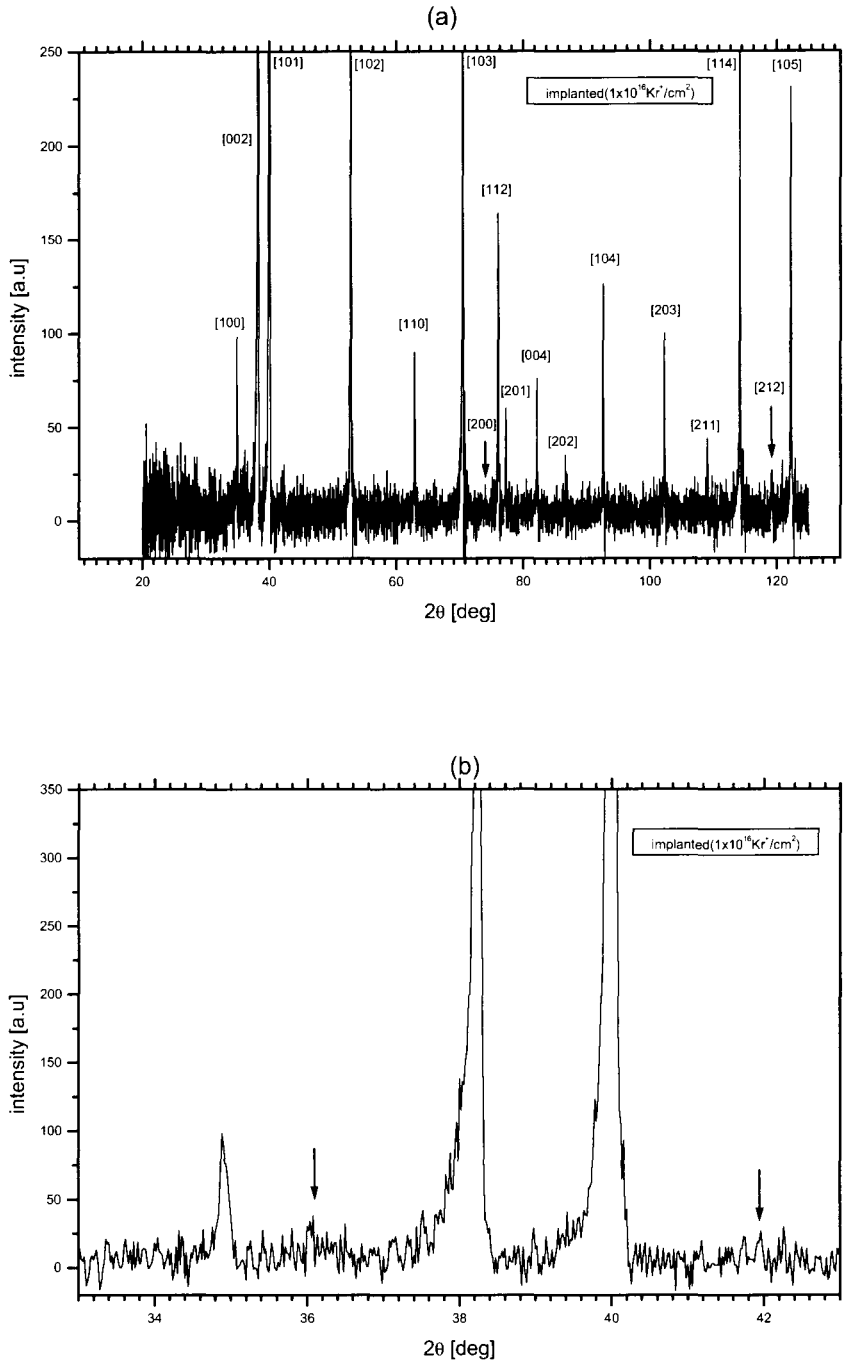

Fig 6.10 XRD phase analysis for the sample implanted with (a) $1x10^{16}$ Kr/cm^2 (b) the same implanted sample but with an expanded scale to show peak positions at $2\theta = 36.3^0$ and 42^0, as indicated by arrows.

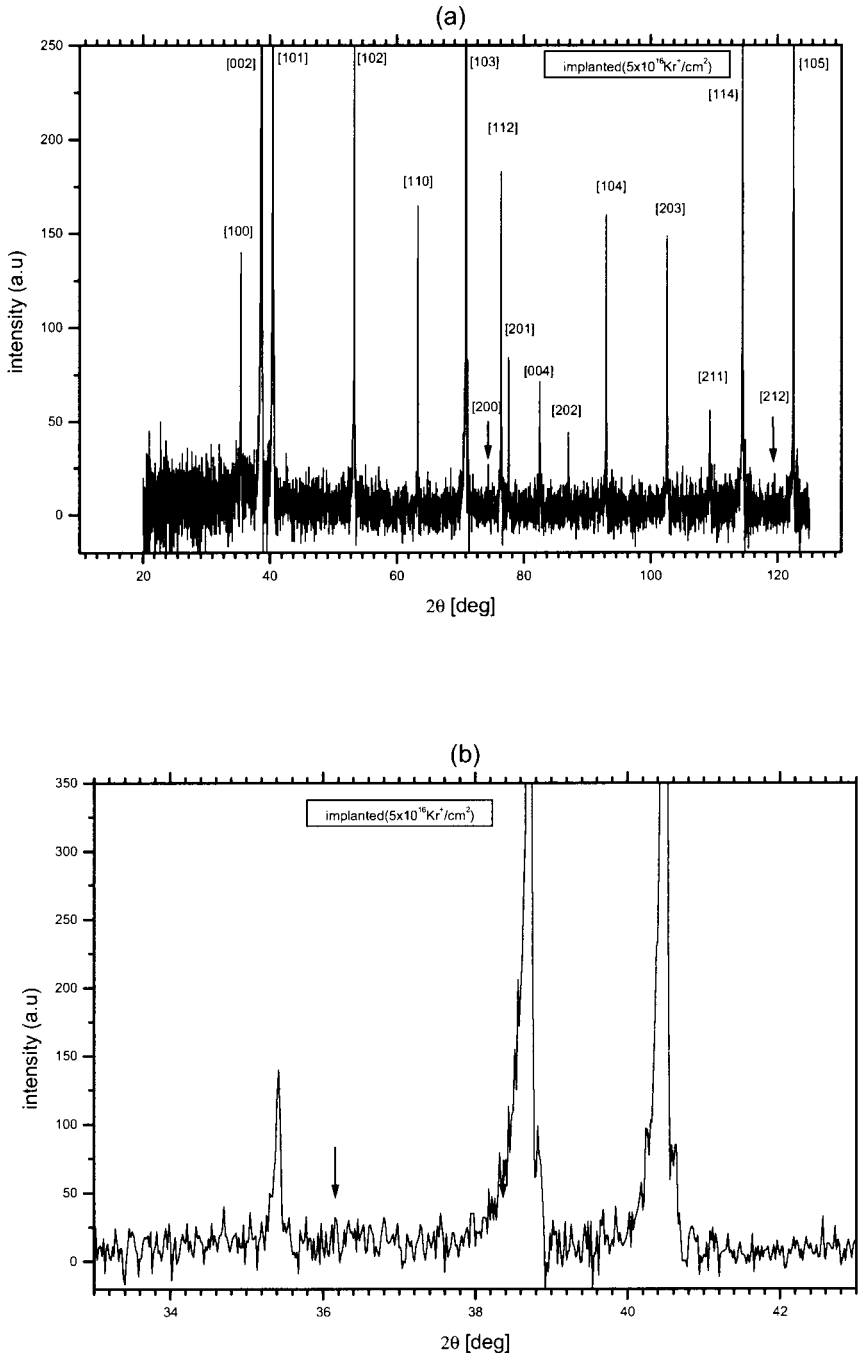

Fig 6.11 XRD phase analysis for the sample implanted with (a) $5x10^{16}$ Kr/cm^2 (b) same implanted sample but with an expanded scale to show peak at $2\theta = 36.3^0$ as indicated by arrow. The peak at 42^0 is no longer visible.

6.6 STRESS DETERMINATION

Four reflection peaks: (101), (102), (103) and (213) corresponding to Bragg angles: 20.1^0, 26.5^0, 35.4^0 and 69.7^0 respectively were selected for residual stress determination, using the X-ray diffraction stress diffractometer and the measurement conditions described earlier in chapter 5.4. Measurements were carried out on one unimplanted titanium sample and two implanted samples with Ψ-tilt angles ranging from 0^0 - 89^0. All the raw data were processed according to the procedure described in chapter 5.5.

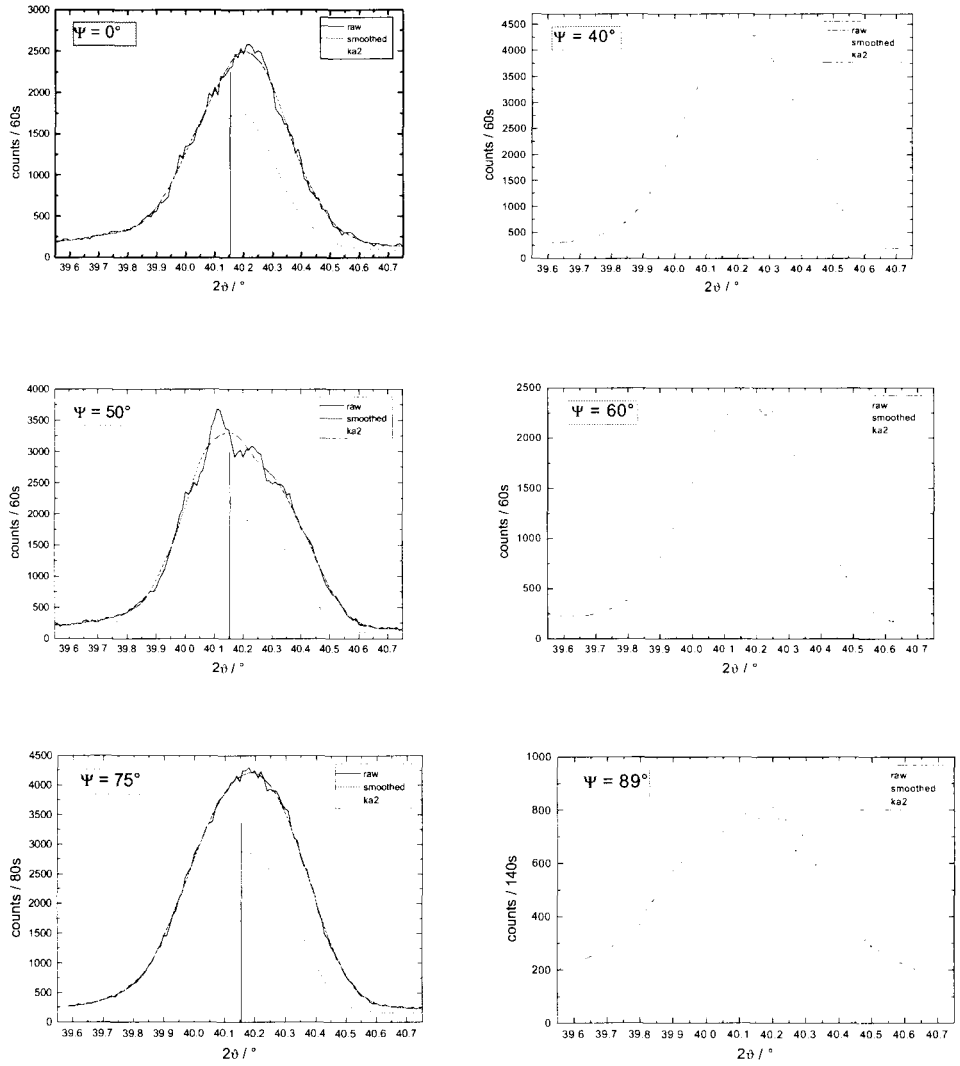

Fig 6.12 Diffraction pattern of [101] reflection at a different Ψ tilt angles for the titanium sample implanted at a dose of $1x10^{16}$ Kr/cm^2.

Figure 6.12 illustrates the angular displacement and broadening of the diffraction peaks from the (101) planes as the Ψ-tilt angles increases for the sample implanted with a krypton of dose $1x10^{16}/cm^2$. The vertical line at the centre of the figures each indicates the 2θ angle for stress free titanium according to the PDF file, and is a reference by which the shifts in the peak position can be observed. Similar peaks of other lattice planes for other samples are shown in appendix A.

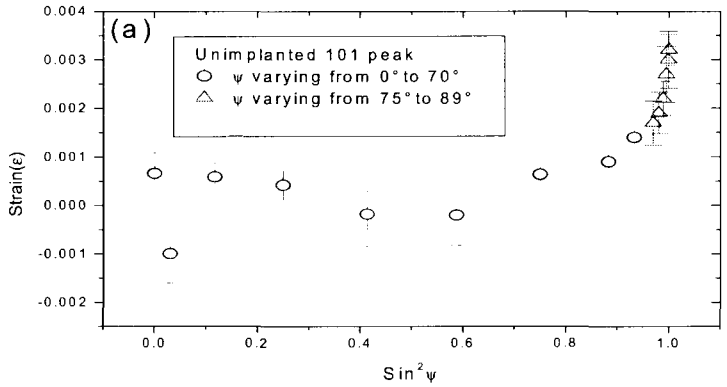

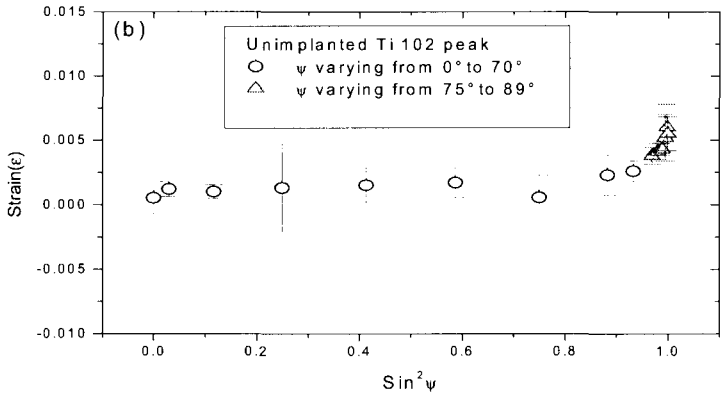

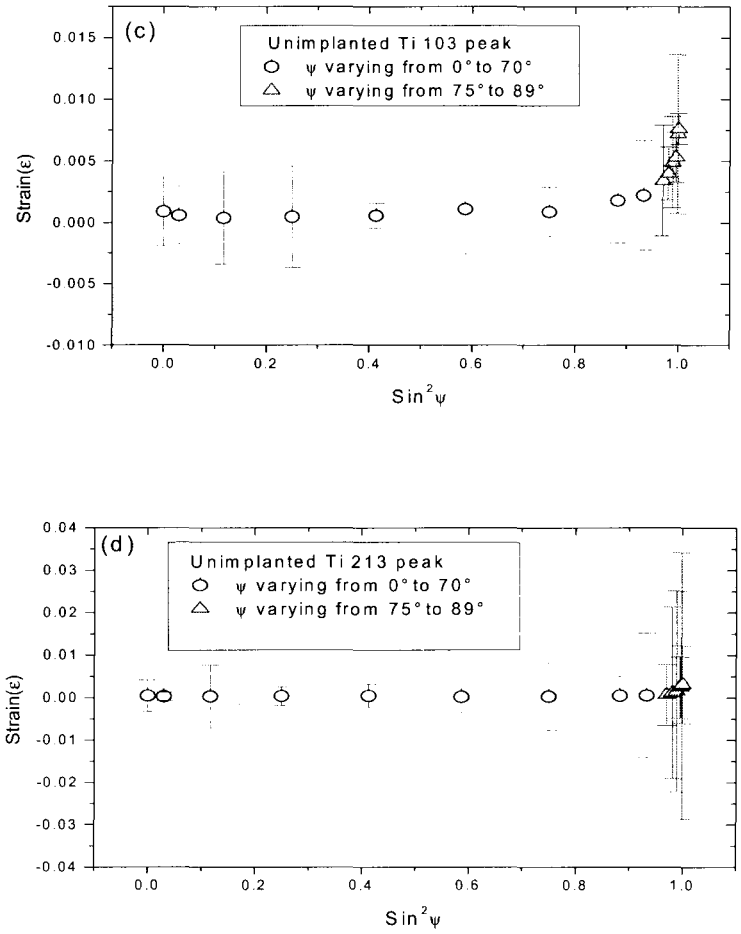

Fig 6.13 (a-d) $sin^2\Psi$ curves for (101), (102), (103) and (213) lattice plane for the unimplanted titanium sample.

The strains for each lattice plane are calculated according to equation 4.20 of chapter 4, and are then plotted against $sin^2\Psi$. Such curves are commonly referred to as the "$sin^2\Psi$ curves". Figures 6.13 (a-d) are $sin^2\Psi$ curves obtained for (101), (102), (213) and (103) lattice planes in the unimplanted titanium sample. Each of the curves consists of two distinct regions: the earlier part corresponding to tilt angle of up to 70^0, at 10^0 intervals, represent the stress state in the bulk, while the latter part corresponding to tilt angle of between 75^0 to 89^0 represent the stress state near the surface.

In all the $sin^2\Psi$ curves (figure 6.12 (a-d)), the strong curvature at high Ψ angles of 75^0 ($sin^2\Psi$ = 0.933) to 89^0 ($sin^2\Psi$ = 0.999) is an indication of high tensile stress near the

surface. For $\Psi < 70$ ($\sin^2\Psi < 0.883$), the stress becomes less tensile or increasingly compressive. The observed stress gradient is a well known effect in residual stress studies of polycrystalline materials, and implies a variation of the stress with depth [72]. It should be mentioned that, due to the continuous absorption of X-rays in the material, it is not possible to define a discrete change in gradient, which could occur anywhere between $\sin^2\Psi = 0.883$ and $\sin^2\Psi = 0.933$.

To illustrate the effect of krypton implantation on the stress state of the titanium sample, the (102) reflection has been selected and is shown in figure 6.13. In this figure, the two upper curves represent the $\sin^2\Psi$ curves for the two samples implanted at fluences of 1 x 10^{16} Kr^+/cm^2 and 5 x 10^{16} Kr^+/cm^2. The data for the two implanted specimens have each been shifted by a constant amount. The lowermost curve is the $\sin^2\Psi$ curve for the unimplanted titanium sample.

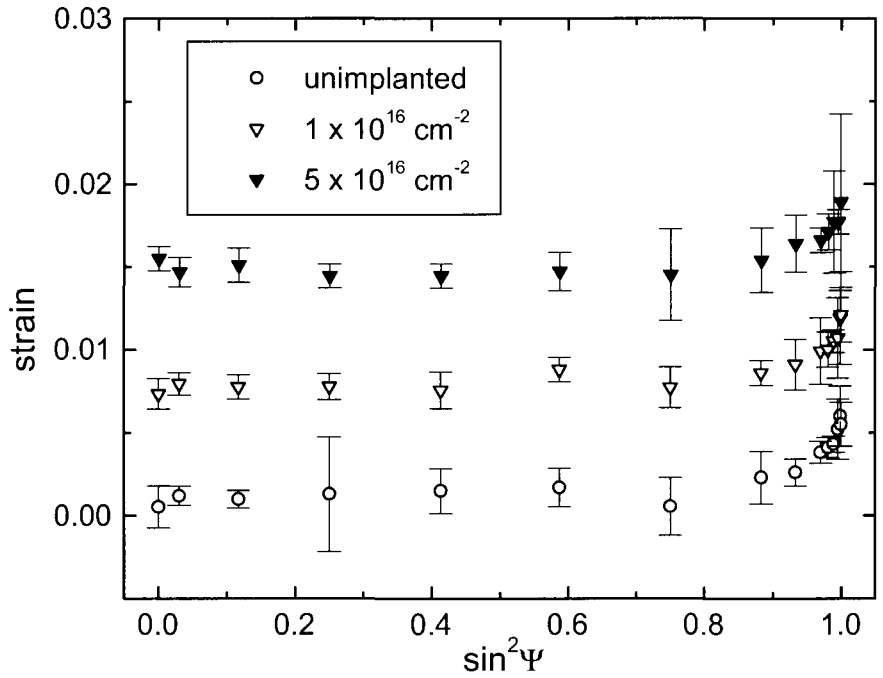

Fig 6.13 $\sin^2\Psi$ curves for (102) reflections of the unimplanted sample and the two samples implanted at fluences of 1 x 10^{16} Kr^+/cm^2 and 5 x 10^{16} Kr^+/cm^2.

At low Ψ-tilts, up to $\sin^2\Psi = 0.4$, the two lower curves, that is, the unimplanted and implanted at 1 x 10^{16} Kr^+/cm^2, have a negligible slope whereas the upper curve has a slight negative gradient. This negative gradient is an indication of an increase in the compressive stress, or a decreasing tensile stress, deeper in the sample. However, at high Ψ-tilts, the increase of the two upper curves, that is of the implanted samples is less than that of the unimplanted sample. This suggests a reduction in near surface tensile stress as a result of krypton implantation. $\sin^2\Psi$ curves of implanted samples for other lattice planes are shown in appendix B.

To calculate the stress magnitudes and the length scales, the $\sin^2\Psi$ curves can be assumed to be a linear superposition of two linear curves weighted with the absorption factor for the X-rays [73]. However, in this work, as an approximation and for simplicity, straight lines were each fitted through the points corresponding to the bulk and the near surface. The stress values were calculated from these slopes using equation 4.20 in chapter 4 with 120 GPa as the Young's Modulus *E*, and 0.361 as the Poison's ratio υ. The results are summarized in *Table 6.1*, along with calculated errors.

For the unimplanted titanium sample, the near surface tensile stress values for the planes (101), (102), (103) and (213) are 2.5 GPa, 3.6 GPa, 7.7 GPa and 4.1 GPa respectively. In the bulk of the material, however, stress values of 110 MPa, 180 MPa, 60 MPa and 10 MPa, are calculated for the same lattice planes.

Table 6.1: Summary of stress values in both implanted and unimplanted samples. Samples Ti5 and Ti4 are implanted with krypton doses of 5 x 10^{16} Kr^{+}/cm^{2} and 1 x 10^{16} Kr^{+}/cm^{2} respectively.

Samples	Stress, σ (Gpa) (101)	Error (Δ σ)	Stress, σ (GPa) (102)	Error (Δ σ)	Stress, σ (GPa) (103)	Error (Δ σ)	Stress, σ (GPa) (213)	Error (Δ σ)
Unimplanted								
Near-surface	2.50	0.62	3.60	0.56	7.70	2.30	4.10	1.03
Bulk	0.11	0.05	0.18	0.05	0.06	0.002	0.01	0.01
Ti5								
Near-surface	2.10	0.11	3.10	1.40	7.70	2.3	0.17	0.16
Bulk	0.06	0.02	0.04	0.06	0.09	0.03	0.04	0.02
Ti4								
Near-surface	1.50	0.18	2.90	1.56	4.00	0.45	1.70	0.75
Bulk	0.07	0.04	0.10	0.03	0.09	0.03	0.04	0.01

The effect of krypton implantation on the stress magnitudes is indicated by the reduction in the near surface tensile stress values in all the lattice planes. For example, in the sample implanted with 5 x 10^{16} Kr^{+}/cm^{2}, the near surface stress values in the (101) plane reduces from 2.5 GPa to 2.1 GPa, and for the sample implanted with 1 x 10^{16} Kr^{+}/cm^{2}, the near surface stress values reduces to 1.5 GPa. In the (102) plane, implantation with 5 x 10^{16} Kr^{+}/cm^{2} slightly reduced the near surface stress value from 3.6 Gpa to 3.1 GPa. The 1 x 10^{16} Kr^{+}/cm^{2} dose reduces the stress value to 2.91 GPa. In the (103) plane, the near surface tensile stress value decreases from 7.7 GPa to 4.0 Gpa due to implantation with 1 x 10^{16} Kr^{+}/cm^{2}. The effect of implantation with higher dose *i.e.* 5 x 10^{16} Kr^{+}/cm^{2} is not apparent, since the stress value remains 7.7 GPa. Also in the (213) lattice plane, the near surface tensile stress value is reduced from 4.1 GPa to 1.7 GPa due to implantation with 1 x 10^{16} Kr^{+}/cm^{2} dose, and to 0.17 GPa as a result of implantation with 5 x 10^{16} Kr^{+}/cm^{2} dose.

In the bulk of the titanium sample, the stress values for (101), (102), (103) and (213) reflections are 110 MPa, 180 MPa, 60 MPa and 10 MPa respectively. As the implantation dose is increased from $1x10^{16}$ Kr^{+}/cm^{2} to $5x10^{16}$ Kr^{+}/cm^{2}, the bulk stress values decreases to 70 MPa and 60 MPa respectively in the (101) plane. In (102) plane, the stress values decreases to 100 MPa and 40 MPa for the same increase in the implantation dose. However, in the (103) and (213) planes, the bulk the stress values increases to 90 MPa and 40 MPa respectively, and these values remain the same, irrespective of the implantation fluence.

CHAPTER 7

DISCUSSION

The as-received titanium sample has been found to be plastically deformed as evidenced by twin bands which cut across the grains. When the material inside a crystal is plastically deformed, there is a change in the internal stress, since the natural change of shape of the deformed region is restrained by its surroundings [74]. The stress state of a given material can be determined by the $\sin^2\Psi$ method of stress determination and this has been described in chapter 5.4. With this method, the stress states in two distinctive regions of the titanium sample were determined. These two regions have been classified as the near surface and the bulk. The near surface is the depth of X-rays penetration from the surface, up to the depth corresponding to the tilt angle for which the slope of a $\sin^2\Psi$ curve changes. The maximum near surface tensile stress has been shown to be 7.7 ± 2.3 GPa. Using the formula [55] for the effective penetration depth of X-rays for the Ψ goniometer, *i.e.* $\tau = \frac{\sin\theta_{hkl}\cos\Psi}{2\mu}$, where θ = 35.4^0(for [103] reflection), Ψ = 75^0 and μ = 912.8/cm are the Bragg angle, the tilt angle and the linear absorption coefficient respectively, this corresponds to tensile stress value within an X-ray penetration depth of 0.82 μm. The bulk refers to the region of the sample where the stress is approximately constant, up to the maximum penetration of the X-rays. For the same reflection, but with Ψ = 70^0 and Ψ = 0^0, this corresponds to the region which lies in between 1.1 μm and 3.2 μm depths below the surface. Here, the stress has been shown to be weakly compressive. The strong stress gradient is expected of a previously rolled material and may result from inhomogeneous plastic deformation during rolling. The calculated near surface tensile stress appears unrealistic, especially when the yield stress and tensile strength of pure titanium *i.e.* 0.48 GPa and 0.62 Gpa respectively [75], are taken into consideration. This is not surprising, as the near surface stress value is estimated from the gradient of steepest part of the $\sin^2\Psi$ curve and this is not expected to give the actual value. However, as a rough guide, this method gives stress magnitudes which indicate the depth dependence of stress state of the sample. A more accurate near surface stress value may be obtained by

assuming the $\sin^2\Psi$ curves to be a superposition of two linear curves weighted with the absorption factor for the X-rays [73]. The full depth dependence of the stress tensor would require a much more complete data set including, in particular, measurements at different azimuthal directions of the sample and this is beyond the scope of this work.

Ion implantation was done on two pre-stressed polycrystalline titanium samples. Each was implanted with krypton at two different doses of 5 x 10^{16}/cm^2 and 1 x 10^{16}/cm^2. Rutherford backscattering spectroscopy gives the maximum depth of implanted krypton to be 90 nm and 99 nm for the high and low dose respectively. This broadly agree with TRIM calculations of the projected range of krypton penetration which show the mean depth to be 64 nm with a straggle of about 30 nm, assuming a Gaussian distribution of implanted kryptons. This is surprising since TRIM calculations do not include secondary effects such as channelling, knock-on and stress induced diffusion, although channelling effects are not expected in a polycrystalline material and knock-on of the implanted species is generally assumed to be negligible. It thus appears that, at room temperature, implanted krypton ions are immobile and their movement is not dependent on the observed stress gradient.

The effect of implanted krypton on the stress state of as–received titanium can be discussed in term of contributions from defects that are created. At low dose implantation, the majority of the defects produced are point defects, such as vacancies and foreign interstitial atoms [48]. Higher dose implantation may introduce complex defects, such as dislocation networks in the material [18]. Monovacancies and vacancy complexes have negative dilatation, while interstitial atoms have a positive dilatation, and are expected to affect significantly the pre-existing stress state. Vacancies production results from collisions between the implanted kryptons atoms and the host titanium atoms, leading to displacement of host atoms from their lattice positions. For the two samples implanted at different fluences *i.e.* 1 x 10^{16} Kr^+/cm^2 and 5 x 10^{16} Kr^+/cm^2, the near surface tensile stress is reduced compared to the unimplanted state, though to a different magnitude. For example, across all the lattice planes, the near surface tensile stress is relaxed by implantation at low fluence *i.e.* 1 x 10^{16} Kr^+/cm^2, but then recovers slightly as the fluence is increased to 5 x 10^{16} Kr^+/cm^2. It can be said therefore, that an

additional source of tensile stress is introduced at high implantation fluence. The decrease in near surface stress by low implantation fluence may be attributed to direct stress relaxation by damage production [14], and stress relaxation by the presence of vacancies [73]. Moreover, the peak vacancy concentration, according to TRIM is approximately at 50 nm depth and this coincides within the track region of ion implantation. We may conclude therefore that the main effect of low dose ion implantation is to induce stress relaxation. The increase in the near surface tensile stress at high implantation fluence may be due to complex defects such as dislocation networks that are produced.

In the bulk of the sample however, the higher implantation dose decreases the tensile stress more, to the extent that the bulk stress state becomes compressive as the implantation dose is increased from 1 x 10^{16} Kr^{+}/cm^{2} to 5 x 10^{16} Kr^{+}/cm^{2}. A possible explanation is that, the increase in compressive stress deeper in the material is necessary to maintain equilibrium with the increasing near surface high tensile stress state for high dose implantation. This is however unlikely at low doses, since the observed stress changes are not in the opposite sense, making equilibrium impossible, unlike like the situation in the high dose. A more likely explanation is that, under the influence of the strong negative stress gradient, vacancies, being a centre of contraction migrate deeper into the material where they may form larger defect clusters. The defect clustering forms a source of additional compressive stress. The absence of any noticeable drift of the implanted krypton may suggest that its configurations are such that it fits into the interstitial spacings of titanium structure in a way that does not allow free diffusion or significant distortion.

In summary, the existing negative stress gradient appears to cause vacancy drift deeper into the sample whereas krypton ions are relatively immobile at room temperature. As vacancies agglomerate, tensile stress is relaxed, but larger defect structures in the track region are sources of additional residual tensile stress.

CHAPTER 8

CONCLUSION

The effect of krypton implantation on the pre-existing stress state of as-received, unimplanted polycrystalline titanium have been investigated, using the well known $\sin^2\Psi$ method of stress determination. Three titanium samples were used: one is unimplanted and the remaining two are each implanted with krypton at doses of 5 x $10^{16}/cm^2$ and 1 x $10^{16}/cm^2$. The initial stress state in the as-received sample has been shown to be strongly tensile, approximately 7.7 ± 2.3 GPa in the first 55 nm below the surface, and weakly compressive deeper into the material. This negative stress gradient has been attributed to inhomogeneous plastic deformation resulting from rolling.

Both TRIM and Rutherford backscattering spectroscopy are in close agreement with respect to the depth of penetration of implanted krypton *i.e* within the first 100 nm, suggesting that at room temperature, implanted krypton atoms are relatively immobile in the titanium structure, and the negative stress gradient has no significant influence on their mobility. TRIM calculations have also shown that ion implantation produces peak vacancies concentration at 50 nm depth. The high near surface tensile stress is relaxed by the low implantation fluence *i.e* 1 x $10^{16}Kr^+/cm^2$, but recovers slightly as the fluence is increased to 5 x $10^{16}Kr^+/cm^2$. Reasons for the decrease in the near surface high tensile stress may include stress relaxation by the presence of vacancies and direct stress relaxation by damage production. The slight increase in the near surface tensile stress may be as a result of possible complex defects, such as dislocation networks that form additional sources of tensile stress.

The bulk stress state becomes slightly more compressive as the implantation dose is increased from 1 x $10^{16}Kr^+/cm^2$ to 5 x $10^{16}Kr^+/cm^2$. Vacancies, under the influence of negative stress gradient, migrate deeper into the material where they agglomerate to form larger defect clusters, and these are thought to be responsible for the increase in the compressive stress.

APPENDIX A:

SHIFT IN REFLECTION PEAKS WITH Ψ-TILT ANGLE FOR UNIMPLANTED AND IMPLANTED TITIANIUM SAMPLES.

101 PEAKS (DOSE: 1 X 10^{16}Kr/cm^2)

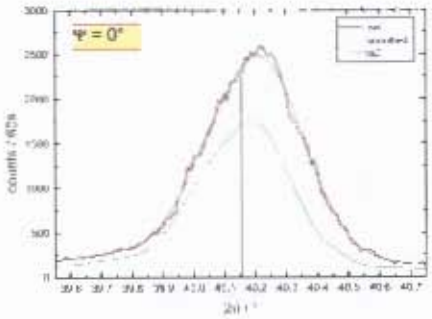

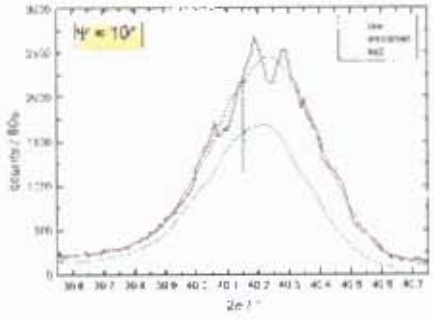

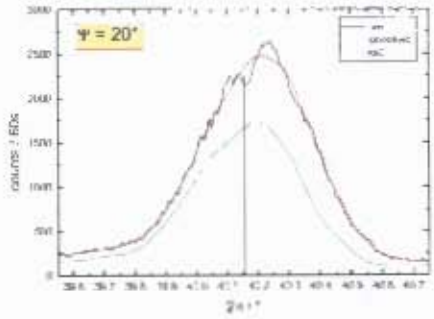

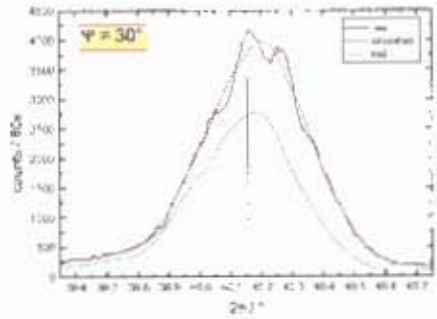

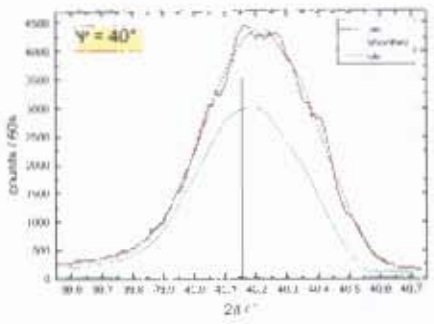
Ψ = 40°
counts / 60s
2θ / °

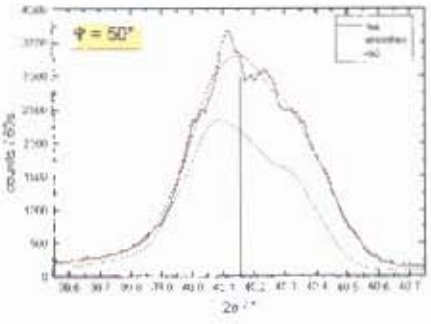
Ψ = 50°
counts / 60s
2θ / °

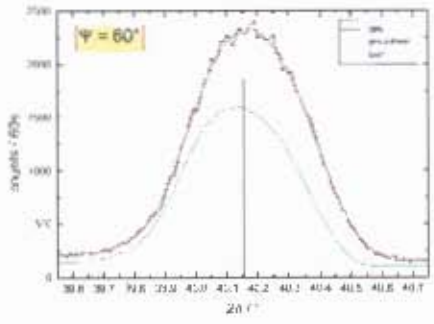
Ψ = 60°
counts / 60s
2θ / °

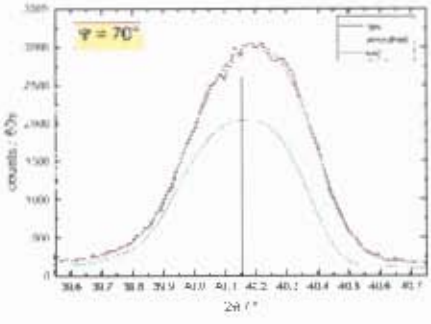
Ψ = 70°
counts / 60s
2θ / °

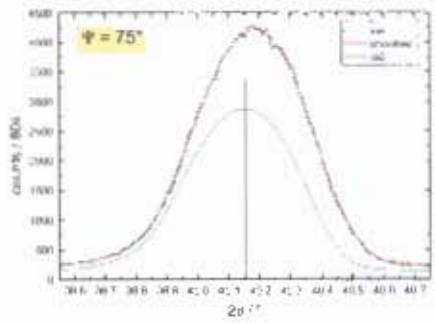
Ψ = 75°
counts / 60s
2θ / °

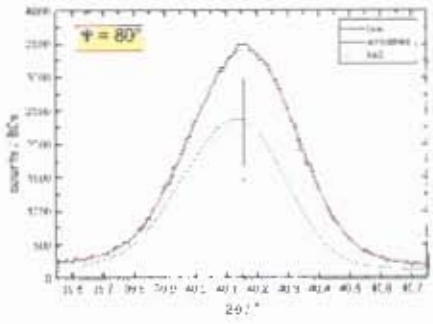
Ψ = 80°
counts / 60s
2θ / °

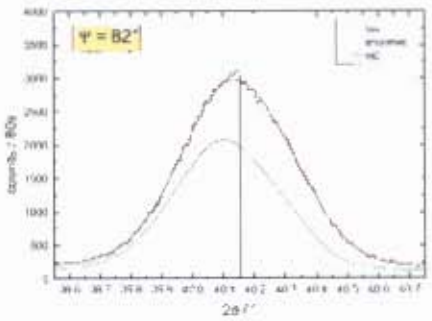
Ψ = 82°
2θ / °

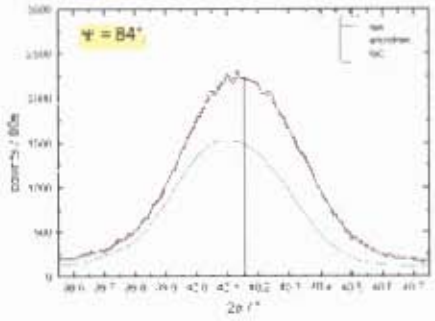
Ψ = 84°
2θ / °

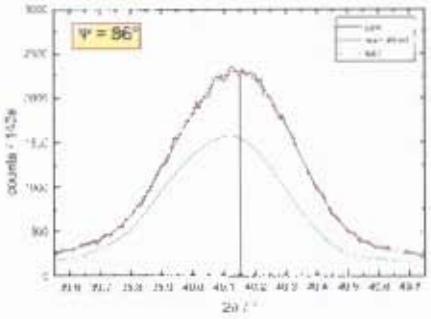
Ψ = 86°
2θ / °

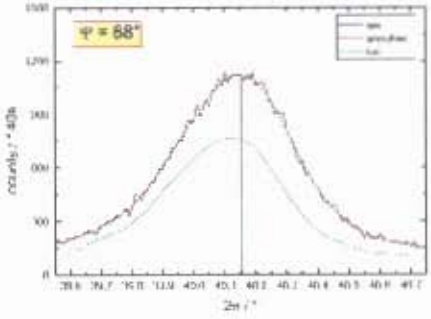
Ψ = 88°
2θ / °

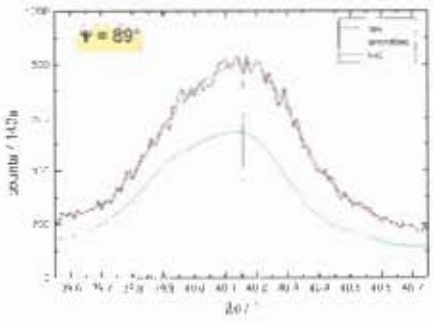
Ψ = 89°
2θ / °

102 PEAKS (DOSE: 1 X 10^{16}Kr/cm^2)

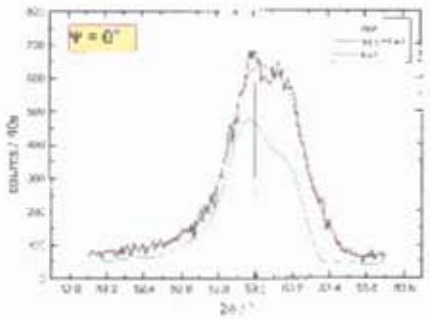

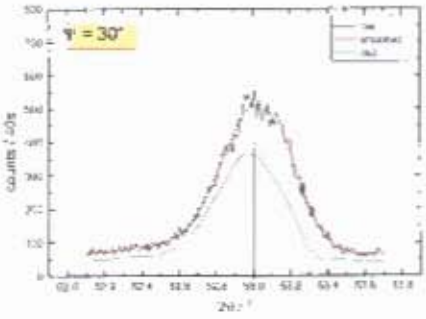

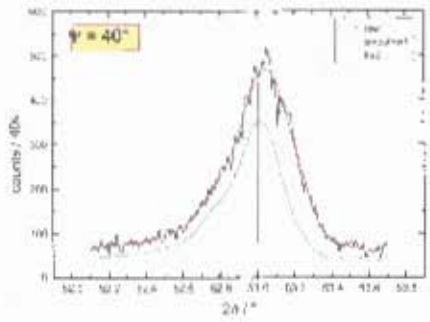

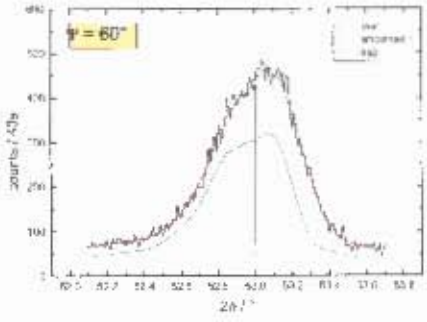

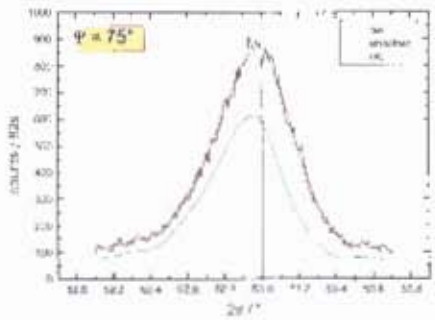

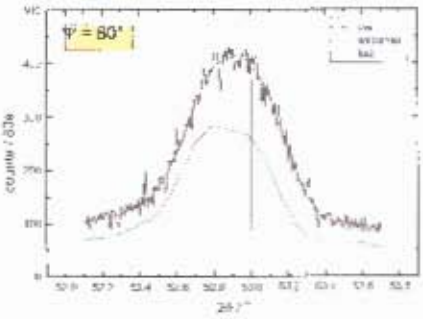

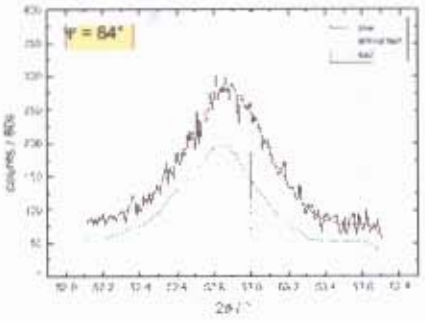

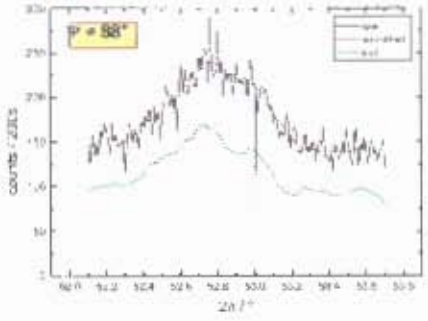

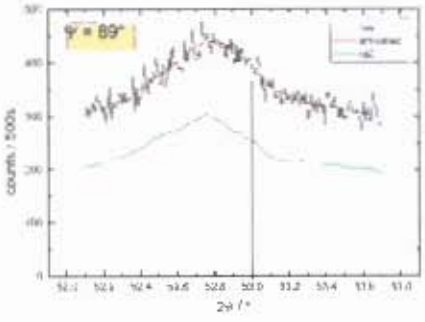

103 PEAKS (DOSE: 1 X 10^{16}Kr/cm^2)

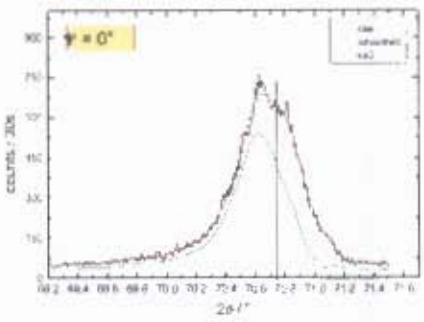
ψ = 0°
counts / 30s
2θ / °

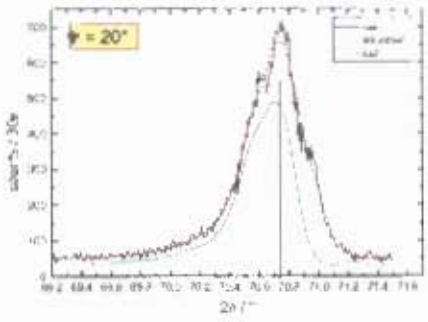
ψ = 20°
counts / 30s
2θ / °

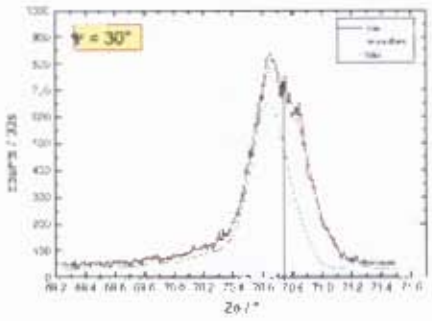
ψ = 30°
counts / 30s
2θ / °

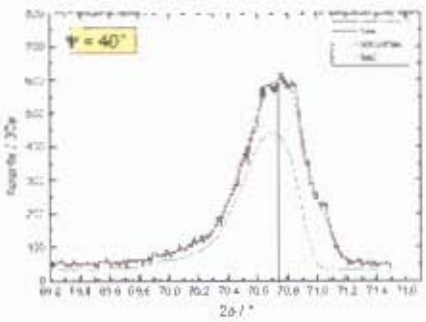
ψ = 40°
counts / 30s
2θ / °

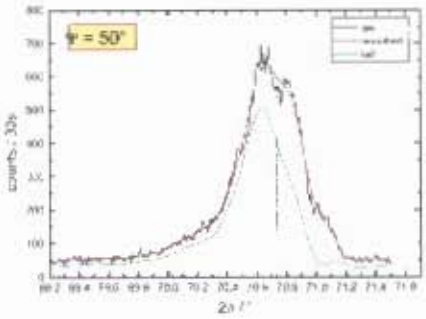
ψ = 50°
counts / 30s
2θ / °

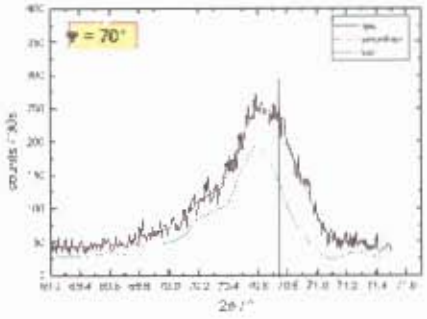
ψ = 70°
counts / 30s
2θ / °

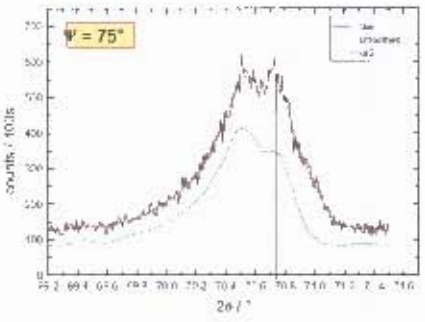
Ψ = 75°
counts / 100s
2θ / °

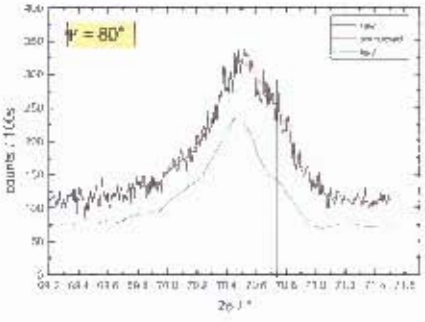
Ψ = 80°
counts / 100s
2θ / °

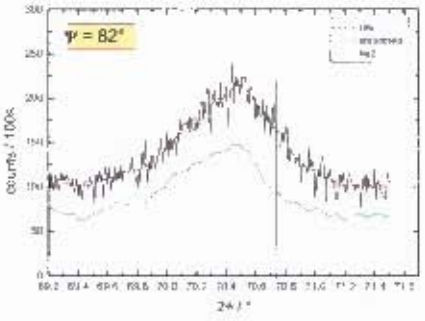
Ψ = 82°
counts / 100s
2θ / °

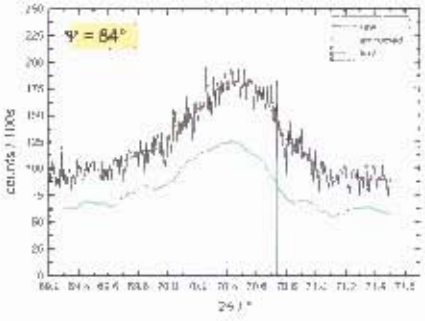
Ψ = 84°
counts / 100s
2θ / °

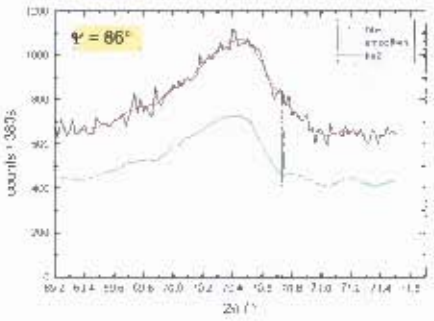
Ψ = 86°
counts / 383s
2θ / °

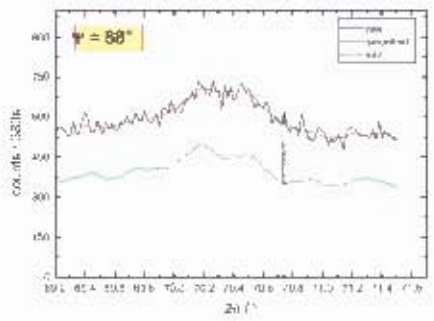
Ψ = 88°
counts / 383s
2θ / °

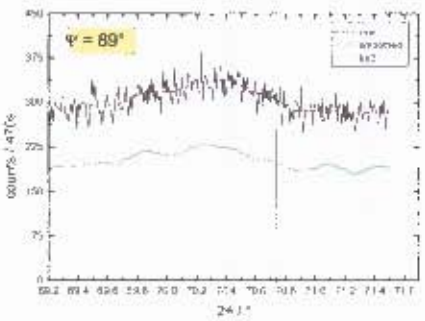
Ψ = 89°
counts / 479s
2θ / °

101 PEAKS (UNIMPLANTED)

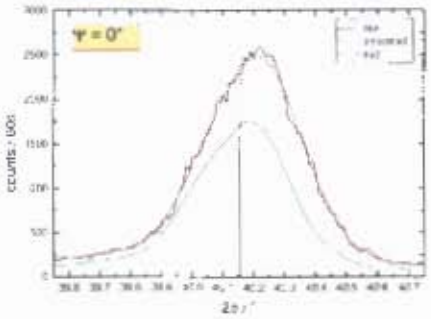

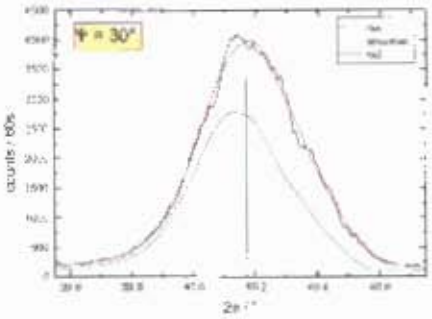

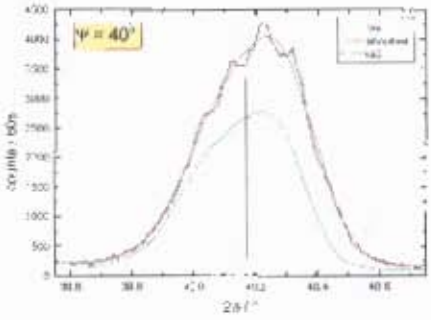

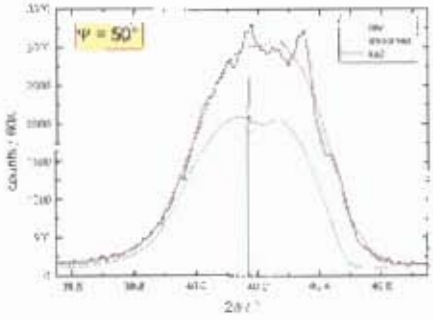

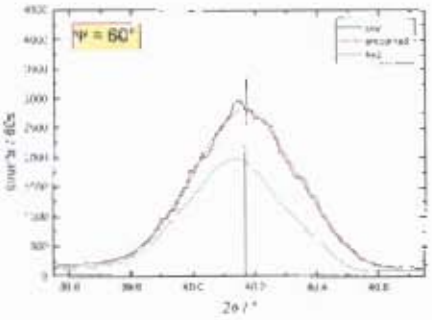

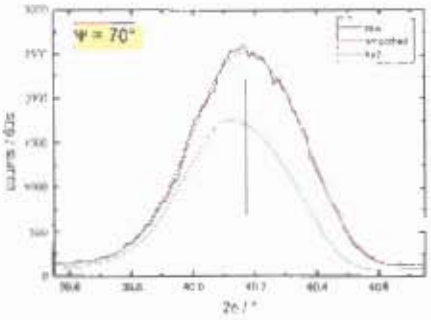

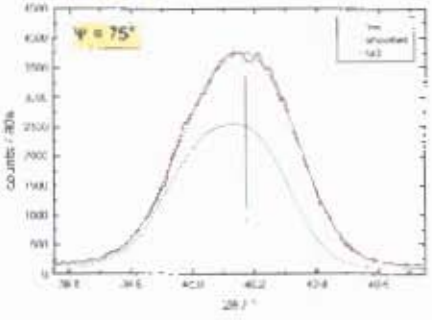

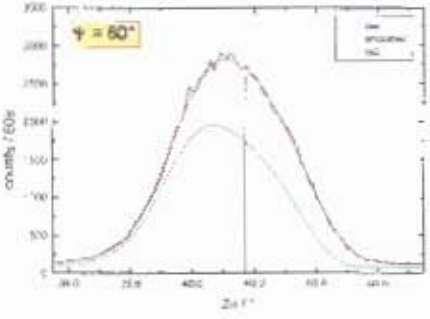

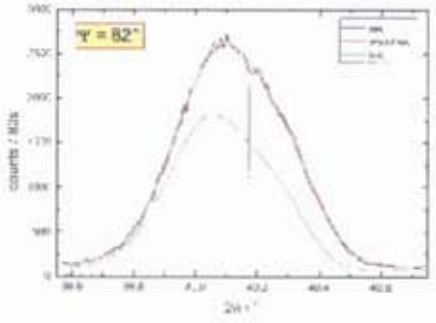
Ψ = 82°

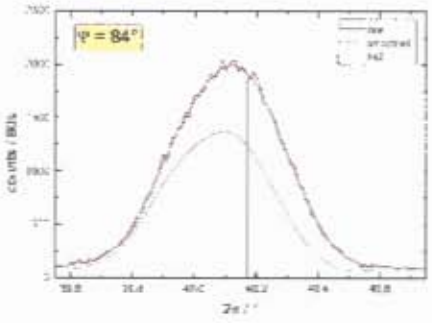
Ψ = 84°

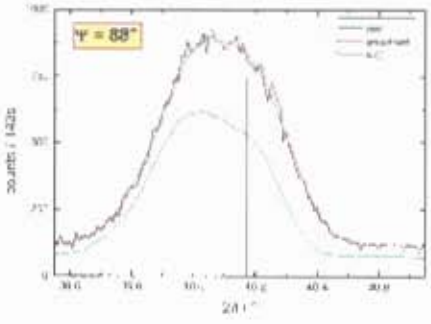
Ψ = 88°

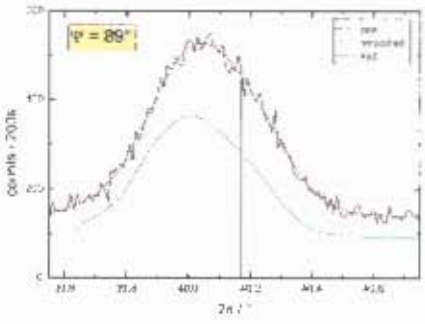
Ψ = 89°

102 PEAKS (UNIMPLANTED)

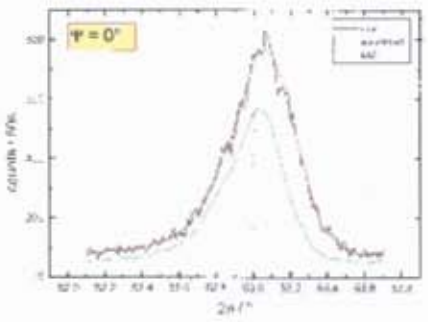

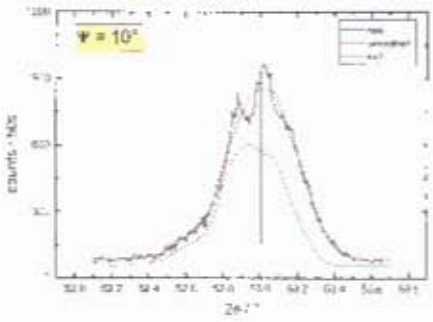

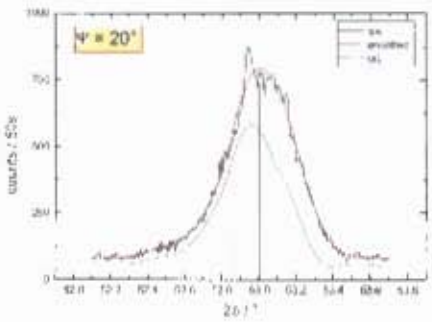

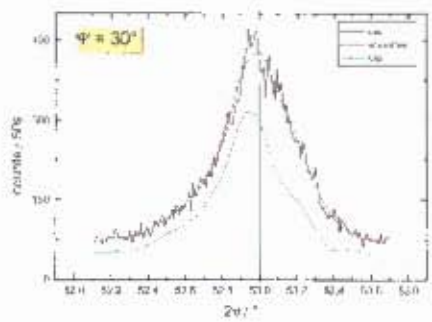

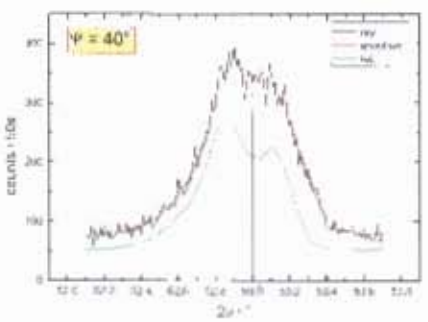

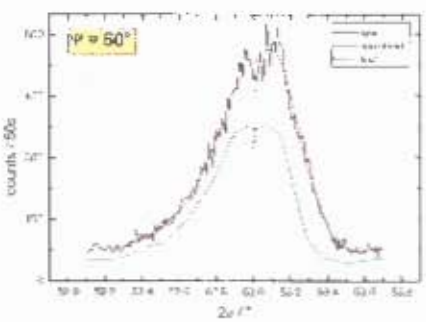

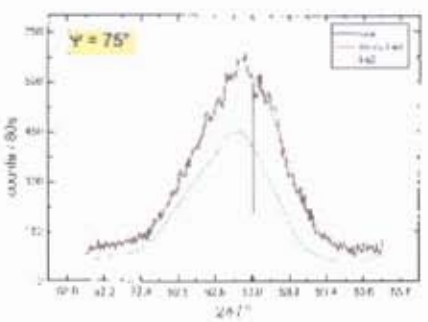

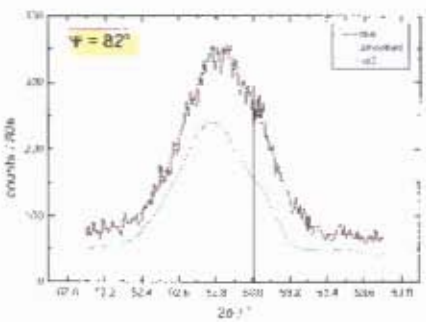

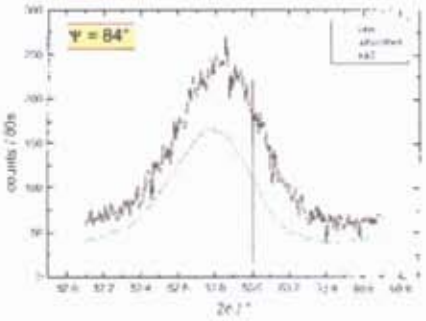

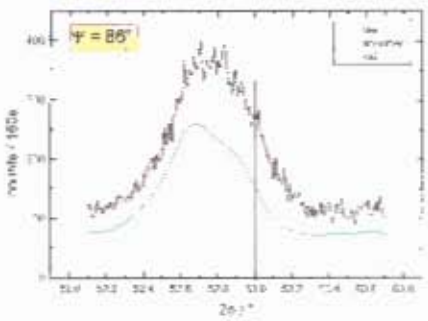

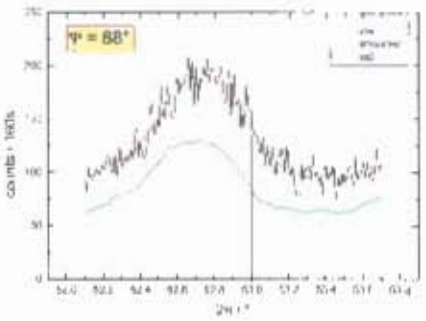

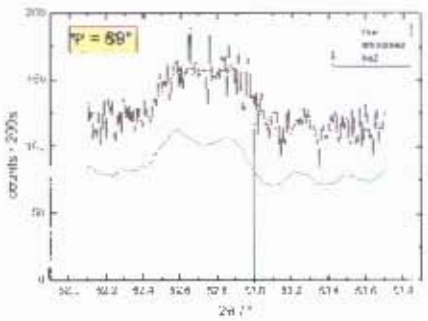

213 PEAKS (UNIMPLANTED)

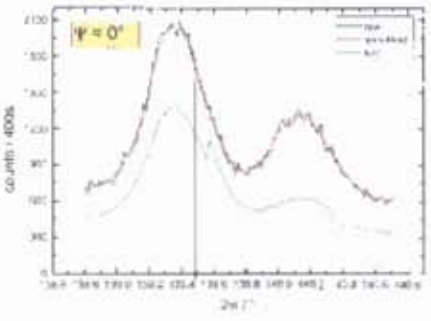

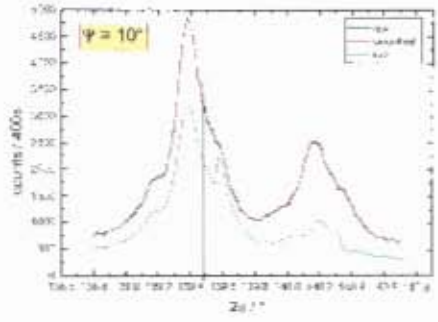

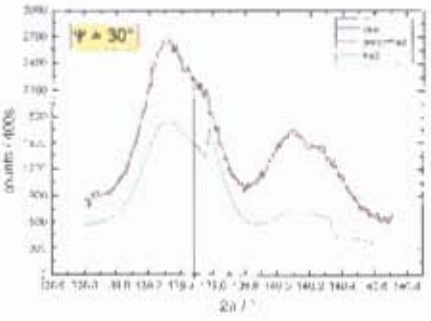

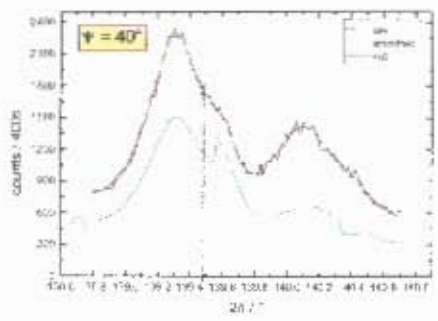

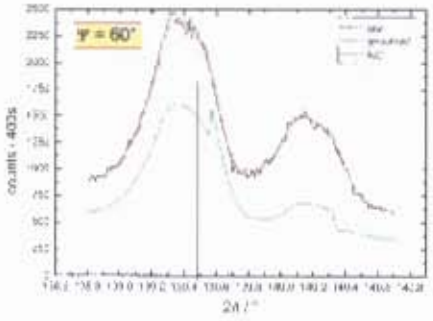
Ψ = 60°
counts
2θ / °

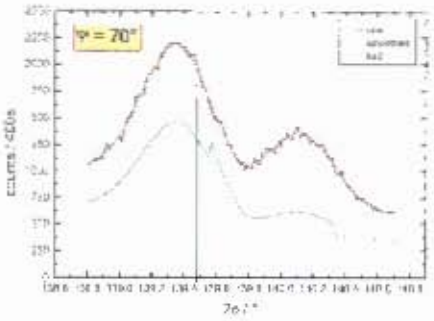
Ψ = 70°
counts
2θ / °

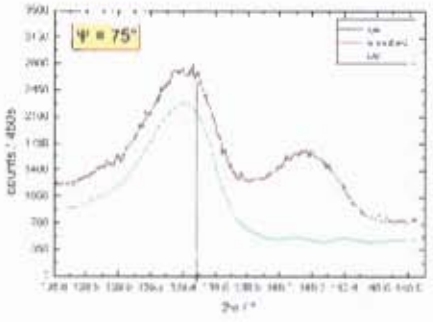
Ψ = 75°
counts
2θ / °

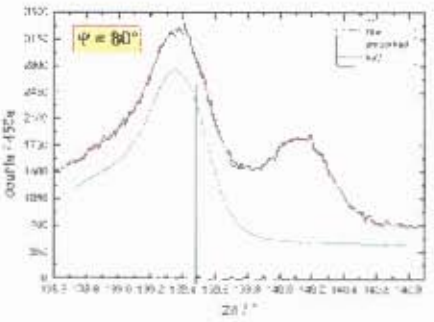
Ψ = 80°
counts
2θ / °

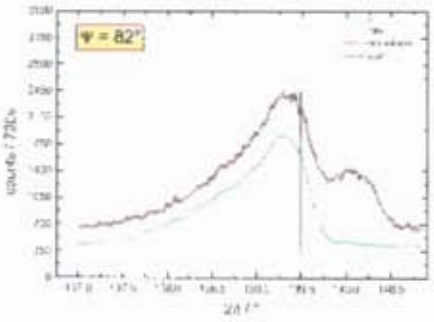
Ψ = 82°
counts
2θ / °

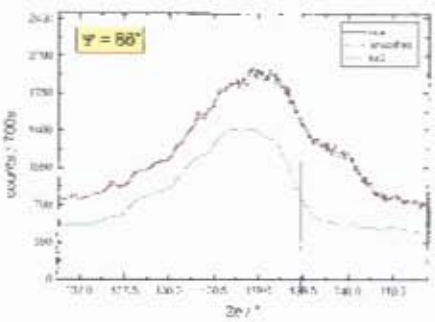
Ψ = 86°
counts
2θ / °

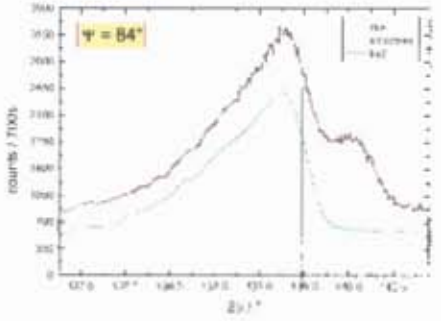

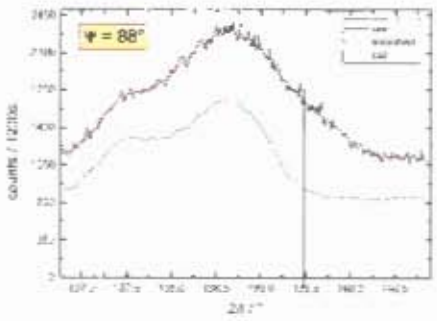

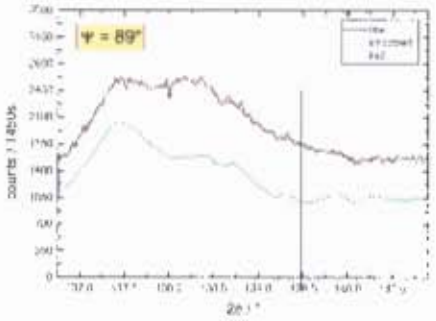

101 PEAKS (DOSE: 5 X 10^{16}Kr/cm^2)

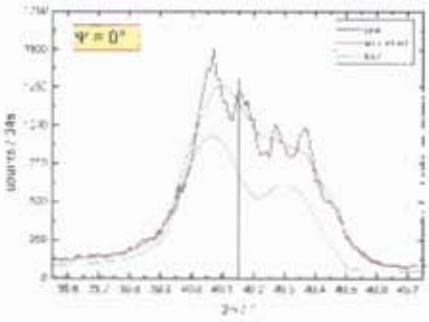

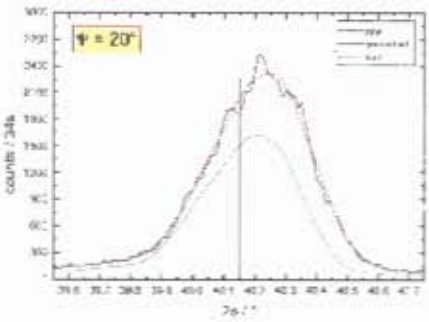

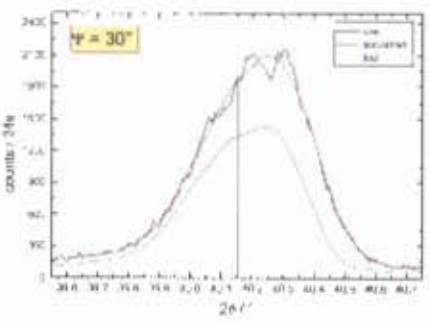

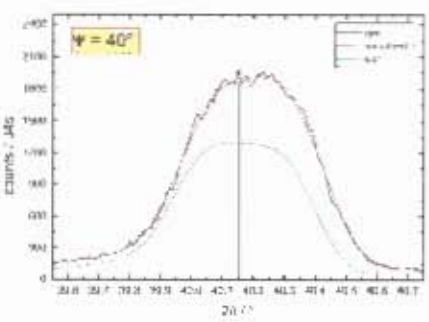

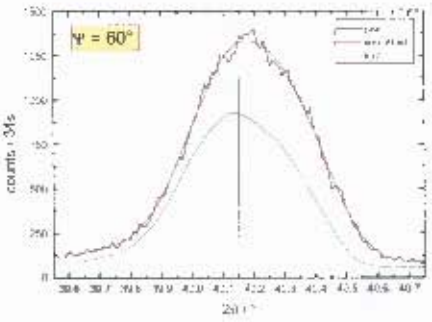
Ψ = 60°
counts / 34s
2θ / °

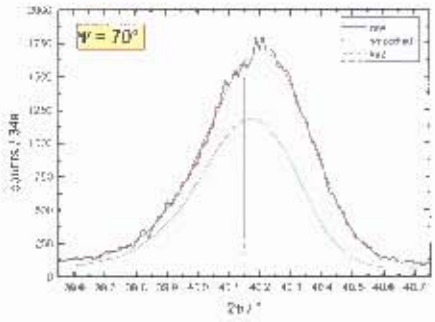
Ψ = 70°
counts / 34s
2θ / °

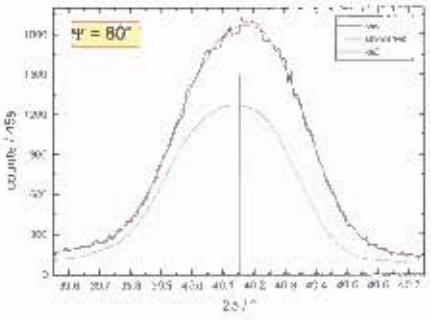
Ψ = 80°
counts / 45s
2θ / °

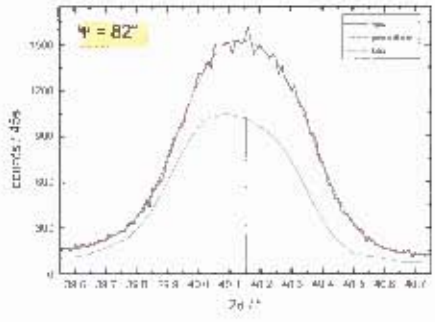
Ψ = 82°
counts / 45s
2θ / °

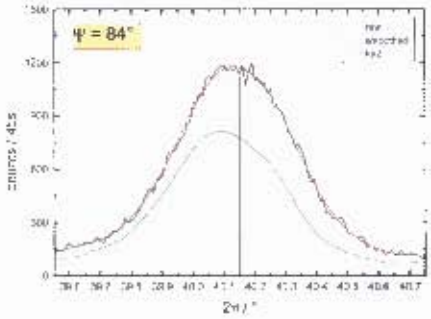
Ψ = 84°
counts / 45s
2θ / °

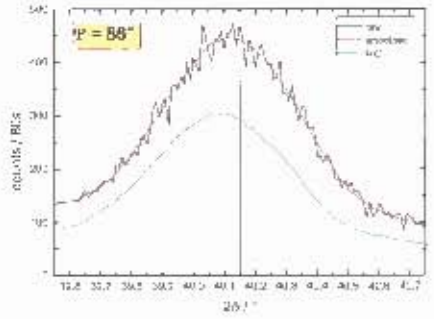
Ψ = 86°
counts / 45s
2θ / °

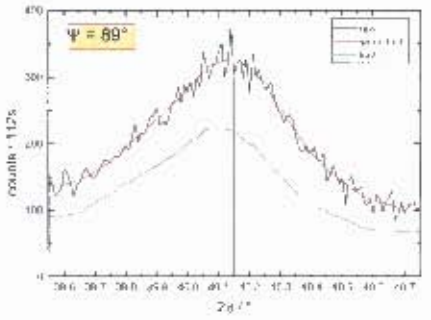
Ψ = 89°
counts / 112s
2θ / °

103 PEAKS (DOSE: 5 X 10^{16}Kr/cm^2)

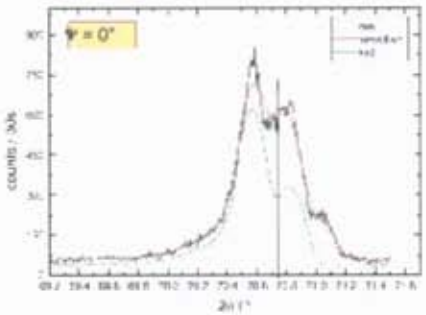

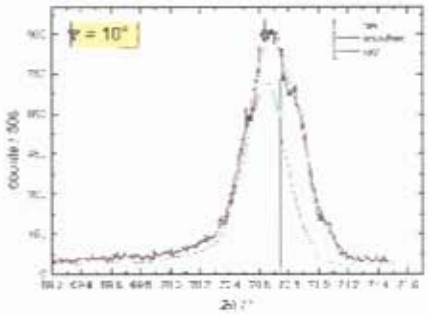

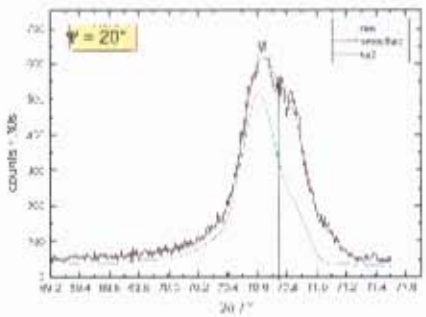

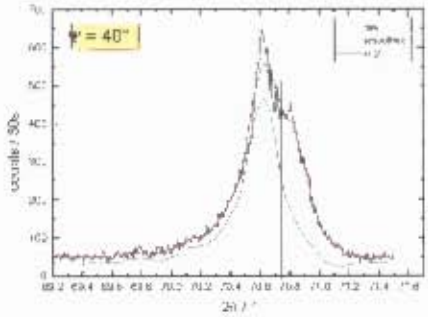

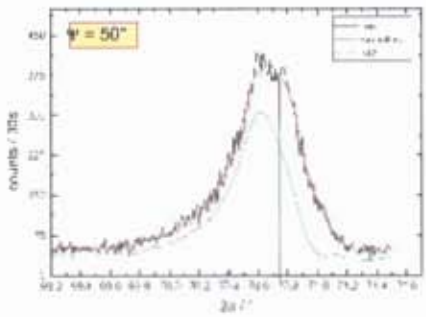

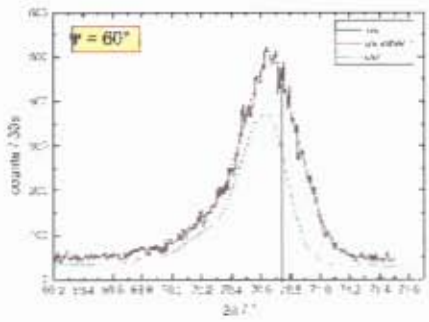

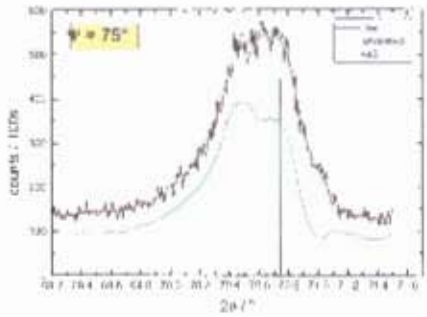

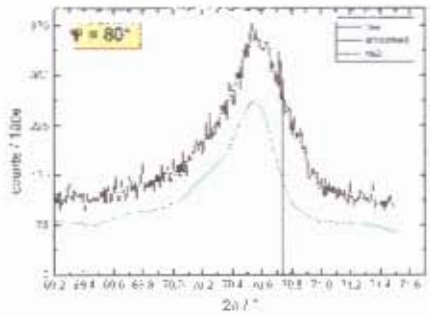

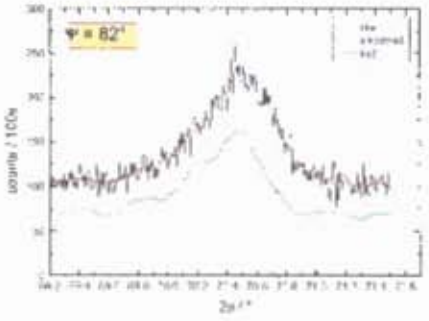
Ψ = 82°
2θ / °

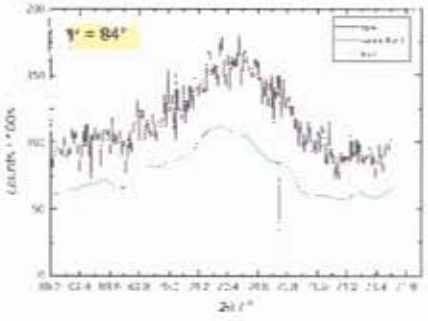
Ψ = 84°
2θ / °

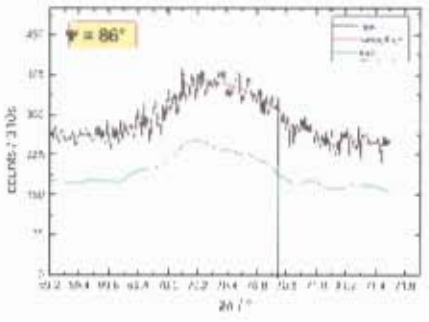
Ψ = 86°
2θ / °

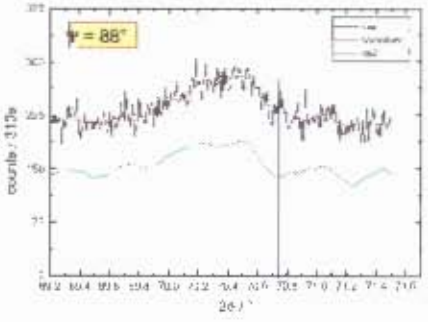
Ψ = 88°
2θ / °

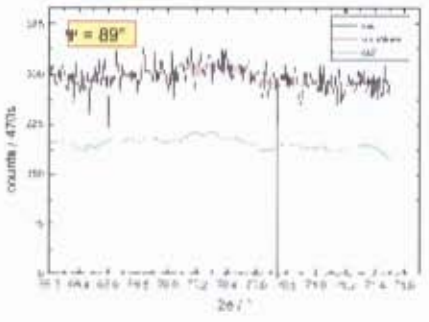
Ψ = 89°
2θ / °

213 PEAKS (DOSE: 5 X 10^{16}Kr/cm^2)

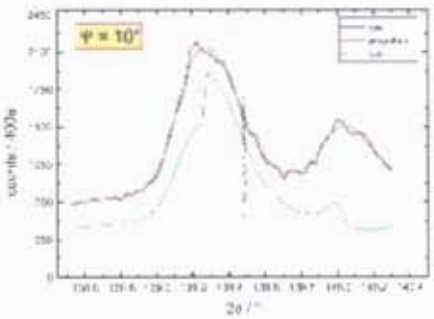

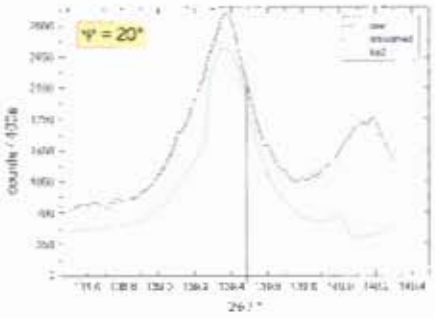

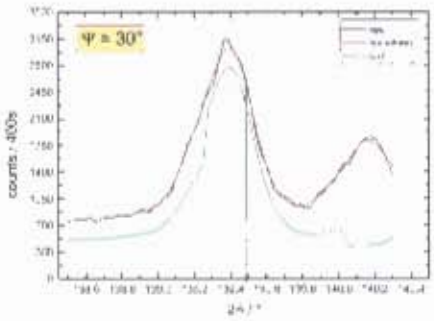

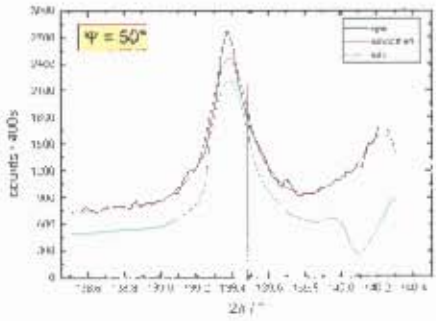

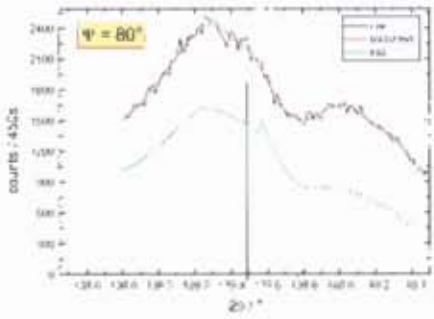

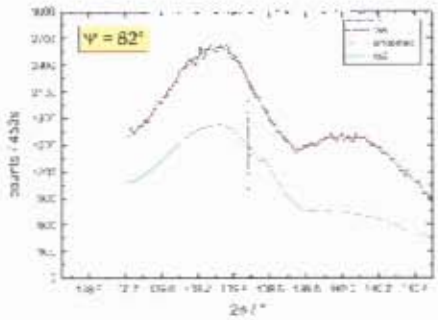

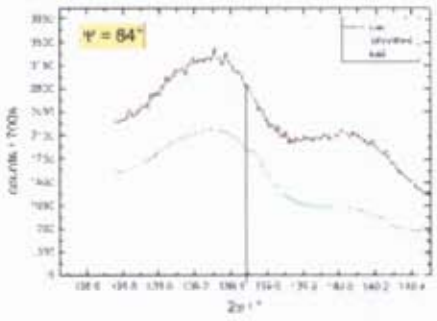
Ψ = 84°
counts / 700s
2θ / °

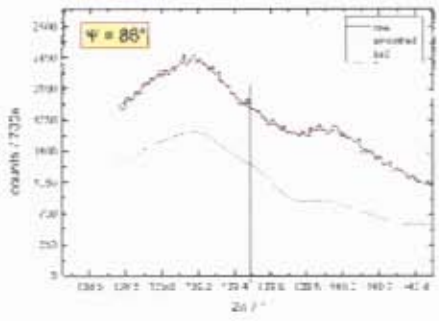
Ψ = 86°
counts / 735s
2θ / °

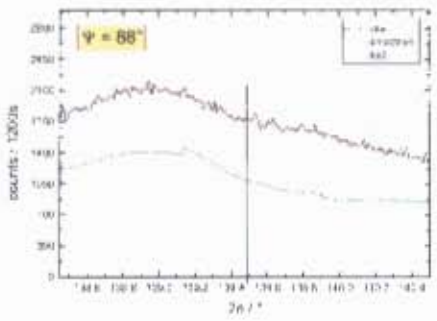
Ψ = 88°
counts / 1200s
2θ / °

APPENDIX B

SIN$^2\Psi$ CURVES FOR IMPLANTED AND UNIMPLANTED TITANIUM SAMPLES. Ti4 IS THE SAMPLE IMPLANTED WITH 1 X $10^{15}Kr^+/cm^2$ AND Ti4 IS THE SAMPLE IMPLANTED WITH 5 X $10^{15}Kr^+/cm^2$.

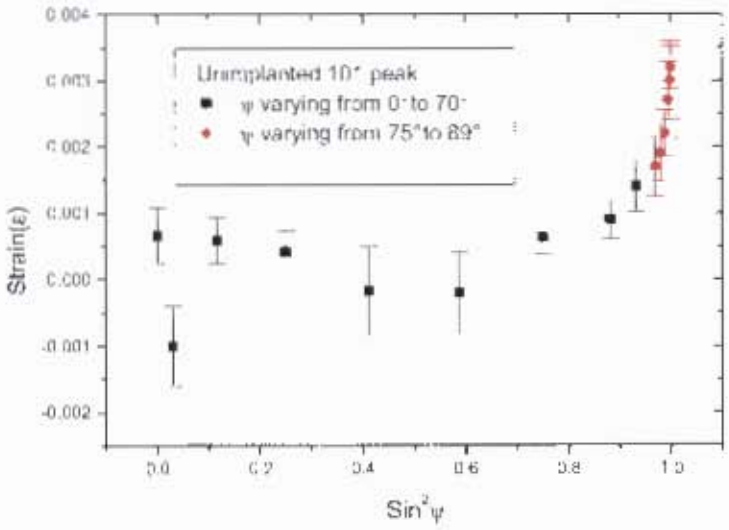

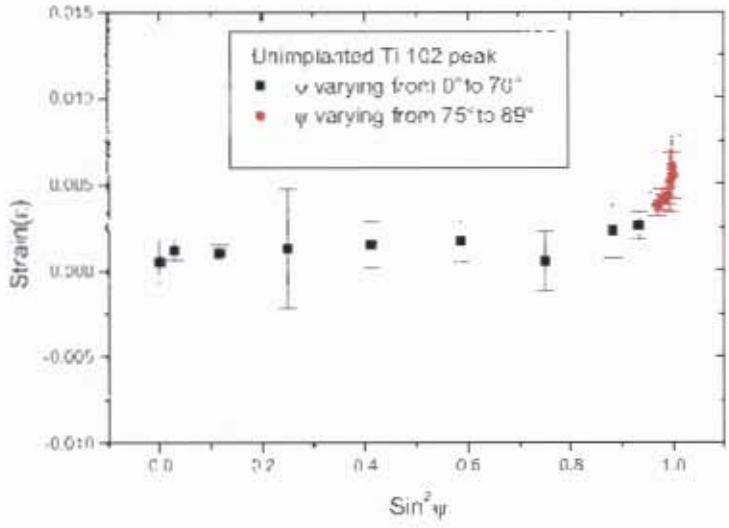

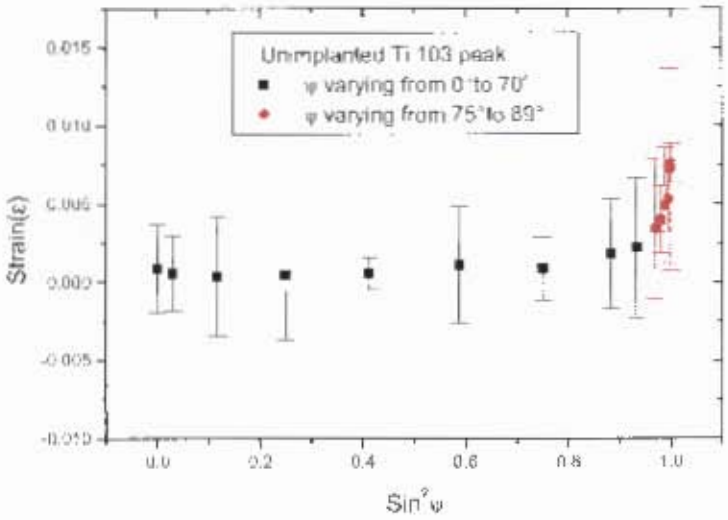
Unimplanted Ti 103 peak
ψ varying from 0° to 70°
ψ varying from 75° to 89°
Strain(ε)
0.015
0.010
0.005
0.000
-0.005
-0.010
0.0
0.2
0.4
0.6
0.8
1.0
Sin²ψ

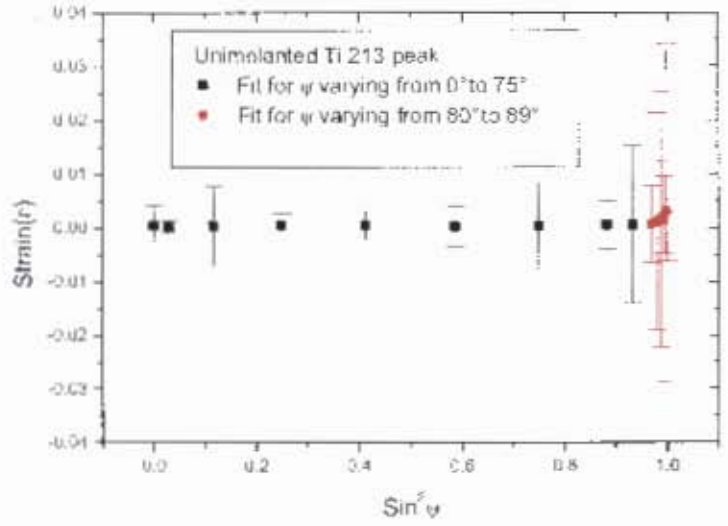
Unimplanted Ti 213 peak
Fit for ψ varying from 0° to 75°
Fit for ψ varying from 80° to 89°
Strain(ε)
0.04
0.03
0.02
0.01
0.00
-0.01
-0.02
-0.03
-0.04
0.0
0.2
0.4
0.6
0.8
1.0
Sin²ψ

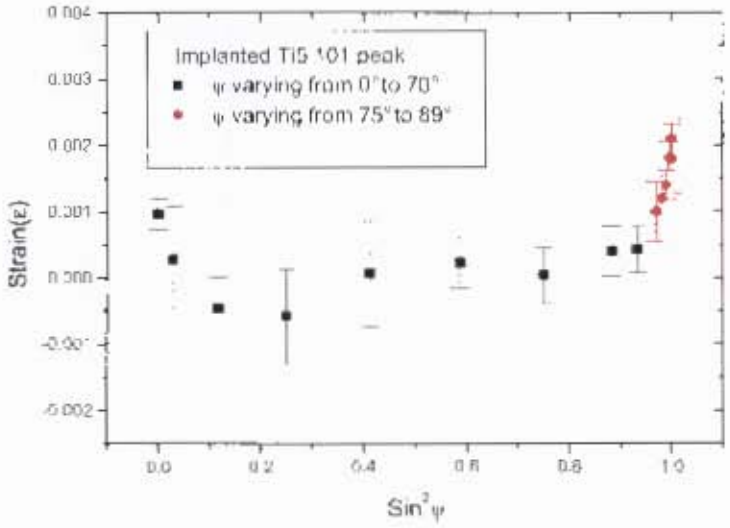
Implanted Ti5 101 peak
ψ varying from 0° to 70°
ψ varying from 75° to 89°
Strain(ε)
Sin²ψ

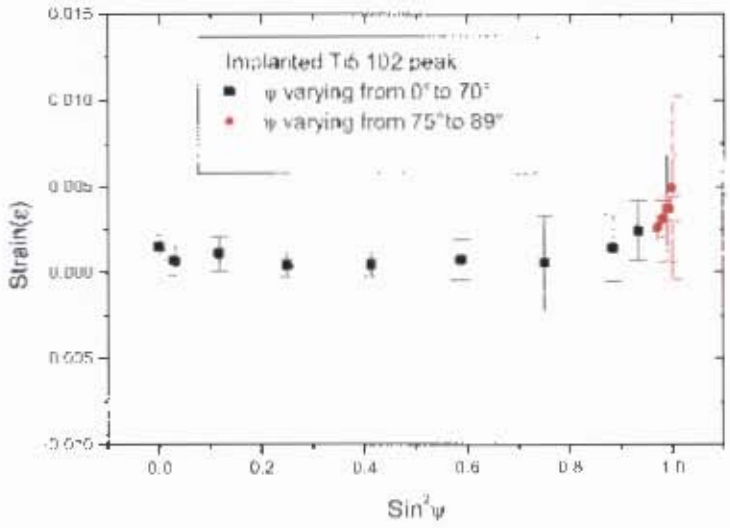
Implanted Ti5 102 peak
ψ varying from 0° to 70°
ψ varying from 75° to 89°
Strain(ε)
Sin²ψ

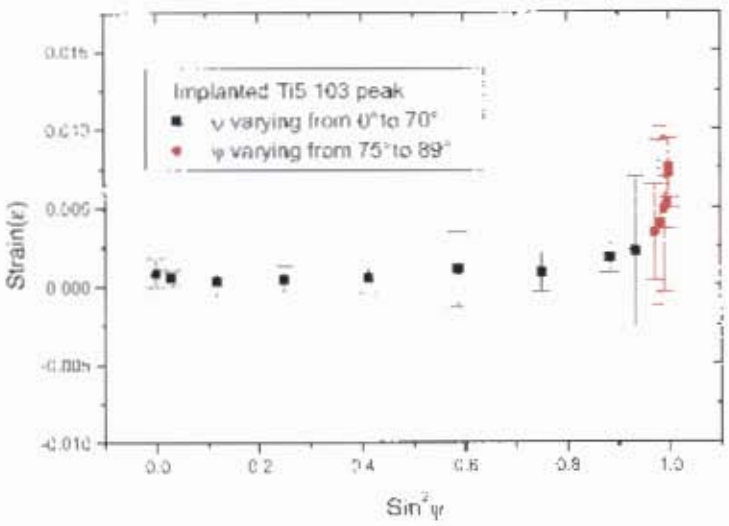
Implanted Ti5 103 peak
ν varying from 0°to 70°
ψ varying from 75°to 89°
Strain(ε)
Sin²ψ

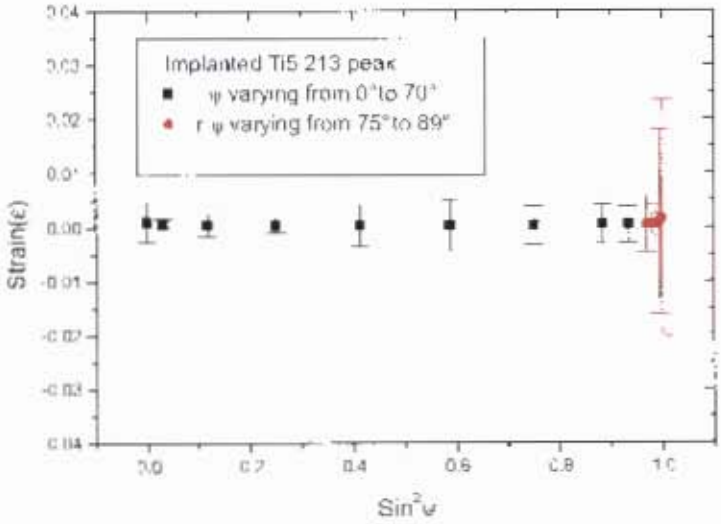
Implanted Ti5 213 peak
ψ varying from 0°to 70°
ψ varying from 75°to 89°
Strain(ε)
Sin²ψ

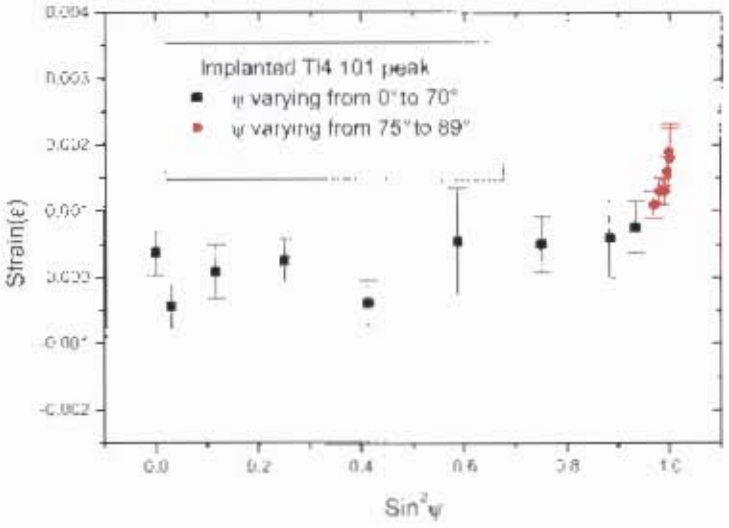
Implanted Ti4 101 peak
ψ varying from 0° to 70°
ψ varying from 75° to 89°
Strain(ε)
Sin²ψ

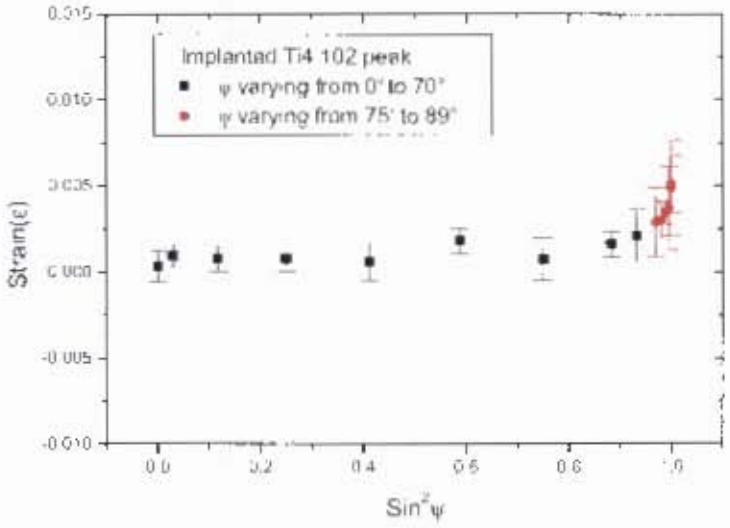
Implanted Ti4 102 peak
ψ varying from 0° to 70°
ψ varying from 75° to 89°
Strain(ε)
Sin²ψ

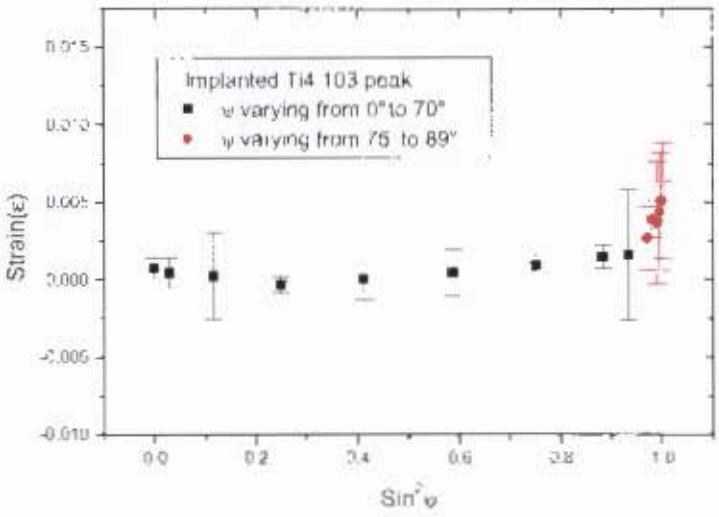
Implanted Ti4 103 peak
ψ varying from 0°to 70°
ψ varying from 75 to 89°
Strain(ε)
Sin²ψ

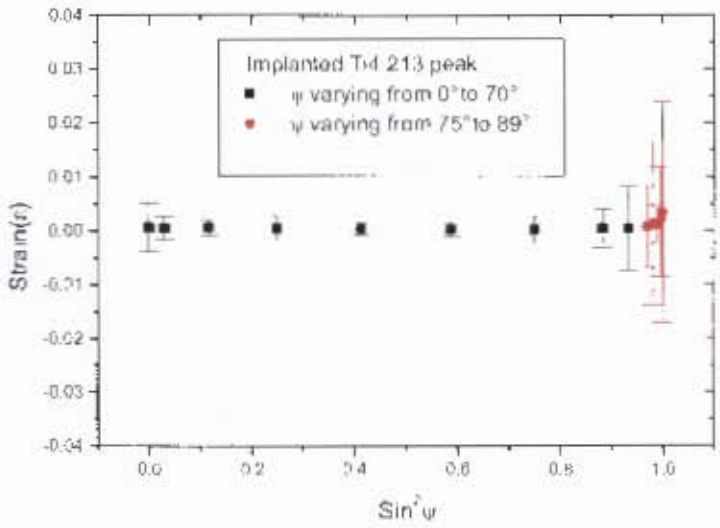
Implanted Ti4 213 peak
ψ varying from 0°to 70°
ψ varying from 75°to 89°
Strain(ε)
Sin²ψ

LIST OF REFERENCES

1. W.Ramsay, M.W Travers: *Proc. Royal. Soc*, Vol. 61, 1987, pp. 267
2. Hg. Matzke: *Fundamentals aspects of inert gases in solids*, S.E Donnelly and J.H Evans (Eds), Plenum press, New York, 401, 1991
3. L. Babsail, N.Hamelin, P.D Townsend: *Nuclear Instrum. Methods B*, 59/60, 1219, 1991
4. D.J Chandler, L. Zhang, P.D Townsend: *Nuclear Instrum .Methods* B, 59/60, 1223, 1991
5. F. Paszti: *Fundamentals aspects of inert gases in solids,* S.E Donnelly and J.H Evans (Eds), Plenum press, New York, 185, 1991

6 G. Hishmen, L. Cartz, F.G Karioris, C. Templier, J. Chaument, C. Clerc. *J. Am. Ceramic. Soc*, Vol. 76, 343, 1993

7. E.L Fleischer, M.G Norton, M.A. Zaleski, W. Hertl, C.B Carter and J.W Mayer: *J. Mater. Res*, Vol. 6, Number 9, 1905, 1991
8. D. Rafaja, Vaclav Valwda, Anthony J. Perry, James R. Treglio: Depth profile of residual stress in metal-ion implanted TIN coatings, *Surface and Coatings Technology,* Vol. 92, 135, 1987
9. D.T. Britton, F.P. Nemalili, and M. Härting: Electrical Resistivity of Copper containing Solid Krypton Precipitates, *Physica Status Solidi*, Vol.198, 238, 2003
10. A.J Perry, B.D. Sartwell, V. Valvoda, D. Rafaja, D.L Williamson and A.J Nelson: *Vac. Science Tech A*, Vol. 10, Number 4, 1446, 1992
11. L.J Liu, D.K Sood, R.R Manory, W. Zhou: *Surface Coating Technology*, Vol. 71, 159, 1995
12. D.E Rimmer and A.H Cottrell, *Phil Mag. 2*, B45, 1957
13. R.Blackburn: *Metall. Reviews*, Vol.11, 159, 1906
14. S.T Picraux: Ion-Implantation in metals. *Ann. Rev. Mater-Science*, Vol.14, 335-372, 1984
15. P.D Townsend, J.C Kelly, N.E.W Hartley: Ion implantation, sputtering and their application. Academic press, New York, 1976.

16. A. J. Perry, D.E Gast: *Vacuum*, Vol.48, Number 10, 833, 1997.

17. C. McHargue: *Int. Met Rev*, 1986, Vol.31, 49, 1986

18. Sharkeev, Yu, P. Didenko, A.N, Kozlov, E. V: High dislocation density structures and hardening produced by high fluency pulsed-ion-beam Implantation, *Surface coating Technology*, 65,112, 1994

19. R.C. Birtcher, W. Jager: Precipitation of implanted krypton in Aluminium. *Journal of nuclear materials*, Vol. 135, 274, 1985.

20. Härting, M, Yaman, R. Bucher, and D.T. Britton: Residual stress in copper containing a high concentration of krypton precipitates, *Advanced Engineering Materials* **4**, 592, 2002

21. D.L. Smith, P.C. Rice-Evans and D.T Britton. Evidence for deep lattice damage in krypton-implanted titanium, revealed by positrons. *Philosophical magazine* A, Vol.61, No.6, 839, 1990.

22. F. Halitim, N. Ikhlef, L. Boudoukha, G. Fantozzi. The effect of copper implantation on the mechanical, structural properties and residual stress of polycrystalline alumina. *Thin solid films*, Vol.300, 197, 1997.

23. M.K. Kloska and O. Meyer. Lattice site occupation of oversized impurity atoms in aluminium single crystals. *Nuclear Instruments and Methods in Physics Research B*, Vol.19/20, 140, 1986

24. J.D Kamminga, Th.H de Keijser, E.J. Mittemeijer, R. Delhez: New methods for diffraction stress measurements: a critical evaluation of new and existing Methods. *J. Applied Crystallography*, 1059, 2000

25. M. Van Leeuwen, J.D Kamminga, E.J Mittemeijer: Diffraction stress analysis of thin films, modelling and epitaxial evaluation of elastic constants and grain interaction. *J. Applied Physics*, Vol. 86, No. 4, 1999

26. www.srim.org/SRIM/SRIMLEGL.htm

27. R Allnat and A.B Lidiard: Atomic *transport in solids*. Cambridge University Press, 55, 1993

28. R. Bullough and M. H. Wood: *Theory of Microstructural Evolution, in Physics of Radiation Effects in Crystals*. R.A Johnson and A.N. Orlov (Eds), North Holland, Amsterdam, 189.

29. A.Guiner, R. Jullien: *The solid state. From superconductors to superalloys*.

Oxford science publication, 200, 1989

30. C. Kittel: *Introduction to Solid State Physics*. John Wiley press, 2005
31. C.A.Wert, R.M Thomson: *Physics of solids*. McGraw-Hill Book Company, 95, 1964
32. P.J Withers and H.K.D.H. Badeshia: Residual Stress Part1-Measurements Techniques. *Materials Science and Technology*, Vol. 17, 355, 2001
33. P.J Withers and H.K.D.H. Badeshia, Residual Stress Part 2- Nature and origins. *Materials Science and Technology*. Vol. 17, 366, 2001
34. X. Liu, P.K. Chu, C. Ding: Surface modification of Titanium, Titanium alloys and related materials for biomedical applications. *Material science and Engineering*, Vol.47, Issues 3-4, 2004.
35. J.A Borders. Metastable phases in metals produced by ion implantation. *Annual rev. Mater. Sci.* Vol.9, 313, 1979
36. D.G Freeman, J.H Nelson, R.S Stephan. Ion Implantation. Amsterdam, North Holland, 802, 1973
37. F.H Eisen, L.T Chadderton (Eds). Ion Implantation. London: Gordon and Breach
38. I. Ruge, J. Graul. Ion implantation in semiconductors. Berlin Springer,
39. B. L Crowder(Ed). Ion implantation in semiconductors and other materials. New York: Plenum press
40. S. Namba (Ed).Ion implantation in semiconductors: Science and Technology. New York: Plenum press
41. F.Chernow, J.A. Borders, D.K. Brice. Ion implantation in semiconductors. New York: Plenum
42. D. Rafaja, V. Valwda, A. J. Perry, J. R. Treglio. Depth profile of residual stress in metal-Ion Implanted TIN coatings, *Surface and Coatings Technology*. Vol.92, 135, 1987
43. J.S Williams: Materials modification with Ion beams, Rep. Prog. Physics Vol.49, 491, 1986
44. D.R. Clarke, S. Suresh I.M Ward: Ion-Solid interactions process: Fundamentals and applications: Cambridge University Press, 1996
45. J. Peltola: Stopping power for Ions and Clusters in crystalline solids, PhD

Thesis, University of Helsinki, Helsinki, Finland, 2003

46. D.R Clarke, S Suresh, I.M Ward (Eds): Ion-solid interactions: Fundamentals and Applications, Cambridge University Press, 1986

47. J.O Stigler and L. K. Mansur: Radiation effects in structural materials. Ann. Rev. Mater. Sci, 405, 1979

48. D.T Britton and M. Härting: The influence of strain on point defect dynamics. *Advanced Engineering Materials*. Vol. 4, No. 8, 2002

49. J.D Eshelby: *Phil.Trans.Roy.Soc.Lond.* Vol.244, 87, 1952

50. F. Mott, F.R.N. Nabarro: *Proc. Phys. Soc.* Vol. 52, 86, 1940

51. W. G. Malmqvist: Accelerator based Ion beam analysis and future prospects. *Radiation Physics and Chemistry*, Vol. 71, 817, 2004

52. W.K Chu, J. W. Mayer, M-A. Nicolet : Backscattering Spectrometry. Academic Press Inc.

53. W.K Chu, J. W. Mayer, M-A. Nicolet, T.M Buck, G. Amsel, F. Eisen: Principles and application of ion beam techniques for the analysis of solids and thin films. *Thin Solid Films*, Vol. 17, 1, 1973

54. L. R. Doolittle: Algorithm for the rapid simulation of Backscattering Spectra, *Analy. Nucl. Inst. Meth* B9, 334, 1985

55. L. R. Doolittle: A semiautomatic algorithm for the Rutherford Backscattering *Analy. Nucl. Inst. Meth*.B15, 227, 1986

56. http://www.cea.com/cai/rbsinst/cairinst.htm

57. S.A Martinez, S. Salhish, M. P. Blodgett and M.J Shepard: Residual stress distribution on surface-treated Ti-6al-4V by X-ray Diffraction, *Society of Experimental Mechanics*, 141-147, 2003

58. S.K Prevey: X-ray Diffraction Residual stress techniques, Metals Handbook.9th Edition, Vol. 10,American Society of Metals, Metals park OH, pp.380-392, 1986

59. I.C .Noyan, and Cohen, J.B: Residual stress measurement by Diffraction and Interpretation, Springer-Verleg, New York, 1987

60. Victor M.Hauk and E.Eckard Macherauch: A useful guide for X-ray stress Evaluation (XSE).*Advances in X-ray analysis*, Vol. 27, 1983

61. H. P. Klug and L.E. Alexander, X-Ray Diffraction Procedures, 2nd

Edition, Wiley, New York, 1979.

62. M. van Leeuwen, J.D Kamminga, J.Mittemeijer, Diffraction stress analysis of thin films: Modelling and experimental evaluation of elastic constants and grain interaction. *Journal of Applied Physics*, Vol.86, Number 4, 1999
63. H. Möller and G.martin: *Mitt.K-Wilh.-Inst.Einsenforschg*, Vol.21, 261,1939
64. W.Voigt: Lehrbuch der Kristallphysik, Teubner, Leipzig, Berlin, 1910
65. H. Neerfeld: Mitt.K-*Wilh.-Inst.Einsenforschg*,Vol.24, Number 61,1967
66. R. Hill: *Proc. Phys. Soc.* London Vol.65, 349, 1952
67. L.R. Doolittle: RUMP-RBS analysis and simulation package, *Nucl. Instr. And Methods*. B9, 5008, 1985
68. T.P Ntsoane: Private Communication
69. D8 Advance/D8 Discover X-ray Diffractometer user's manual. Issue 2-12, 1999, Bruker analytical X-ray systems, 1999(2)
70. CAS. 7440-32-6. Natl. Bur. Stand. (U.S), Circ.538, Vol.0, (1954) primary reference: Swanson, Fuyat
71. C.Templer, H. Garem, J.P.Riviere and J.Delafond: Solid and fluid xenon in Xe implanted aluminium. . *Nuclear Instruments and Methods in Physics Research*, B18, 24, 1986
72. M. Härting, S.Woodford, D.Knoesen, R.Bucher and D.T Britton: Stress in hydrogenated amorphous silicon determined by X-ray reflection. Thin Solid Films Vol.430, 153, 2003
73. M. Härting, S.Nsengiyumva, A.T. Raji, G. Dollinger, P.Sperr, S.R. Naidoo, T.E. Derry, C.M. Comrie, and D.T. Britton. 14th International conference on surface modification of materials by ion beams, September, 2005, Kudaisi Turkey.
74. J.D Eshelby: The determination of the elastic field of an ellipsoidal inclusion, and related problems. *Phil.Trans.Roy.Soc.Lond*, Vol.197, 396, 1954
75. M. H Härting: Privatc discussion
76. K.F.Badawi, Ph.Goudeau, J. Pacaud, C. Jaouen, J. Delafond, A. Naudon and G.Gladyszewski: X-ray diffraction study of residual stress modification in Cu/W superlattices irradiated by light and heavy ions. *Nuclear Instruments and Methods in Physics Research*, B80/81, 404, 1993